

AD-A020 713

PASSIVE NOSETIP TECHNOLOGY (PANT) PROGRAM.  
VOLUME XV. ROUGHNESS INDUCED TRANSITION ON  
BLUNT AXISYMMETRIC BODIES - DATA REPORT

M. D. Jackson

Acurex Corporation

Prepared for:

Space and Missile Systems Organization

April 1974

DISTRIBUTED BY:

**NTIS**

National Technical Information Service  
U. S. DEPARTMENT OF COMMERCE

055045

SAMSO-TR-74-86  
Volume XV

ADA020713

INTERIM REPORT  
PASSIVE NOSETIP TECHNOLOGY  
(PANT) PROGRAM

Volume XV. Roughness Induced Transition on Blunt  
Axisymmetric Bodies - Data Report

M. D. Jackson

Aerotherm Division/Acurex Corporation

SAMSO-TR-74-86

April 1974

AEROTHERM REPORT 74-100

DDC  
EXPERIMENTAL  
1976  
FILED

~~This document may be distributed further by any holder  
only with specific prior approval of Space and Missile  
Systems Organization (SAMSO), Los Angeles, California.~~

Air Force Space and Missile  
Systems Organization  
Los Angeles, California

**DISTRIBUTION STATEMENT A**

Approved for public release  
Distribution Unlimited

Contract F04701-71-C-0027

Reproduced by  
NATIONAL TECHNICAL  
INFORMATION SERVICE  
U.S. Department of Commerce  
Springfield VA 22151

VOL 14  
R 930 713

DISTRICT OF COLUMBIA  
 DEPARTMENT OF THE DISTRICT ATTORNEY  
 OFFICE OF THE DISTRICT ATTORNEY  
 1000 PENNSYLVANIA AVENUE, N.W.  
 WASHINGTON, D.C. 20004

## FOREWORD

This document is Volume XV of the Interim Report series for the Passive Nosetip Technology (PANT) program. A summary of the documents in this series prepared to date is as follows:

- Volume I - Program Overview (U)
- Volume II - Environment and Material Response Procedures for Nosetip Design (U)
- Volume III - Surface Roughness Data
  - Part I - Experimental Data
  - Part II - Roughness Augmented Heating Data Correlation and Analysis (U)
  - Part III - Boundary Layer Transition Data Correlation and Analysis (U)
- Volume IV - Heat Transfer and Pressure Distributions on Ablated Shapes
  - Part I - Experimental Data
  - Part II - Data Correlation
- Volume V - Definition of Shape Change Phenomenology from Low Temperature Ablator Experiments
  - Part I - Experimental Data, Series C (Preliminary Test Series)
  - Part II - Experimental Data, Series D (Final Test Series)
  - Part III - Shape Change Data Correlation and Analysis
- Volume VI - Graphite Ablation Data Correlation and Analysis (U)
- Volume VII - Computer User's Manual, Steady-State Analysis of Ablating Nosetips (SAANT) Program
- Volume VIII - Computer User's Manual, Passive Graphite Ablating Nosetip (PAGAN) Program
- Volume IX - Unsteady Flow on Ablated Nosetip Shapes - PANT Series G Test and Analysis Report

- Volume X - Summary of Experimental and Analytical Results
- Volume XI - Analysis and Review of the ABRES Combustion Test Facility for High Pressure Hypothermal Reentry Nosetip Systems Tests
- Volume XII - Nosetip Transition and Shape Change Tests in the AFFDL 50 MW RENT Arc - Data Report
- Volume XIII - An Experimental Study to Evaluate Heat Transfer Rates to Scalloped Surfaces - Data Report
- Volume XIV - An Experimental Study to Evaluate the Irregular Nosetip Shape Regime - Data Report
- Volume XV - Roughness Induced Transition Experiments - Data Report

This report was prepared by Aerotherm Division/Acurex Corporation under Contract F04701-71-C-0027. Volumes I through IX covered PANT activities from April 1971 through April 1973. Volumes X through XV represent contract efforts from May 1973 to December 1974. Volume X summarizes the respective test programs and describes improvements in nosetip analysis capabilities. Volume XI presents an evaluation of the ABRES test facility in terms of performing thermostructural and reentry flight simulation testing. Volumes XII through XV are data reports which summarize the experiments performed for the purpose of defining the irregular flight regime. The analysis of these data are presented in Volume X.

This work was administered under the direction of the Space and Missile Systems Organization with Lieutenant A. T. Hopkins and Lieutenant E. G. Taylor as Project Officers with Mr. W. Portenier and Dr. R. L. Baker of the Aerospace Corporation serving as principal technical monitors. Mr. M. D. Jackson was test engineer and principal Aerotherm investigator for the work described in this volume.

This technical report has been reviewed and is approved

*E. G. Taylor*

E. G. Taylor, Lt. USAF  
Project Officer  
Aero and Materials Division  
Directorate of Systems Engineering  
Deputy for Reentry Systems

# ABSTRACT

Laminar, transitional and turbulent heat-transfer coefficients measured on six roughened calorimeter models are presented. Four of the models were sphere cones with nose radii of .75, 1.5, 2.5 and 3.5 inches and with an eight degree cone half angle. One 60 degree forecone biconic with an eight degree cone half angle, and one laminar ablated shape calorimeter were also tested. The nominal roughness height on these models was 3.5 mils. The tests were conducted at  $M_\infty = 5$  and at sonic point unit Reynolds numbers from  $.42 \times 10^6/\text{ft}$  to  $7.4 \times 10^6/\text{ft}$ . Larger Reynolds numbers were required in order to promote rough wall boundary layer transition on the smaller nose radius models.

## TABLE OF CONTENTS

<u>Section</u>		<u>Page</u>
1	INTRODUCTION	1-1
2	EXPERIMENTAL OBJECTIVES AND APPROACH	2-1
3	DESCRIPTION OF CALORIMETER MODELS	3-1
	3.1 Model Fabrication	3-1
	3.2 Definition of Surface Roughness	3-12
4	TEST CONDITIONS	4-1
5	DESCRIPTION OF RECORDED DATA	5-1
6	TEST RESULTS	6-1
	6.1 Data Reduction Technique	6-1
	6.2 Test Data	6-3
7	SUMMARY OF RESULTS AND CONCLUSIONS	7-1
	REFERENCES	R-1

## LIST OF FIGURES

<u>Figure</u>		<u>Page</u>
1	Configuration for .75 Inch Sphere-Cone Calorimeter and Adapter	3-3
2	Configuration for 1.5 Inch Sphere-Cone Calorimeter and Adapter	3-4
3	Configuration for 2.5 Inch Sphere-Cone Calorimeter and Mounting Ring	3-5
4	Configuration for 3.5 Inch Sphere-Cone Calorimeter and Mounting Ring	3-6
5	Configuration for 3.5 Inch Laminar-Blunt Calorimeter and Mounting Ring	3-7
6	Configuration for 1.5 Inch Shoulder Radius/60°/8° Biconic Calorimeter and Adapter	3-8
7	Pretest Photographs of .75, 1.5 Sphere-Cone Models and Biconic Model	3-9
8	Assembly Configuration for 3.5 Inch Sphere-Cone Calorimeter (2.5 Inch Sphere-Cone and 3.5 Inch Laminar Ablated Shape Models also used Calorimeter Sting)	3-10
9	Assembly Configuration for 1.5 Inch Sphere-Cone Calorimeter (60° Biconic Calorimeter and .75 Inch Sphere-Cone also uses LTA Sting)	3-11
10	Definition of Thermocouple Locations for 2.5-Inch Sphere Cone Model	3-13
11	Definition of Thermocouple Locations for .75 Inch Sphere Cone Model	3-14
12	Definition of Thermocouple Locations for 1.5 Inch Sphere Cone Model	3-15
13	Definition of Thermocouple Locations for 3.5 Inch Sphere Cone Model	3-16
14	Definition of Thermocouple Locations for Laminar Ablated Shape Model	3-17
15	Definition of Thermocouple Locations for Biconic Model	3-18
16	Cross Section Photomicrographs of Rough Wall Calorimeter Surface Specimens	3-19



## LIST OF FIGURES

<u>Figure</u>		<u>Page</u>
1	Configuration for .75 Inch Sphere-Cone Calorimeter and Adapter	3-3
2	Configuration for 1.5 Inch Sphere-Cone Calorimeter and Adapter	3-4
3	Configuration for 2.5 Inch Sphere-Cone Calorimeter and Mounting Ring	3-5
4	Configuration for 3.5 Inch Sphere-Cone Calorimeter and Mounting Ring	3-6
5	Configuration for 3.5 Inch Laminar-Blunt Calorimeter and Mounting Ring	3-7
6	Configuration for 1.5 Inch Shoulder Radius/60°/8° Biconic Calorimeter and Adapter	3-8
7	Pretest Photographs of .75, 1.5 Sphere-Cone Models and Biconic Model	3-9
8	Assembly Configuration for 3.5 Inch Sphere-Cone Calorimeter (2.5 Inch Sphere-Cone and 3.5 Inch Laminar Ablated Shape Models also used Calorimeter Sting)	3-10
9	Assembly Configuration for 1.5 Inch Sphere-Cone Calorimeter (60° Biconic Calorimeter and .75 Inch Sphere-Cone also uses LTA Sting)	3-11
10	Definition of Thermocouple Locations for 2.5-Inch Sphere Cone Model	3-13
11	Definition of Thermocouple Locations for .75 Inch Sphere Cone Model	3-14
12	Definition of Thermocouple Locations for 1.5 Inch Sphere Cone Model	3-15
13	Definition of Thermocouple Locations for 3.5 Inch Sphere Cone Model	3-16
14	Definition of Thermocouple Locations for Laminar Ablated Shape Model	3-17
15	Definition of Thermocouple Locations for Biconic Model	3-18
16	Cross Section Photomicrographs of Rough Wall Calorimeter Surface Specimens	3-19

## TABLE OF CONTENTS

<u>Section</u>		<u>Page</u>
1	INTRODUCTION	1-1
2	EXPERIMENTAL OBJECTIVES AND APPROACH	2-1
3	DESCRIPTION OF CALORIMETER MODELS	3-1
	3.1 Model Fabrication	3-1
	3.2 Definition of Surface Roughness	3-12
4	TEST CONDITIONS	4-1
5	DESCRIPTION OF RECORDED DATA	5-1
6	TEST RESULTS	6-1
	6.1 Data Reduction Technique	6-1
	6.2 Test Data	6-3
7	SUMMARY OF RESULTS AND CONCLUSIONS	7-1
	REFERENCES	R-1

# LIST OF FIGURES (Concluded)

<u>Figure</u>		<u>Page</u>
17	Sketch Indicating Definition of Nominal Surface Roughness Height (Surface Traced from 3.5 Mil Grit Blasted Surface Photomicrograph, 50X)	3-21
18	Typical AFML Profilometer Measurement of Nickel 200 Calorimeter Surface Roughness	3-22
19	Summary of AFML Profilometer RMS Measurements	3-23
20	Nominal Test Points at $M_\infty = 5.0$ in NOL Hypersonic Wind Tunnel	4-2
21	Effect of Mass Addition on RMS Pressure Fluctuations in NOL Hypersonic Tunnel Mach 5 Nozzle	4-4
22	RMS Pressure Fluctuations in NOL Hypersonic Tunnel Mach 5 Nozzle	4-6
23	Sample of Measured Thermocouple Histories	5-2
24	Sample Shadowgraph Photographs	5-9
25	Specific Heat as a Function of Temperature for Electroformed Nickel and Nickel 200	6-4
26	Thermal Conductivity as a Function of Temperature for Electroformed Nickel and Nickel 200	6-5
27	Recovery Temperature Distribution	6-6
28	Convective Heat Transfer Coefficient Distribution, Model 4, Sphere Cone, $R_N = 2.5$ Inches	6-10
29	Convective Heat Transfer Coefficient Distribution, Model 18, Sphere Cone, $R_N = 3.5$ Inches	6-14
30	Convective Heat Transfer Coefficient Distribution, Model 16, Sphere Cone, $R_N = .75$ Inch	6-21
31	Convective Heat Transfer Coefficient Distribution, Model 17, Sphere Cone, $R_N = 1.5$ Inches	6-27
32	Convective Heat Transfer Coefficient Distribution, Model 20, Biconic, $R_g = 1.5$ Inches	6-37
33	Convective Heat Transfer Coefficient Distribution, Model 19, Laminar Shape, $R_g = 3.5$ Inches	6-43
34	Summary of Transition Data on Sphere Cone Models	7-3

# LIST OF SYMBOLS

$c$	specific heat
$h$	convective heat transfer coefficient
$h_{tc}$	convective heat transfer coefficient
$k$	roughness height
$K$	thermal conductivity
$\dot{m}$	mass flow rate
$M$	Mach Number
$\Delta P$	RMS pressure fluctuation
$\Delta P_f$	nozzle cooling pressure differential
$P$	pressure
$q$	convective heat flux
$q_\infty$	dynamic pressure
$r$	radial distance from model centerline
$R_f$	recovery factor
$R_n$	nose radius
$R_s$	shoulder radius
$Re$	Reynolds Number

# LIST OF SYMBOLS (Concluded)

s streamwise distance

t wall thickness

T temperature

## Subscripts

C cooling

e boundary layer edge property

N nozzle

o model stagnation point property

r boundary layer recovery property

s supply condition

w property evaluated at wall conditions

$\infty$  free stream property

## Superscript

\* sonic point property

## SECTION 1

### INTRODUCTION

The overall objective of the PANT program (Contract F04701-71-C-0027) is to improve and validate the accuracy of existing nosetip design analysis computer codes. Task 4.2.5 of the PANT program has the objective of defining the environmental regimes which produce irregular nosetip shapes and updating nosetip design analysis codes. In order to satisfy this objective a series of wind tunnel and high pressure ablation tests was required. The tests were designed to obtain calorimeter and shape change data for geometries and environments of interest. The objectives of the four test series are given below.

50 MW Arc Heater Tests - Test ATJ-S graphite, Mod-III carbon/carbon, and reverse chevron carbon phenolic nosetip models in the 50 MW arc using a  $M_\infty = 3$  nozzle to assess the transition behavior and shape change response of "real" materials in a hyperthermal environment.

Series H Wind Tunnel Tests - Generate heat transfer data for a calorimeter replica of an LTA scallop roughened surface for comparison with inferred heat transfer data and predictions.

Series I Wind Tunnel Tests - Generate low temperature ablator (LTA) shape change data to determine the effect of relevant nosetip parameters on the formation and extent of irregular shapes.

Series J Wind Tunnel Tests - Generate heat transfer data which show the effect of surface roughness and model size on boundary layer transition and heating augmentation.

The 50 MW tests were conducted in the RENT leg of the 50 MW arc facility at the Air Force Materials Flight Dynamics Laboratory. Test series H and J were conducted in Tunnel No. 8 at the Naval Ordnance Laboratory (NOL) from February 21 to February 26, 1974. Test Series I was conducted at NOL from March 27 to April 4, 1974.

These test series compliment Series E and G which were directed at obtaining pressure data on nosetips of irregular shape. A brief description of these two test series is given below:

Series E (Task 4.2.3) - Generate high frequency pressure, acceleration, and shock shape stability data to establish the possibility of high frequency flow field pulsations on ablated nosetip shapes.

Series G (Task 4.2.7) - Generate high frequency pressure, acceleration, and shock shape stability data to determine the envelope of realistic nosetip shapes which induce high frequency flow field pulsations.

Test Series E and G were conducted in NOL Tunnel No. 8; Series E was conducted in October of 1972 and Series G was conducted from July 25 to August 1, 1973. The results of Series G are reported in Reference 1.

This data report presents the results of Test Series J. The test objectives are defined in Section 2, and the calorimeter models are described in Section 3. A description of the wind tunnel facility and test matrix is given in Section 4. A brief overview of the recorded data is presented in Section 5, and the reduced data, in terms of heat transfer coefficients, are presented in Section 6. Conclusions are given in Section 7.

## SECTION 2

### EXPERIMENTAL OBJECTIVES AND APPROACH

Prior to the PANT program, data were not available to accurately characterize the effects of material surface roughness on boundary layer transition forward of the sonic point on a reentry nosetip. The PANT Series A tests (Reference 2) generated a substantial data base from which to assess the importance of surface roughness on boundary layer transition. Subsequent correlation (Reference 3) of the Series A test data, however, indicated the need for additional transition data in order to define the effects of body shape and size on rough-wall boundary layer transition.

The basis of the Series B roughwall transition experiments was formulated in Reference 4. In this reference, pertinent transition data were compared to the correlations developed in Reference 3. Deficiencies in the data base were noted and an experimental test program was developed. As identified in Reference 4, the primary test objectives were

- To evaluate the effect of body size on transition onset and location
- To evaluate the effect of body shape on transition onset and location.

Secondary objectives were to obtain additional data on the effect of the wall cooling ratio,  $(T_w/T_e)$ , on rough wall boundary layer transition and to obtain additional data relative to rough wall heating augmentation.

The above objectives were accomplished by testing six calorimeter models in the NOL Tunnel number 8 at a free stream Mach number of 5 and over a sonic point unit Reynolds number ( $Re^*$ ) range from .42 to  $7.40 \times 10^6/\text{ft}$ . Four of the six models were sphere cones having nose radii of 0.75, 1.5, 2.5 and 3.5 inches. The cone half angle for these models was 8 degrees. The two remaining models were a 60 degree biconic model and a laminar ablated shape model. All of the models were grit blasted to obtain a uniformly distributed roughness of approximately 3.5 mils.



## SECTION 2

### DESCRIPTION OF CALORIMETER MODELS

The calorimeter models are described here; details of model fabrication are discussed in Section 3.1, and the surface roughness is characterized in Section 3.2.

#### 3.1 MODEL FABRICATION

The six calorimeters used in the Series J experiments are listed in Table 1. The individual configurations are shown in Figures 1 through 6. The 2.5 inch sphere cone (model number 4) is from the PANT Series A tests (Reference 2). This model was fabricated by electroforming nickel on an aluminum mandrel and then machining the shell to nominal wall thickness of 0.080 inch. At this point, the shell configuration was weighed and the wall thickness measured. The shell was then roughened via grit blasting and reweighed. The base of the shell was electron beam welded to a stainless steel flange to facilitate mounting in the tunnel. The five other models were machined from wrought nickel 200 to nominal wall thickness of 0.080 inch. The models were weighed and wall thickness measurements taken. The models were then grit blasted over the entire instrumented surface, and reweighed. Pretest photographs of the 0.75 inch sphere cone calorimeter, 1.5 inch sphere cone calorimeter and the 60° biconic calorimeter model are given in Figure 7.

Models 4, 18 and 19 were bolted to a stainless steel back plate and attached to the calorimeter sting assembly as depicted in Figure 8. For the remaining models, 16, 17 and 20, conical stainless steel adapters were machined and attached to the models with four set screws spaced 90 degrees apart, as illustrated in Figures 1, 2 and 6. The conical adapter for 1.5 inch sphere-cone model and the 60 degree biconic model were 8 degree truncated cones, whereas for the 0.75 inch sphere-cone model the adapter was a 12 degree truncated cone. Twelve degrees was selected in order to minimize both the length of the adapter and the extent of laminar boundary layer separation. The conical stainless steel adapters were attached to the low temperature ablator sting assembly as indicated in Figure 9.

TABLE 1  
MODEL DEFINITION

Model Number	Configuration	Figure
4*	Sphere-cone, 2.5 inch nose radius/ 8 degree cone half angle	3
16	Sphere-cone, 0.75 inch nose radius/ 8 degree cone half angle	1
17	Sphere-cone, 1.5 inch nose radius/8 degree cone half angle	2
18	Sphere-cone, 3.5 inch nose radius/8 degree cone half angle	4
19	Laminar-blunt shape, 3.5 inch shoul- der radius	5
20	Biconic, .25 inch nose radius/60 degree forecone half angle/8 degree aftcone half angle	6

\*Model was previously tested in the PANT Series A program.

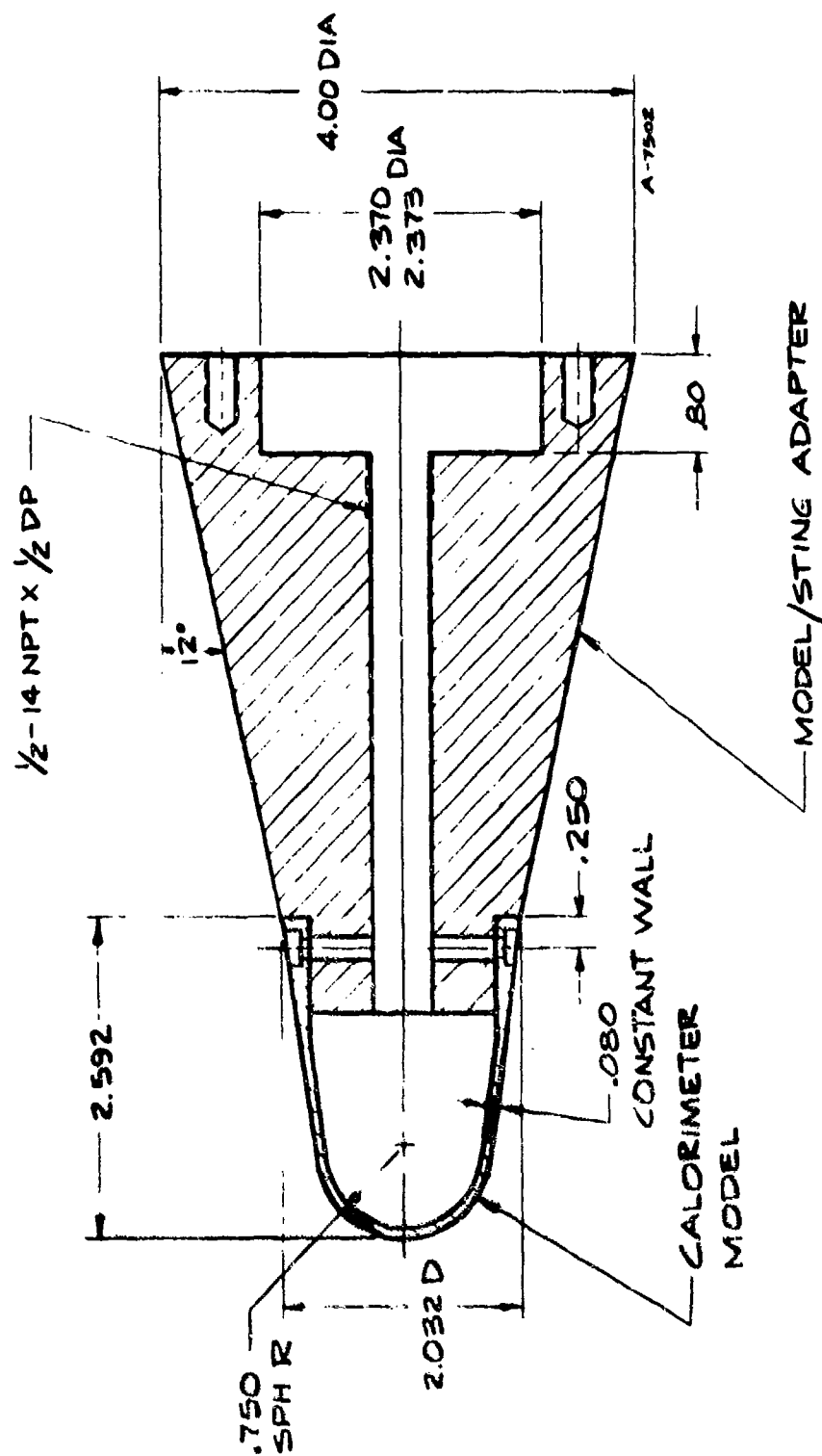


Figure 1. Configuration for .75 Inch Sphere-Cone Calorimeter and Adapter

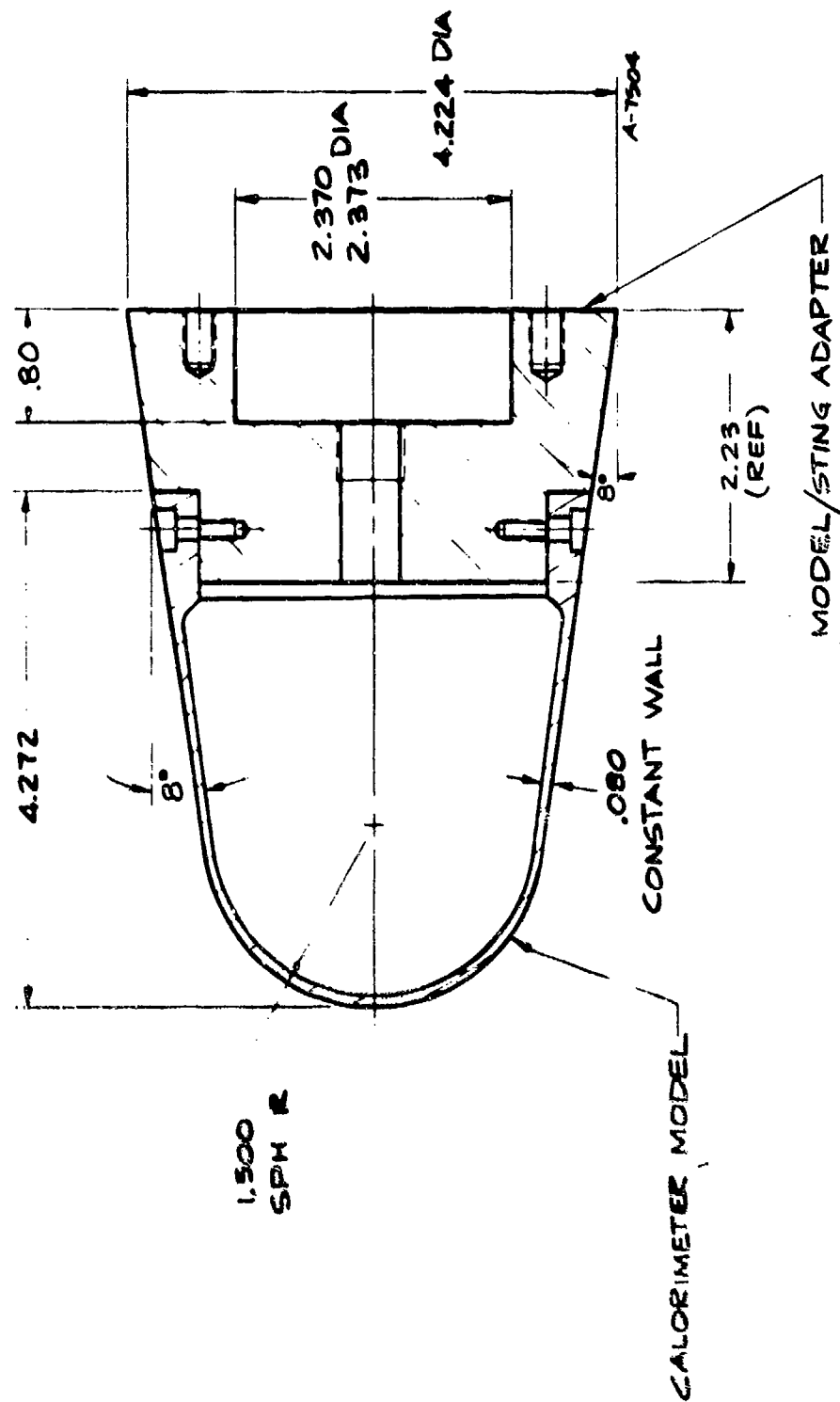


Figure 2. Configuration for 1.5 Inch Sphere-Cone Calorimeter and Adapter

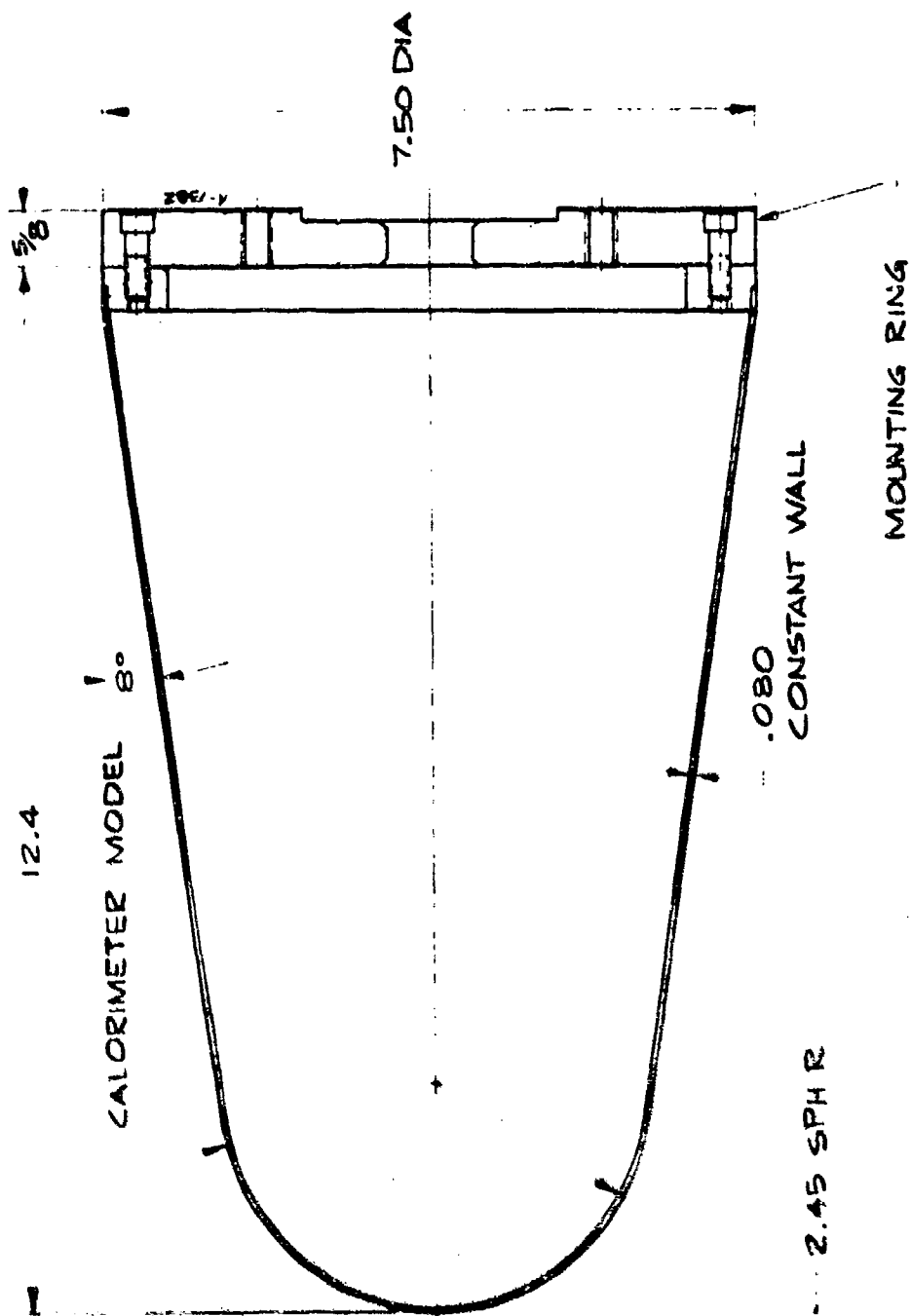


Figure 3. Configuration for 2.5 inch Sphere-Cone Calorimeter and Mounting Ring.

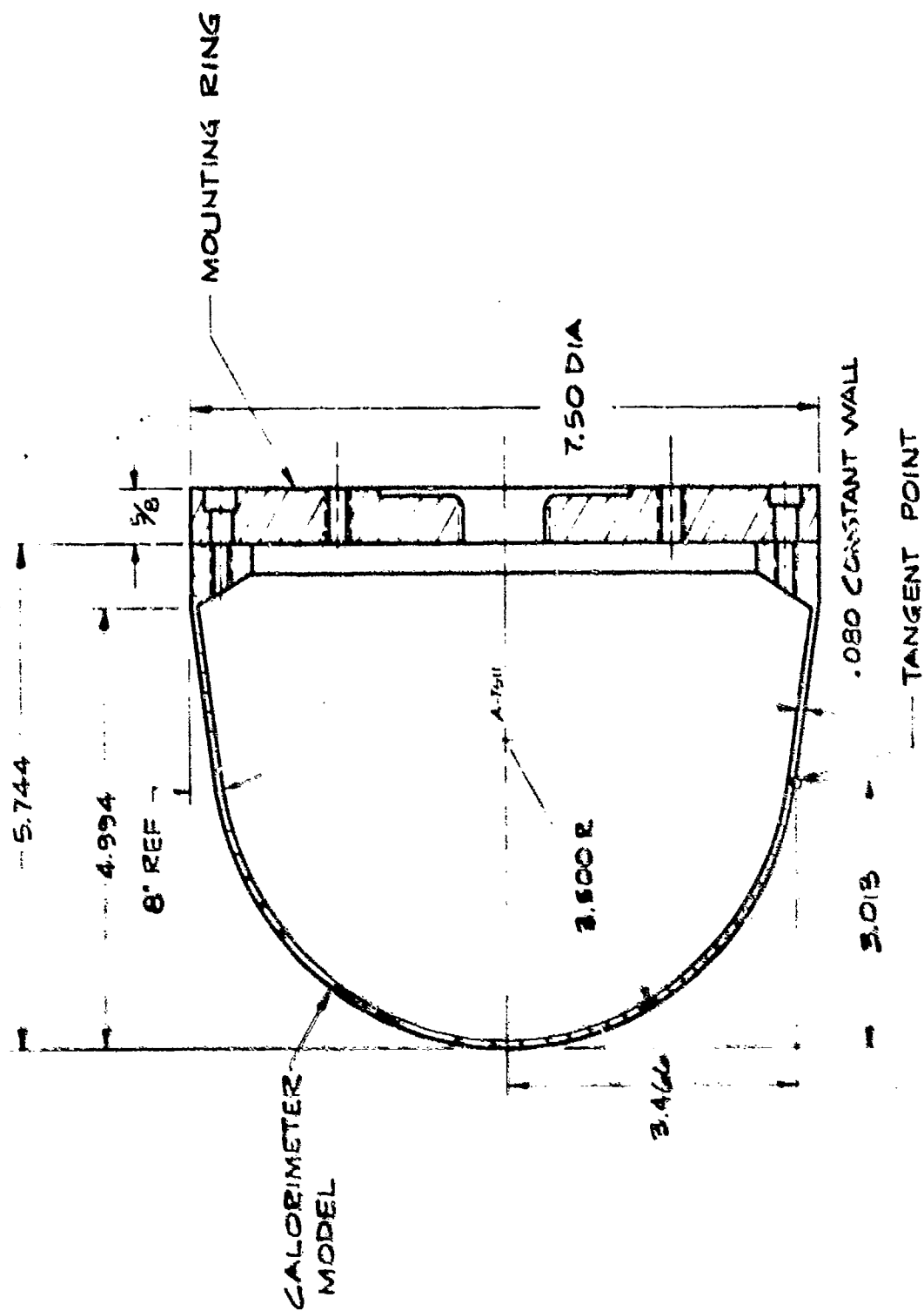


Figure 4. Configuration for 3.5 Inch Sphere-Cone Calorimeter and Mounting Ring

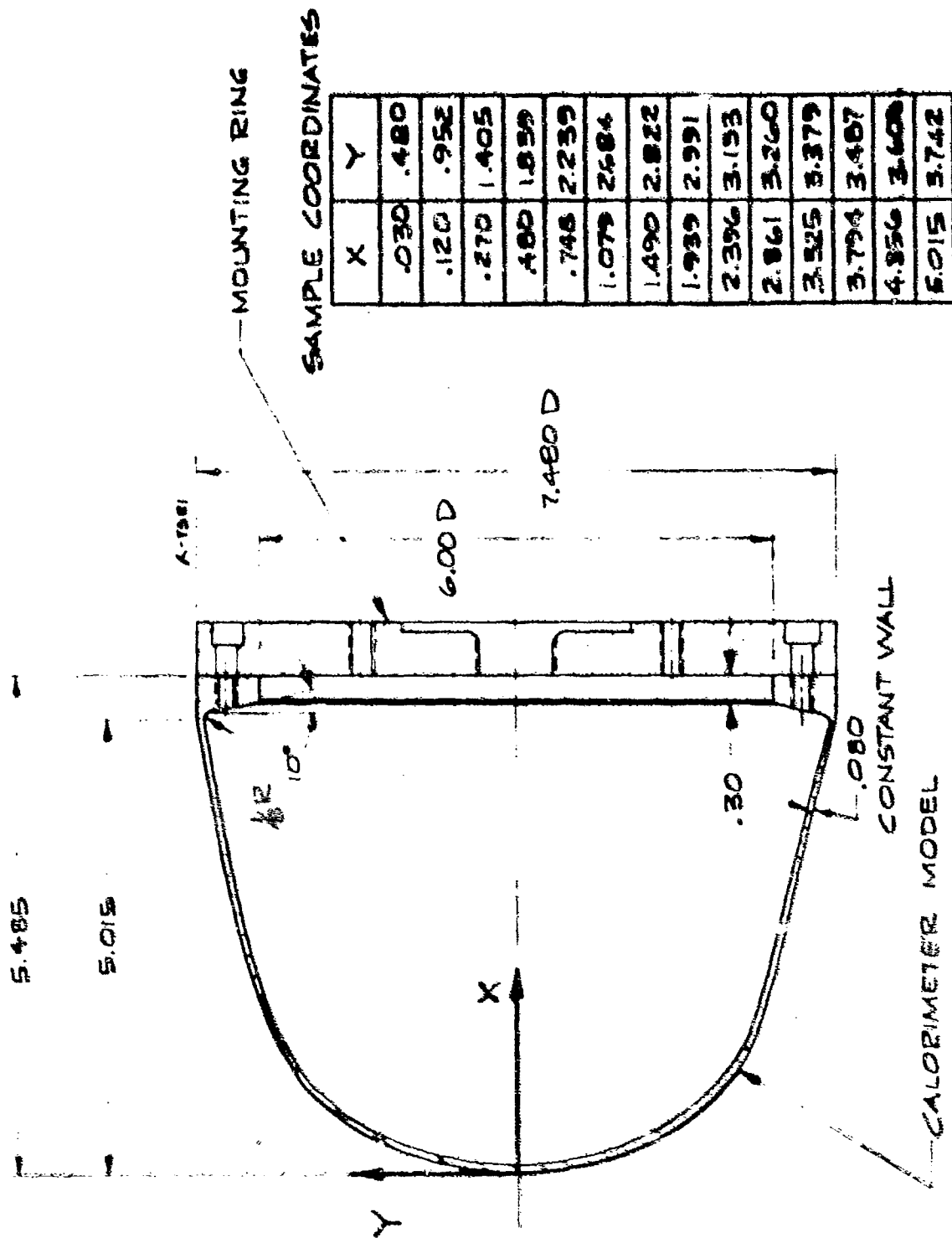


Figure 5. Configuration for 3.5 inch Laminar-Blunt Calorimeter and Mounting Ring

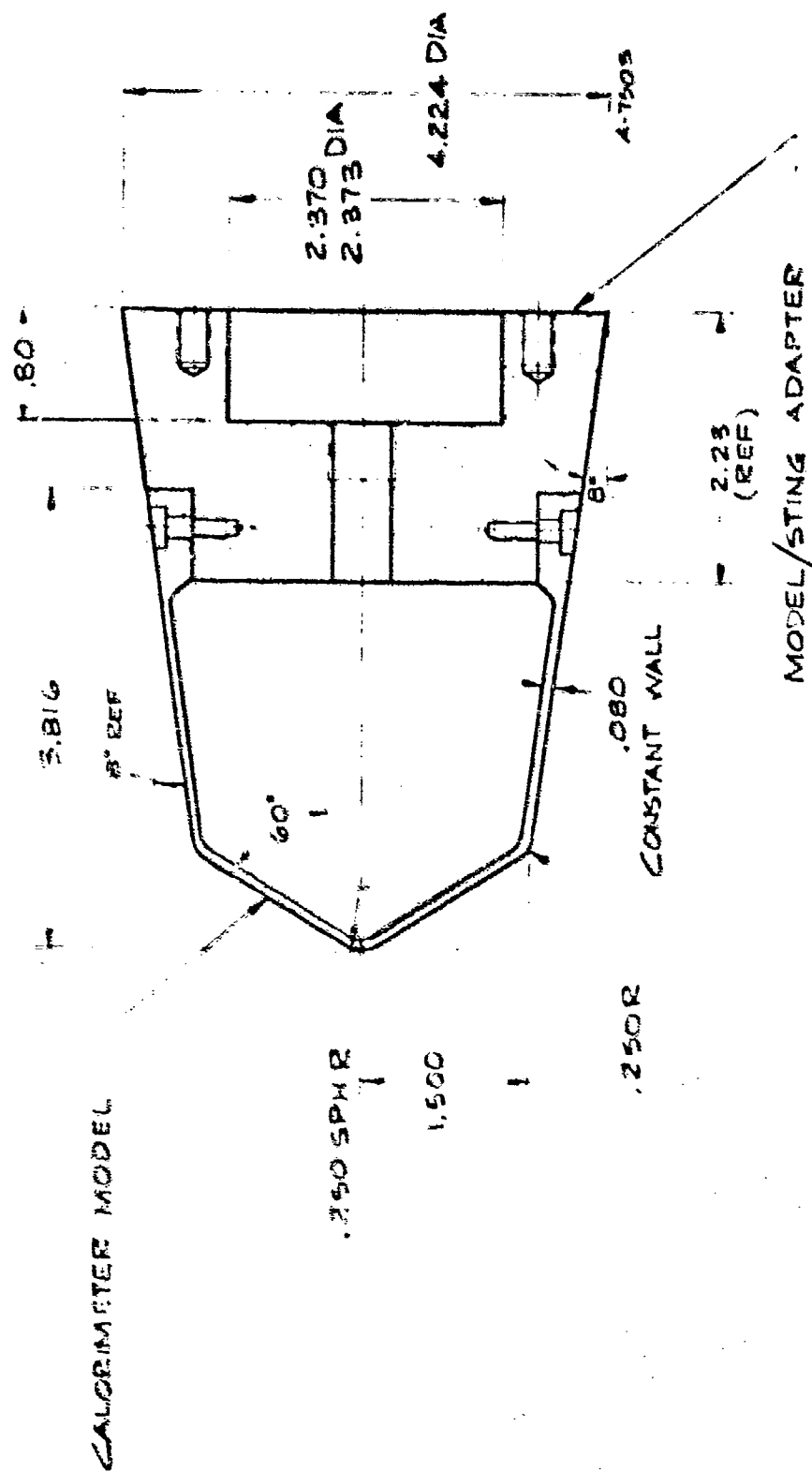
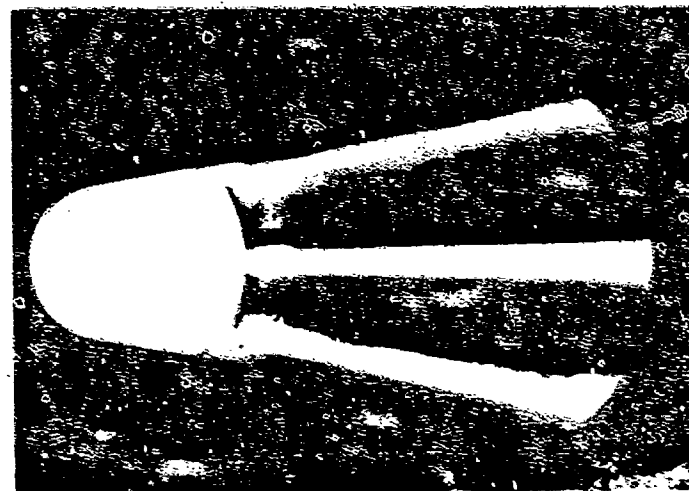
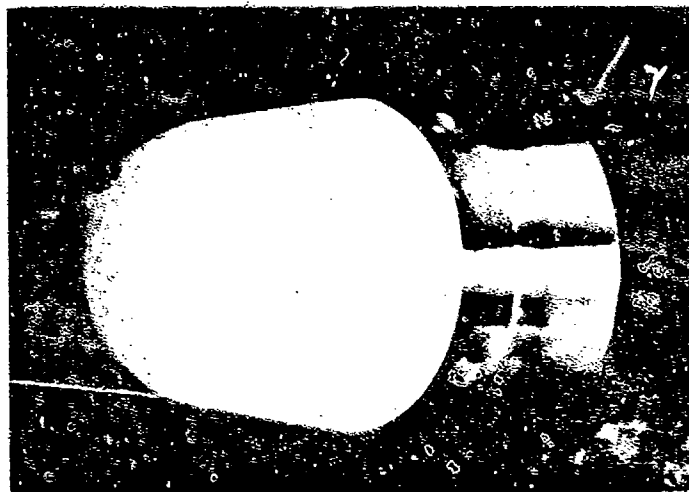


Figure 6. Configuration for 1.5 Inch Shoulder Radius/60 /8 Bionic Calorimeter and Adapter

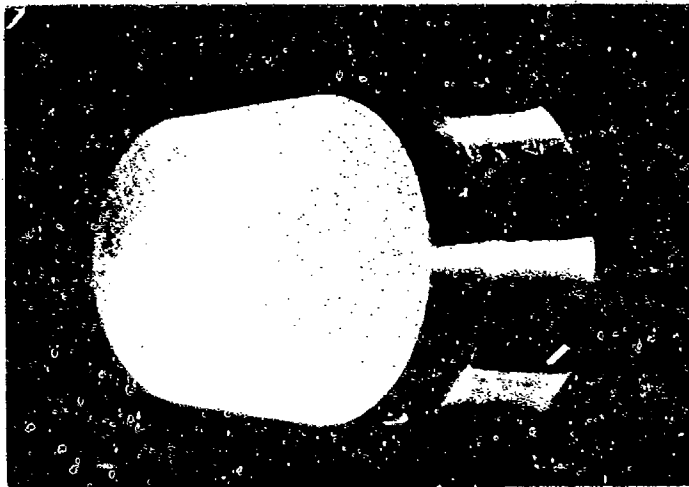




0.75-Inch Sphere Cone Model



1.5-Inch Sphere Cone Model



60 Degree Biconic Model

Figure 7. Pretest Photographs of .75, 1.5 Sphere Cone Models and Biconic Model

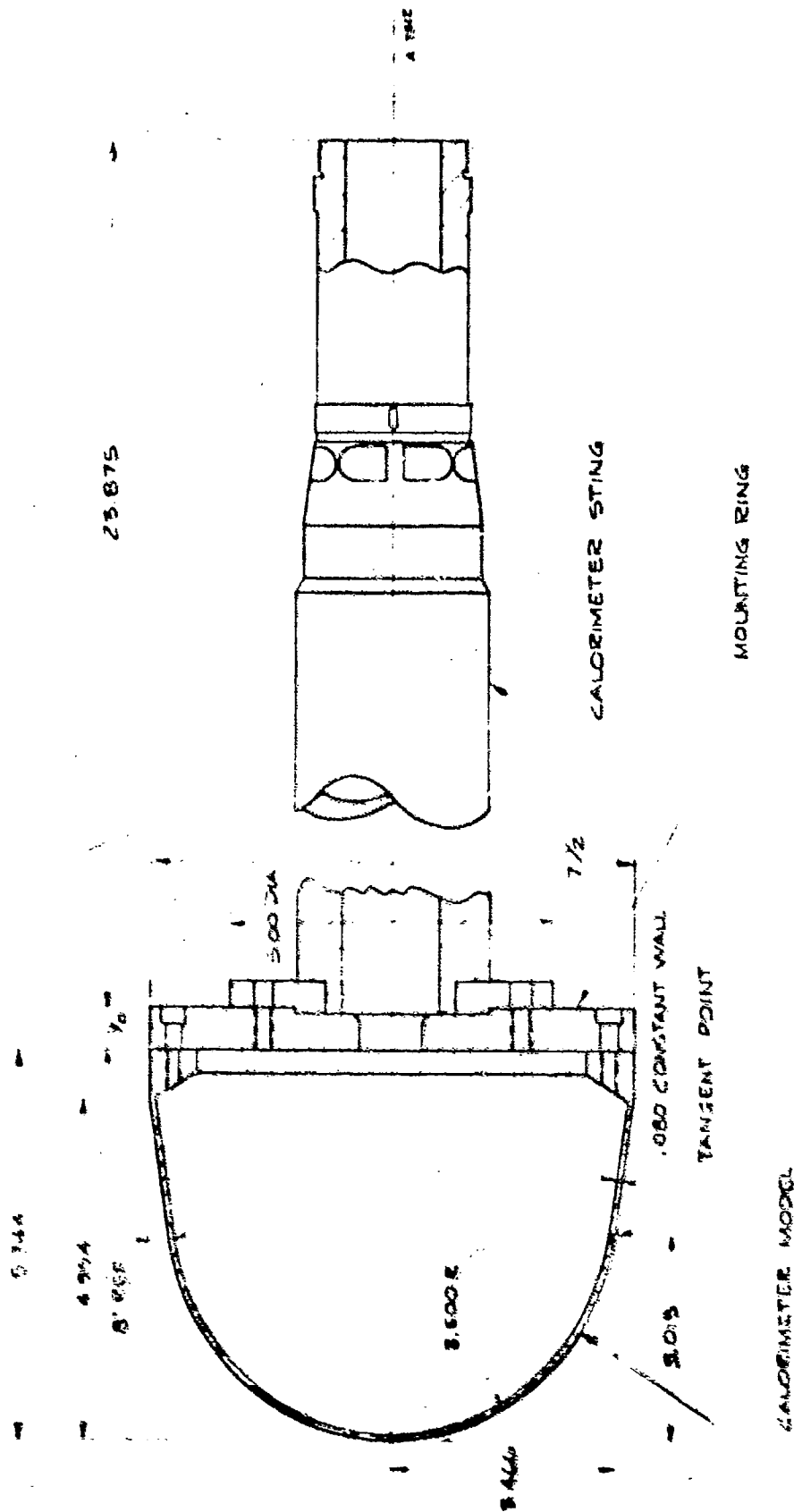


Figure 6. Assembly Configuration for 2.5 Inch Sphere-Cone Calorimeter (2.5 Inch Sphere-Cone and 2.5 Inch Linear Ablated Shape Models also used Calorimeter Sting)

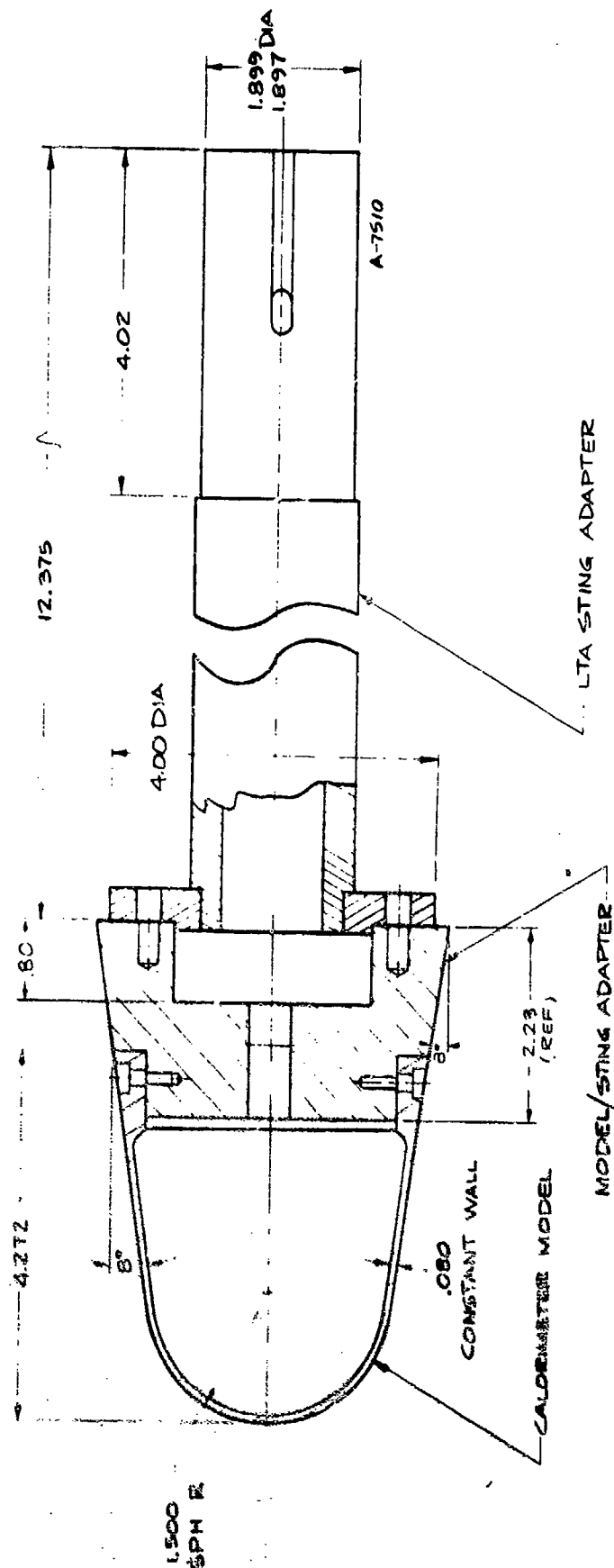


Figure 9. Assembly Configuration for 1.5 Inch Sphere-Cone Calorimeter ( 60° Biconic Calorimeter and .75 Inch Sphere-Cone also uses LTA Sting)

The instrumentation employed on the calorimeter models consisted of spot welding chromel/alumel thermocouples to the interior surface of the models. The chromel/alumel thermocouples were fabricated from 36 gauge (5 mil) wire and special connecting pins were installed on the ends of the wires for ease of installation during model setup at the wind tunnel facility. The thermocouple locations for the calorimeter models are defined in Figures 10 through 15. As indicated by these figures, the number of thermocouples for each calorimeter are as follows:

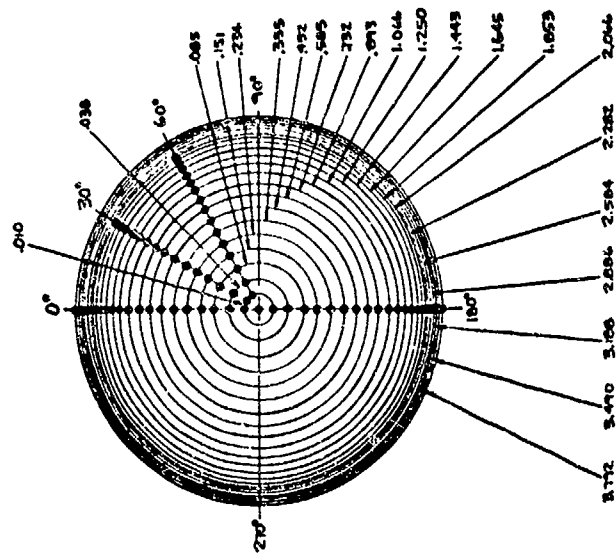
<u>Model Configuration</u>	<u>No. of TC's</u>
.75 inch sphere cone	39
1.5 inch sphere cone	58
2.5 inch sphere cone	78
3.5 inch sphere cone	78
3.5 inch laminar ablated shape	78
60°/8° biconic	58

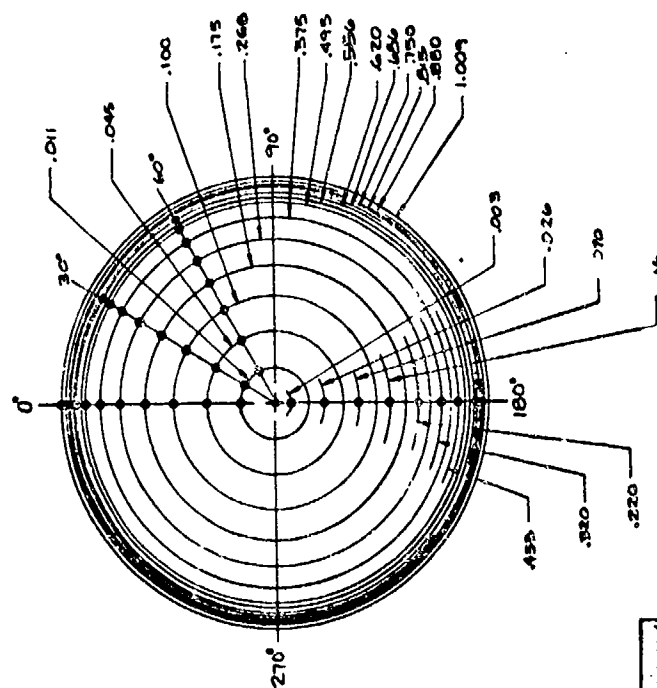
### 3.2 DEFINITION OF SURFACE ROUGHNESS

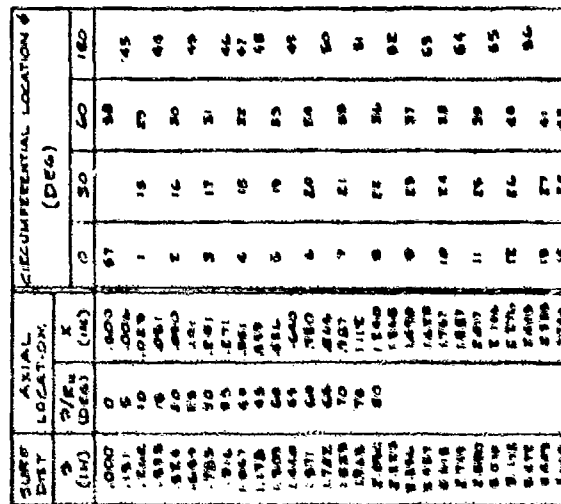
A nominal peak-to-valley roughness height of 3 mils was selected for the Series J calorimeter models. This roughness height normalized by either the boundary layer momentum thickness or displacement thickness obtainable in the NOL hypersonic wind tunnel on the Series J models closely simulates  $k/\theta$  or  $k/\delta^*$  for nosetip materials such as carbon composites or ATJ-S over the flight range of interest. The roughening technique used, grit blasting, yields a uniformly distributed roughness character, which in addition closely simulates the surface roughness character of an ablating graphite (Reference 5).

As indicated above, model number 4 was previously fabricated for the Series A test program. The nominal peak-to-valley, surface roughness was determined to be 3 mils by photomicrographs and profilometer measurements (Reference 5). These same techniques, i.e., cross section photomicrographs and profilometer measurements, were used to characterize the surface roughness height on the Series J models.

The procedure for obtaining cross section photomicrographs is briefly outlined below. Specimens of Nickel 200 were grit blasted simultaneously with the actual models. These specimens were compared visually with the actual models and were found to be quite representative of the surface roughness obtained on the models. The specimens were carefully cross sectioned and photomicrographs taken. Figure 16a shows two photomicrographs of a Nickel 200 sample. Whereas, Figure 16b (taken from Reference 2) shows a photomicrograph of an electroformed nickel sample. Note that the captions in these figures give specific details relative to the fabrication of each roughness.







3-15

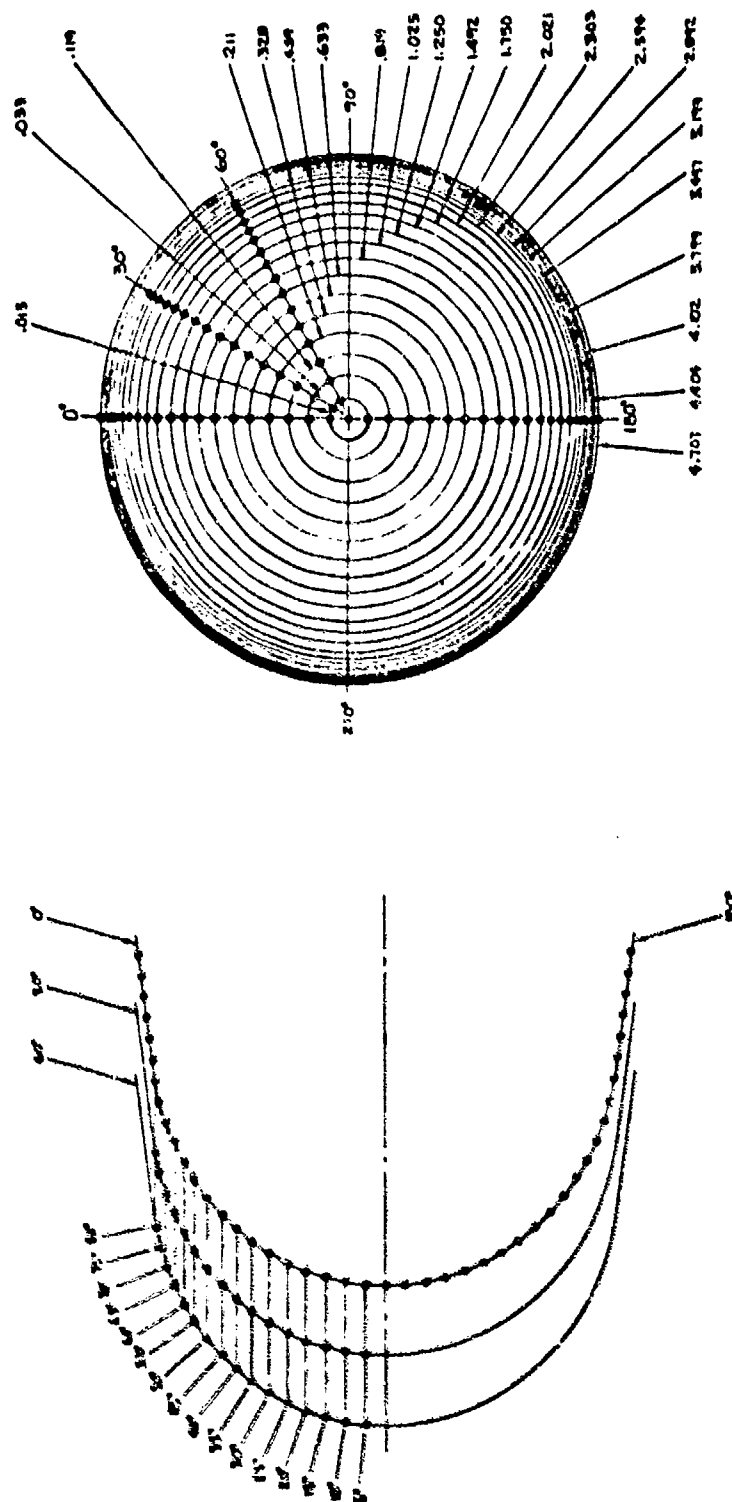
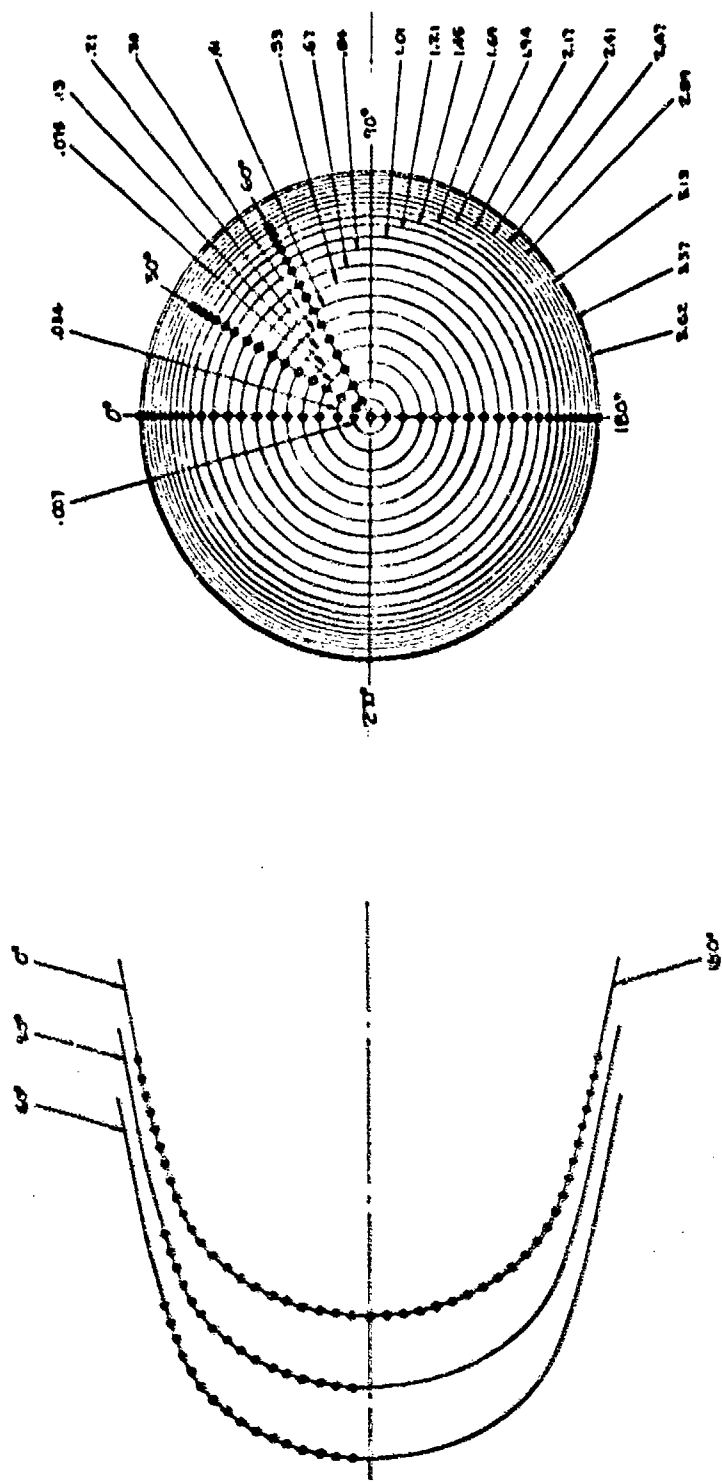
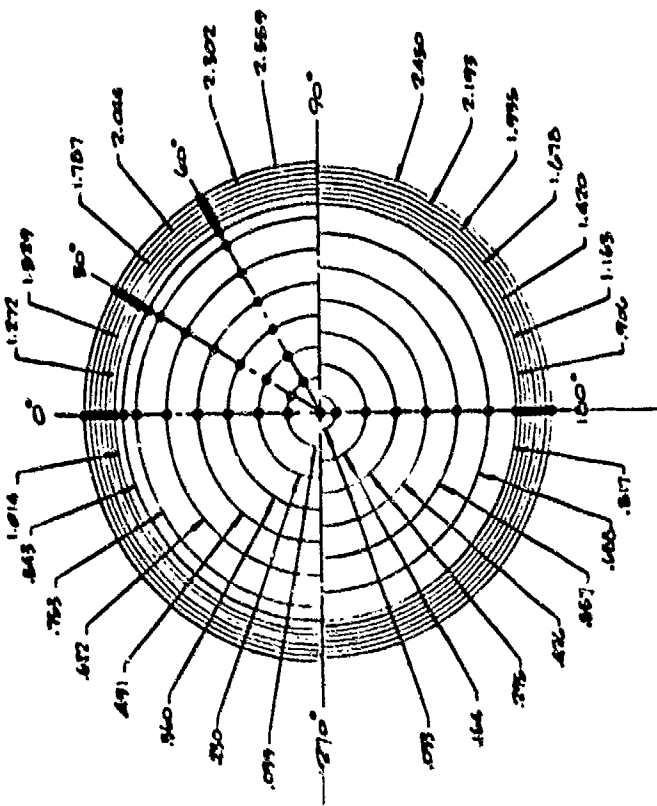


Figure 13. Definition of Thermocouple Locations for 3.5 Inch Sphere Cone Model

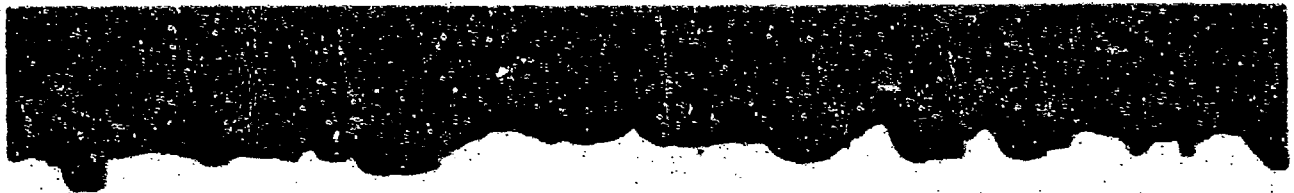








a. Nominal 3.5 Mil Roughness, Nickel 200  
50x  
Grit Blasted Using G-18 Steel Grit  
Pressure Fed Gun, Supersonic Nozzle,  
100 psi



b. Nominal 3.0 Mil Roughness, Electroformed Nickel  
50x  
Grit Blasted Using G-18 Steel Grit  
Pressure Fed Gun, Supersonic Nozzle, 100 psi

Figure 16. Cross Section Photomicrographs of Rough  
Wall Calorimeter Surface Specimens

From the lower photomicrograph shown in Figure 16a, a "nominal" roughness height can be determined as illustrated in Figure 17. Note that this measurement considers the distance between the significant peaks and the significant valleys, but is not the distance from the very highest peak to the lowest valley.

Profilometer measurements of the surface roughness were also carried out for the Nickel 200 specimens by the Air Force Materials Laboratory.\* A recording Talysurf profilometer was used, and data was analyzed using the SURFR computer program (Reference 6) which computes RMS roughness, roughness amplitude probability density, peak height distribution, Burnett roughness integral, etc. This program also produces a computer plot of the roughness profile.

Figure 18 shows a typical roughness profile output by the SURFR program for a Nickel 200 grit blasted sample. As can be seen in this figure the distance between the high peaks and low valleys is about 3500 microinches or 3.5 mils.

A total of seven profilometer traces were made on the Nickel 200 sample. The RMS roughness range was from .683 mil to 1.16 mils with a mean RMS value of .908 mil. It was found in Reference 5 that the peak-to-valley roughness height was approximately 3.6 times the RMS roughness height. Figure 19 illustrates this relationship for both the electroformed nickel calorimeters (Series A) and the Nickel 200 Calorimeters (Series J). The fact that this relationship exists indicates consistency between assigned peak-to-valley roughness heights and measured RMS roughness heights.

In summary, the peak-to-valley roughness height for the Series J models fabricated from Nickel 200 is 3.5 mils. Although the Nickel 200 calorimeter models are rougher than the 3 mil electroformed nickel calorimeter, the data presented above indicates that the roughness character is basically very similar.

\* These measurements were performed through Mr. Gary Denman of AFML/AMS. Mr. Denman's assistance in this regard is gratefully acknowledged.

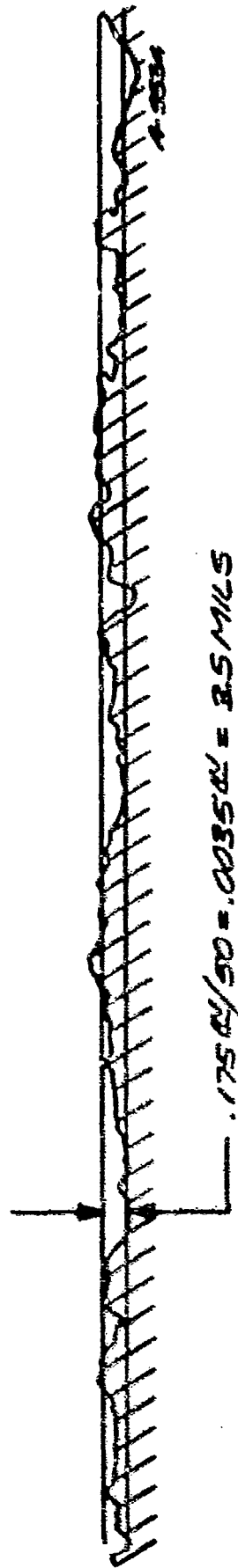


Figure 17. Sketch Indicating Definition of Nominal Surface Roughness Height (Surface Traced from 3.5 Mil Grit Blasted Surface Photomicrograph, 50x)

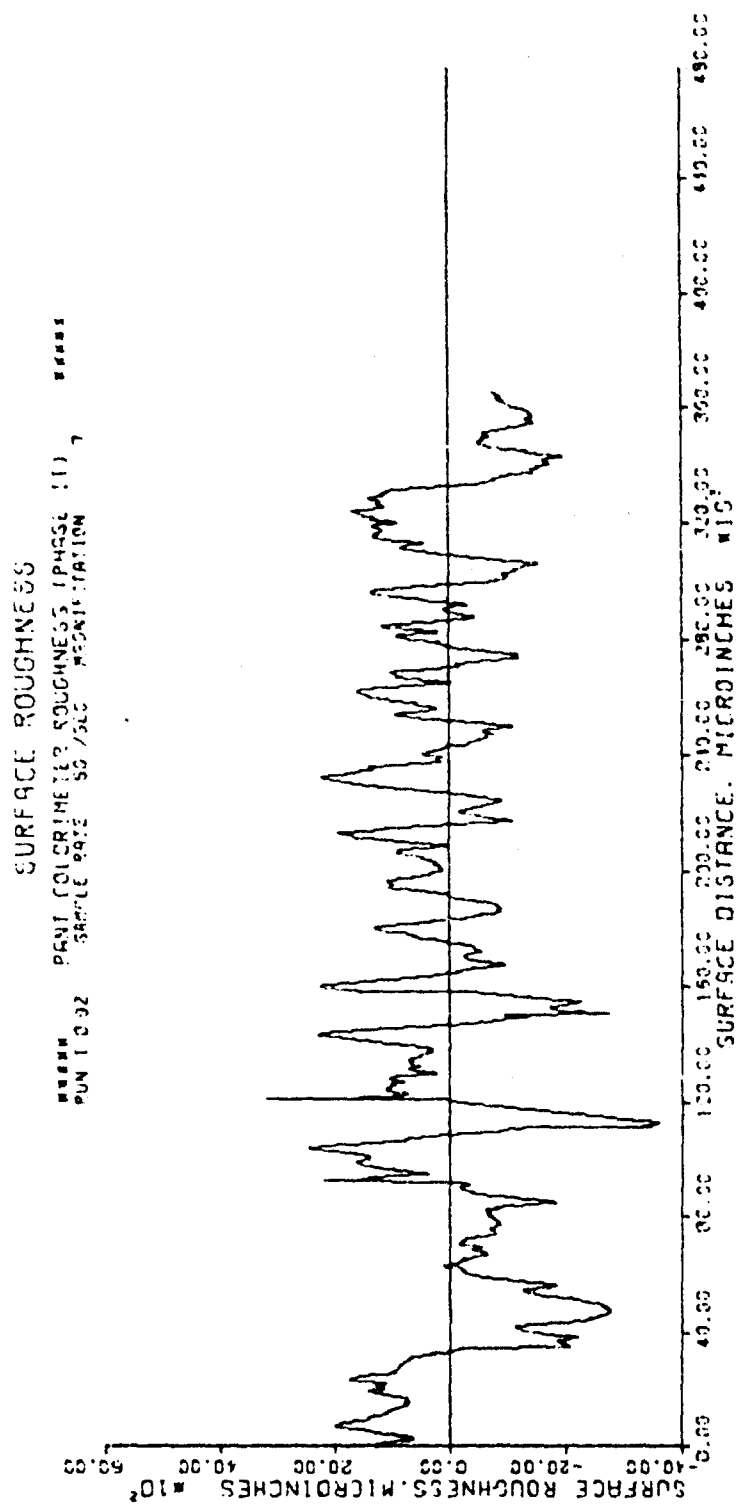


Figure 18. Typical AFML Profilometer Measurement of Nickel 200  
Calorimeter Surface Roughness

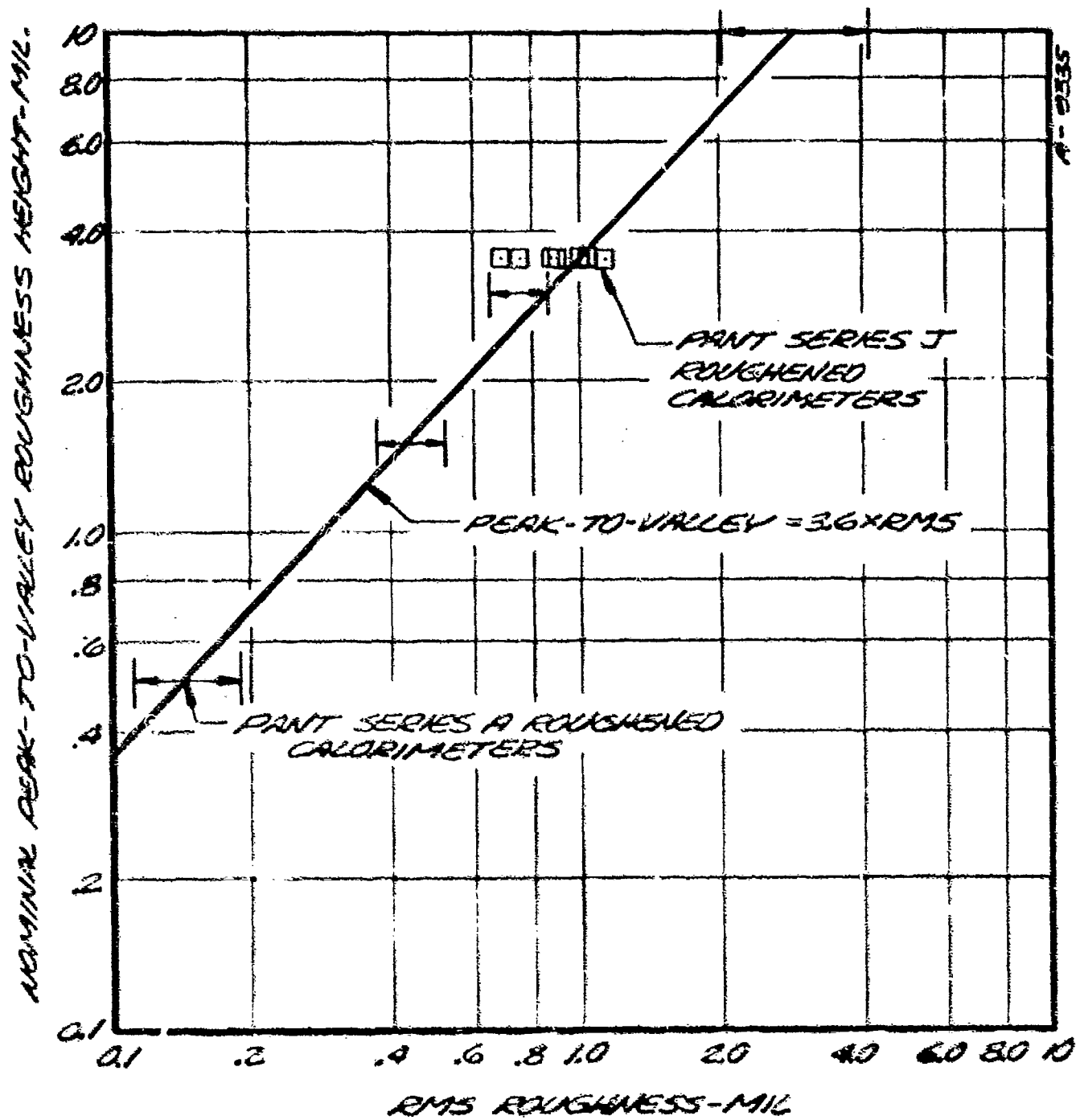


Figure 19. Summary of AFIE Profilometer RMS Measurements

## SECTION 4

### TEST CONDITIONS

The wind tunnel selected for the Series J experiments was Tunnel Number 8 at the Naval Ordnance Laboratory (NOL). This tunnel was chosen based on its capability of producing large enough sonic point unit Reynolds numbers to promote blunt body boundary layer transition (Reference 7). The NOL Tunnel Number 8 is an intermittent blowdown hypersonic wind tunnel in which heated air is the working gas. Air is compressed and stored in high pressure containers. In transit to the nozzle, the air is heated in a pebble bed heater which can be supplemented by an electric resistance heater when the required air temperature exceeds 1150°F. The tunnel has an open jet test section and a constant geometry diffuser. Nozzle selection is dependent on the required Mach number.

The free stream Mach number for this test series was  $M_\infty = 5$ . The associated nozzle is rectangular with throat dimensions of 0.642 inch by 16.60 inches and exit dimensions of 17.37 inches by 16.97 inches. The resulting Reynolds number operating envelope at Mach 5 is presented in Figure 20 as a function of supply temperature and pressure. Superimposed on this figure are the nominal operating conditions which were run during this test series. The average measured test conditions are summarized in Table 2.

At the supply temperatures required for the Series J experiments, film cooling of the nozzle throat is necessary in order to prevent nozzle degradation. Prior to this test series NOL performed detailed flow measurements in the Mach 5 nozzle in order to establish the effect film cooling on the test section flow field (Reference 8). These measurements included free-stream Mach number, total temperature, flow angularity, and pressure fluctuations. Of these parameters, pressure fluctuations were found to be most sensitive to film cooling rates. This is significant since these fluctuations may severely affect the interpretation of boundary layer transition data.

Indeed, the subject of wind tunnel noise and its effect on boundary layer transition has been discussed many times in the literature, see for instance, References 9, 10 and 11. For hypersonic ( $M_\infty > 3$ ) wind tunnels the primary mode of aerodynamic noise is believed to be the sound waves originating from the turbulent tunnel wall boundary layers. This type of disturbance manifests itself primarily in the form of pressure fluctuations. Figure 21 (taken



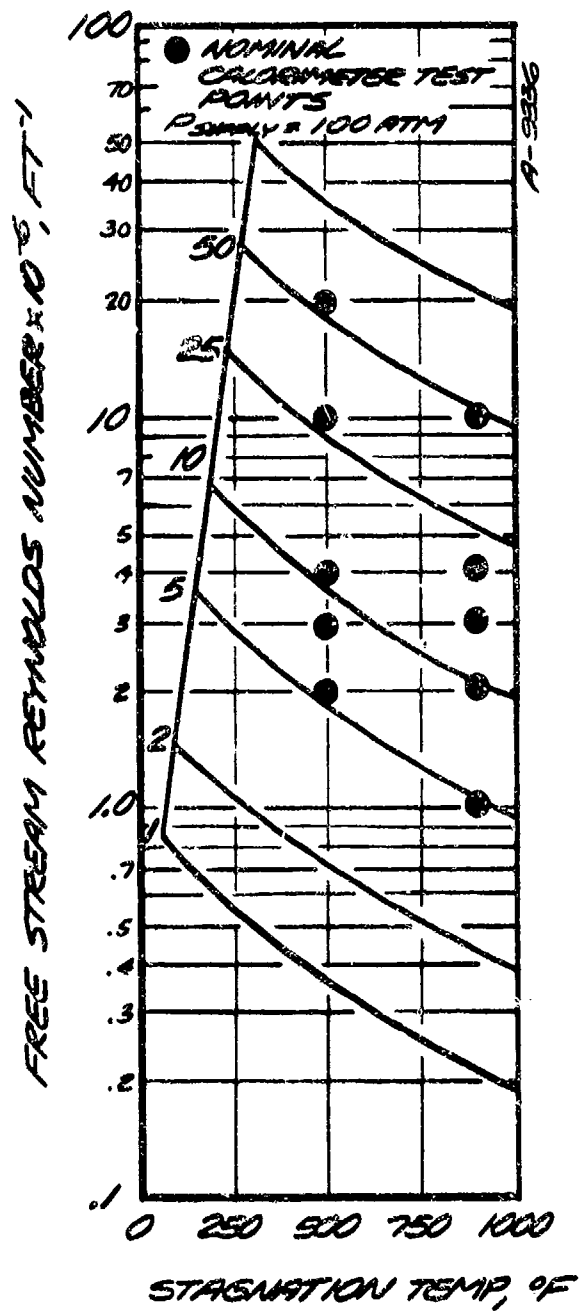


Figure 20. Nominal Test Points at  $M_\infty = 5.0$  in NOL Hypersonic Wind Tunnel

TABLE 2  
ACTUAL TEST CONDITIONS FOR PANT SERIES J WIND TUNNEL TESTS

Run No.	Model No.	Model Description**	k (mils)	Supply Conditions			Free Stream Conditions		
				$T_s$ ( $^{\circ}$ F)	$P_s$ (psia)	Film Cooling $\Delta P_f$ (psi)	$M_{\infty}$	$Re_{\infty}$ ( $10^6$ /ft)	$Re^*$ ( $10^6$ /ft)
601	4	2.5 in. $R_N$ Sphere/cone	3.0	843	127	20	4.97	1.94	.83
602				865	134	30	4.97	2.00	.85
603				847	129	20	4.98	1.96	.83
604				873	250	30	4.99	3.67	1.59
605	18	3.5 in. $R_N$ Sphere/cone	3.5	878	142	20	4.98	2.08	.90
606				871	73	12	4.95	1.09	.45
607				879	107	15	4.96	1.58	.67
608				898	279	30	4.99	3.98	1.74
609				520	86	12	4.95	2.04	.78
610				526	117	15	4.96	2.74	1.05
611				505	181	20	4.97	4.31	1.67
612	16	.75 in. $R_N$ Sphere/cone		911	283	30	4.99	3.98	1.75
613				898	155	20	4.98	2.22	.96
614				885	109	15	4.96	1.60	.67
615				889	130	30	4.97	1.89	.81
616				904	186	22	4.97	2.66	1.15
617				900	212	30	4.98	3.04	1.32
618	17	1.5 in. $R_N$ Sphere/cone		844	122	17	4.97	1.87	.79
619				851	149	20	4.98	2.25	.96
620				859	272	30	4.99	4.05	1.76
621				845	181	20	4.98	2.75	1.18
622				555	103	10	4.96	2.31	.89
623				568	126	12	4.96	2.77	1.08
624				513	181	20	4.97	4.31	1.66
625				857	91	10	4.96	1.38	.58
626				859	89	30	4.95	1.35	.56
627				855	70	10	4.95	1.07	.44
628	20	Biconic, $R_S = 1.5$ in.		865	275	30	4.99	4.07	2.53
629				848	139	20	4.97	2.12	1.28
630				834	68	10	4.95	1.06	.52
631				839	101	10	4.97	1.55	.86
632				849	168	20	4.98	2.54	1.57
633				731	509	30	5.00	8.79	5.32
634	19	Laminar Ablated Shape, $R_S = 3.5$ in.		479	439	30	5.00	10.90	4.70
635				515	829	30	5.00	19.41	7.59
636				865	276	30	4.99	4.09	1.78
637				825	62	10	4.95	.98	.42
638				839	135	20	4.97	2.08	.90
639				819	101	10	4.97	1.59	.68
640				831	162	20	4.98	2.37	1.08

\* All runs at zero angle-of-attack

\*\* All model grit blasted

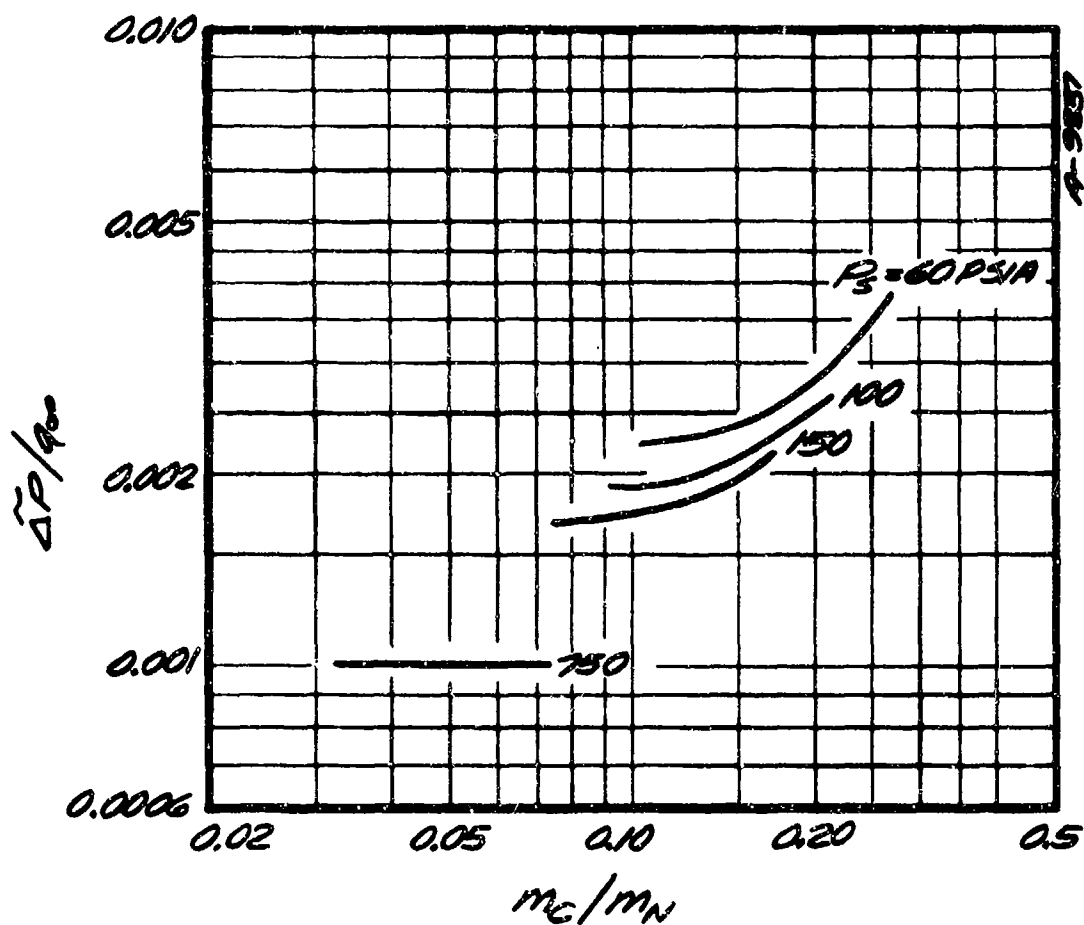


Figure 21. Effects of Mass Addition on RMS Pressure Fluctuations in NOL Hypersonic Tunnel Mach 5 Nozzle

from Reference 8) illustrates the root mean square pressure fluctuations ( $\Delta\tilde{P}$ ) normalized by the dynamic pressure ( $q_\infty$ ) as a function of the mass flow cooling rate ( $m_C$ ) normalized by nozzle flow rate ( $m_N$ ). Two points should be noted. First, film cooling does not affect the pressure fluctuations providing the cooling rates are less than 10 percent of the nozzle flow rate. For higher  $m_C/m_N$ ,  $\Delta\tilde{P}$  increases substantially. Second, the pressure fluctuations increase with decreasing supply pressure or, more conventionally, with decreasing free-stream unit Reynolds number ( $Re_\infty$ ). Figure 22 illustrates this trend. The data upon which this figure is based was obtained for  $m_C/m_N$  less than 0.1.

From the data presented in Figure 21 the normalized RMS pressure fluctuations can be estimated for each run. This was accomplished by relating the film cooling pressure differential given in Table 2 to  $m_C/m_N$ . The resulting normalized mass cooling rate and pressure fluctuations are summarized in Table 3 for each run.

The dependency of the pressure fluctuations on the film cooling mass flow rate indicated an interesting aside to the primary test objectives. By increasing the coolant mass flow it is possible to increase the aerodynamic noise level of the tunnel, and therefore obtain data on the effects of noise on transition. This was tried for two models (4 and 17), cf. Runs 601-602 and 625 and 626. Unfortunately, for Runs 601 and 602 the supply conditions varied enough between the runs to negate the usefulness of this procedure. For Runs 625 and 626, however, this procedure resulted in approximately a 30 percent difference in  $\Delta\tilde{P}/q_\infty$  with essentially constant supply conditions.

As shown in Section 6, both Runs 625 and 626 were laminar, indicating for these conditions that boundary layer transition was not affected by wind tunnel noise.

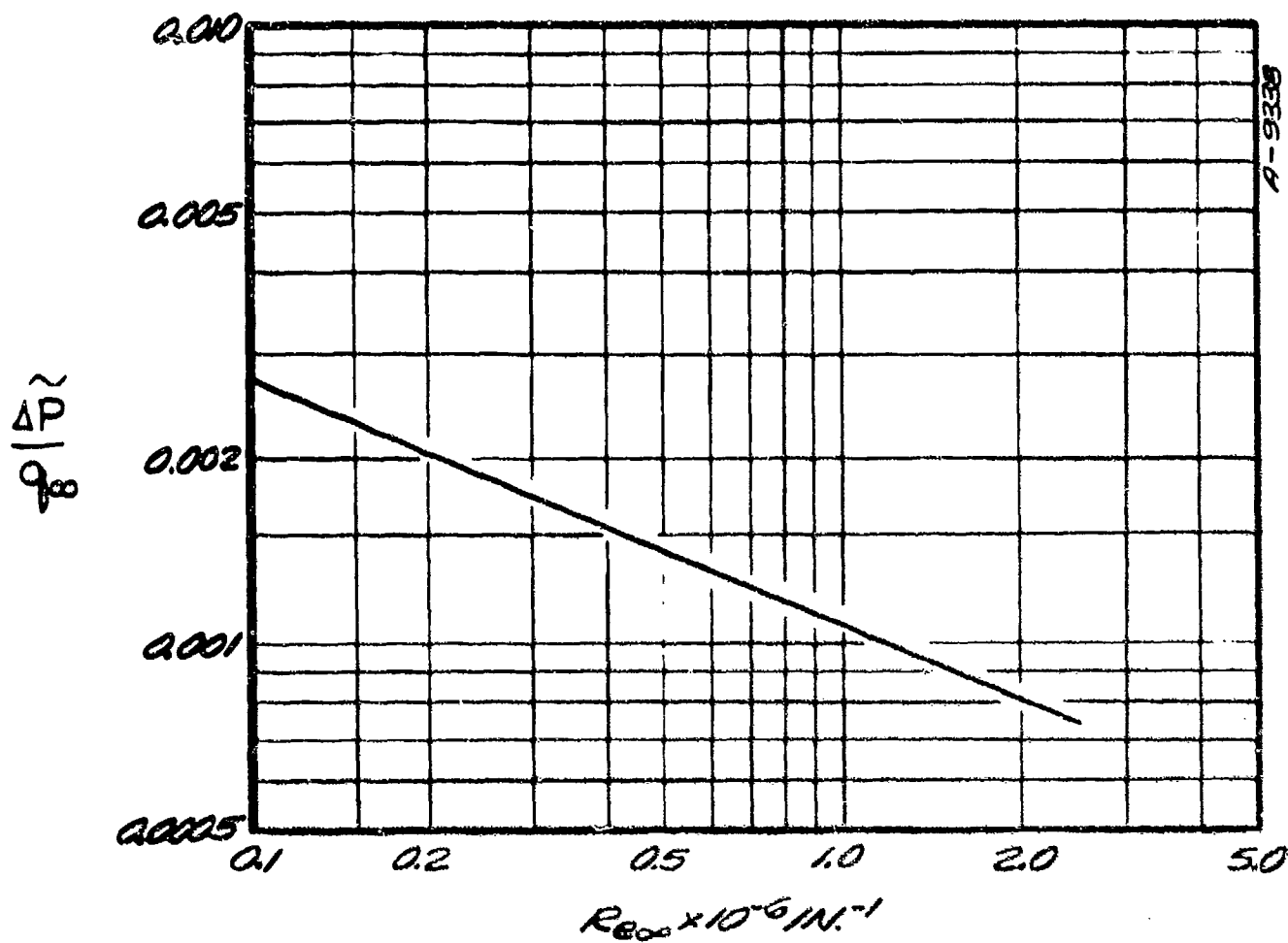


Figure 22. RMS Pressure Fluctuations in NOL Hypersonic Tunnel Mach 5 Nozzle

TABLE 3  
ESTIMATION OF FREE STREAM TUNNEL NOISE

Run No.	Model No.	Film Cooling $\Delta P_f$ (psi)	$\frac{P_C}{P_H}$	$\frac{\Delta P}{Q_c}$
601	4	20	.13	.0019
602		30	.15	.0020
603		20	.13	.0019
604		30	.11	.0016
605	18	20	.12	.0018
606		12	.13	.0022
607		15	.12	.0019
608		30	.11	.0016
609		12	.10	.0020
610		15	.10	.001*
611		20	.09	.0017
612	16	30	.10	.0015
613		20	.12	.0018
614		15	.12	.0019
615		30	.16	.0020
616		22	.11	.0017
617		30	.12	.0017
618	17	17	.12	.0019
619		20	.12	.0017
620		30	.11	.0016
621		20	.11	.0017
622		10	.085	.0018
623		12	.085	.0017
624		20	.093	.0017
625		10	.11	.0019*
626		30	.19	.0025*
627		10	.12	.0022
628	20	30	.11	.0016
629		20	.12	.0018
630		10	.12	.0022
631		10	.10	.0019
632		20	.11	.0017
633		30	.071	.0014
634	19	30	.072	.0013
635		30	.053	.0010
636		30	.10	.0015
637		10	.13	.0023
638		20	.12	.0018
639		10	.10	.0020
640		20	.11	.0018

\* Changed  $w_c$  holding supply conditions approximately constant

## SECTION 5

### DESCRIPTION OF RECORDED DATA

The primary reduced data from the Series J wind tunnel tests were heat transfer coefficient distributions calculated from the recorded thermocouple data for the calorimeter models. The primary data recorded for each calorimeter run were:

- Temperature as a function of time for all thermocouples
- Test section supply temperature and pressure as a function of time
- Sting (or model) position as a function of time
- Approximately 3 Schlieren pictures.

The paragraphs below briefly describe the primary recorded data.

At the NOL wind tunnel test facility, a 14-channel digital recorder is used for recording the test time, the supply pressure, the supply temperature, and the thermocouple temperatures. This recorder has a sampling (or sweep) rate of 0.056 second (i.e., all channels are recorded every 0.056 second). Of the fourteen channels, only thirteen are available for recording the above data. The test time, supply temperature, and supply pressure are each recorded on a separate channel, leaving 10 channels for recording temperature responses of the thermocouples. These 10 channels were multiplexed such that data from each thermocouple were sampled at least every 0.392 second.

The thermocouple data obtained from the calorimeter runs were of excellent quality and samples of typical temperature vs. time plots are shown in Figure 23. In this figure, the digital recorder was turned on at zero time. The initial calorimeter shell temperatures were below local ambient temperatures before the model entered the test stream. Low initial temperatures were achieved by precooling the model using a portion of the available air supply. The thermocouple data presented in Figure 23 are samples from each of the calorimeter models. The nominal free stream sonic point unit Reynolds number ( $Re^*$ ) for these runs is  $2 \times 10^6/\text{ft}$ . The thermocouples presented in this figure are located in the vicinity of the sonic point. A discussion of the technique used to curve fit these temperature histories is given in Section 6.

RUN HAS TOP 0030010

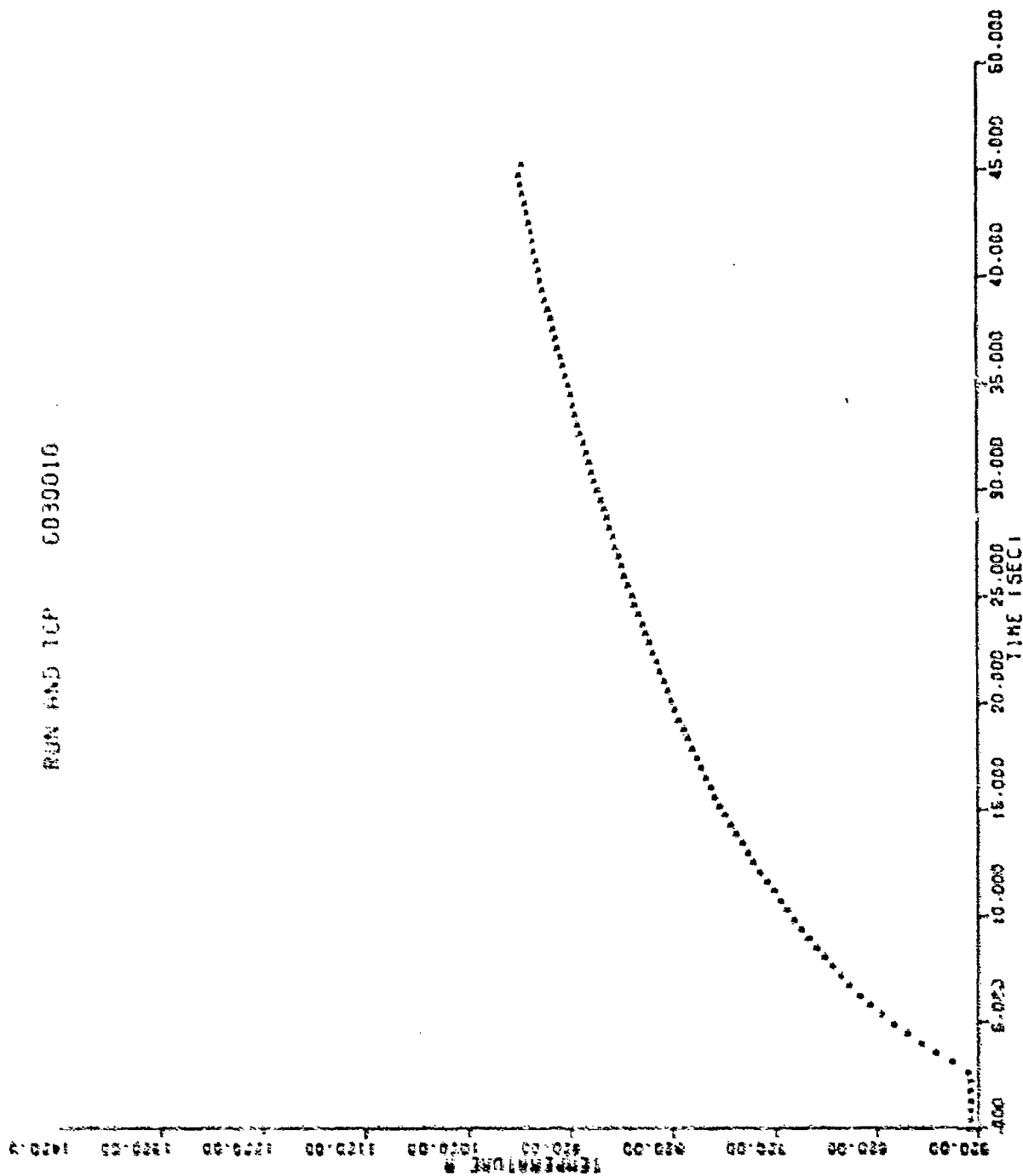


Figure 23. Sample of Measured Thermocouple Histories

4. 2.5 Inch Sphere Cone Model Run 603,  
Thermocouple 10



RUN AND TCP 6090010

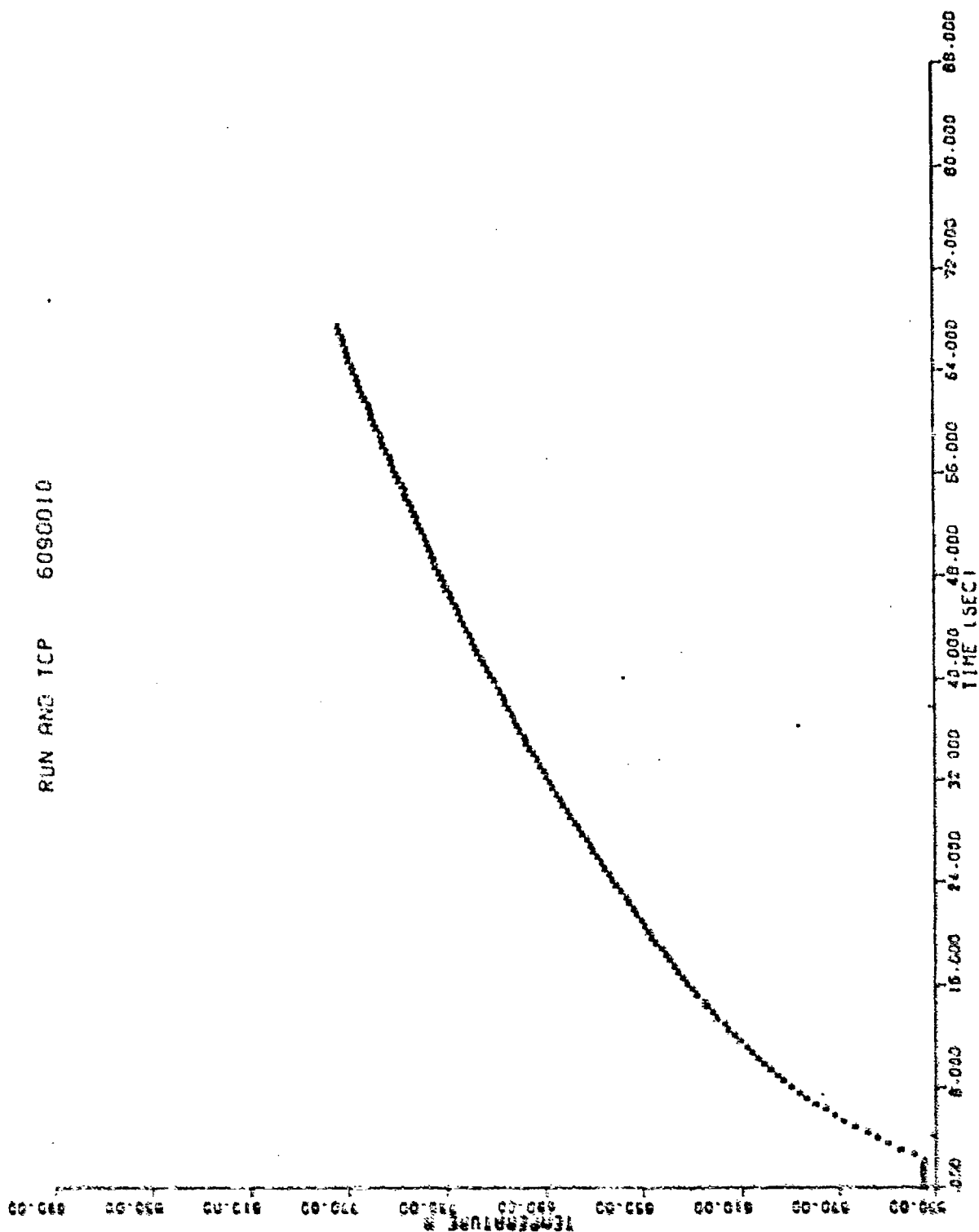


Figure 23. Continued  
b. 3.5 inch Sphere Cone Model  
Run 609, Thermocouple 10

RUN AND TCP 6150025

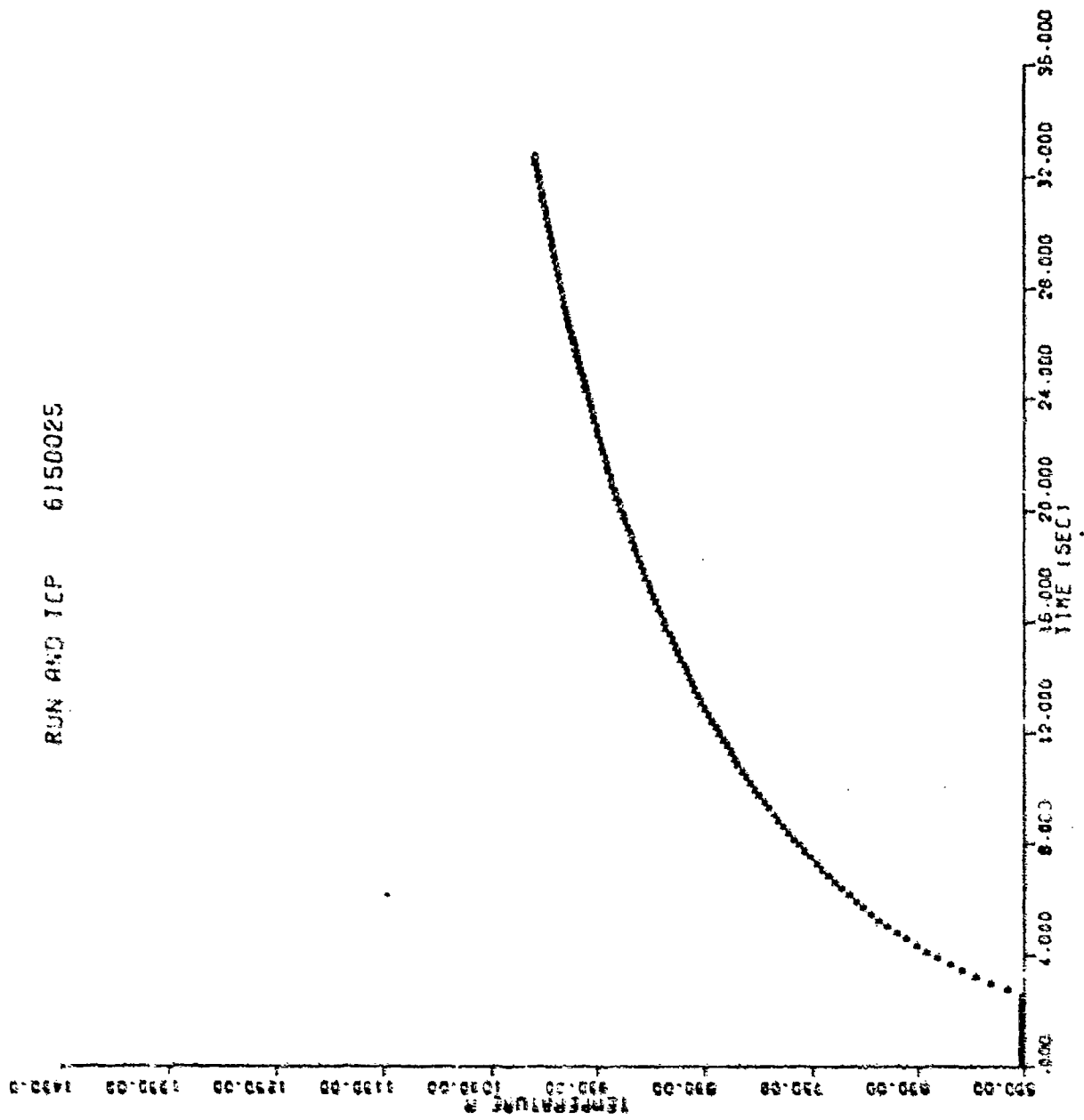


Figure 23. Continued  
c. .75 inch Sphere Cone Model  
Run 615, Thermocouple 25

RUN AND TCP 6180004

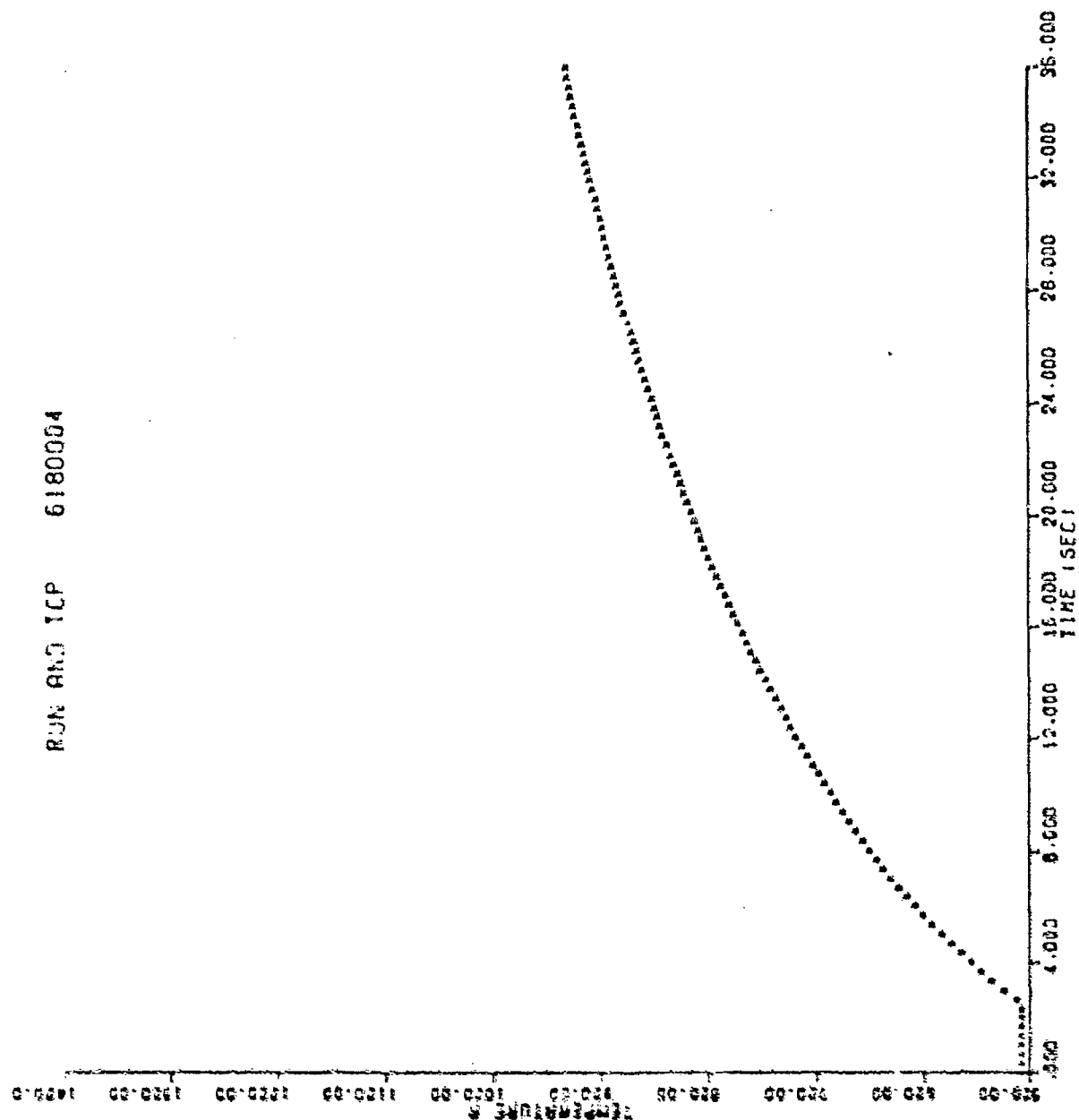


Figure 23. Continued  
d. 1.5 Inch Sphere Cone Model  
Run 618, Thermocouple 4

RUN AND TCR 6290007

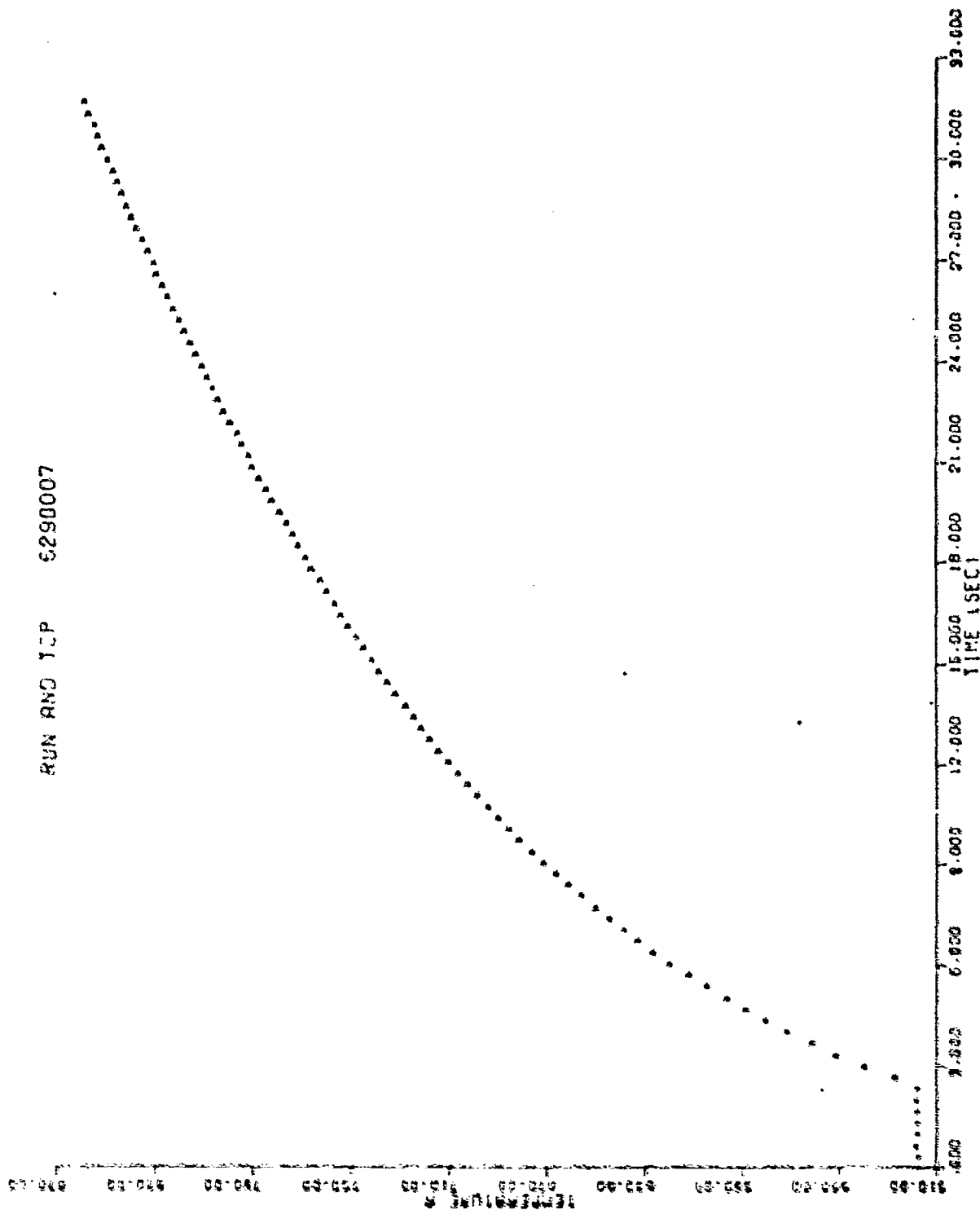


Figure 23. Continued  
 e. Bicomit Model  
 Run 629, Thermocouple 7

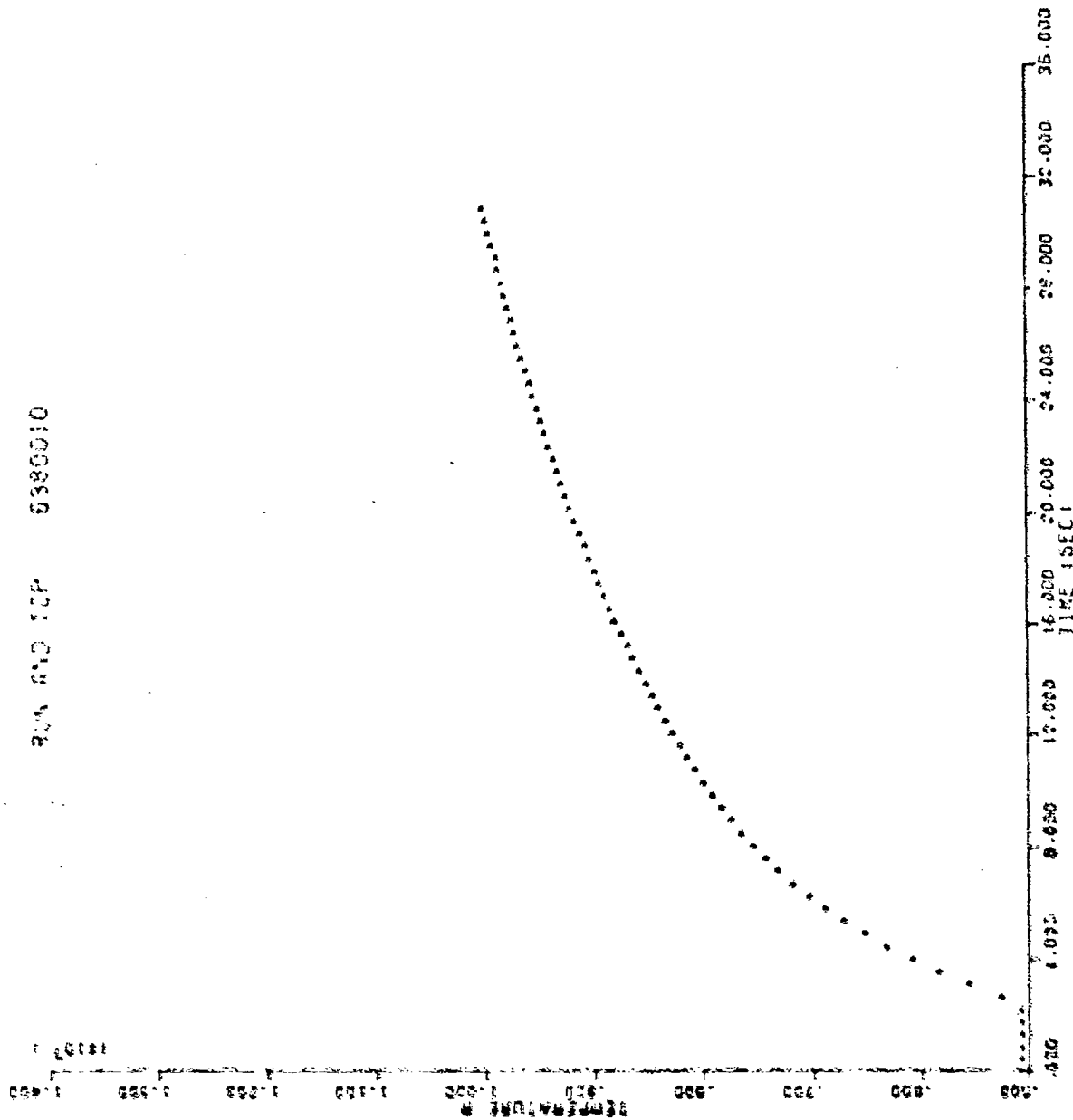
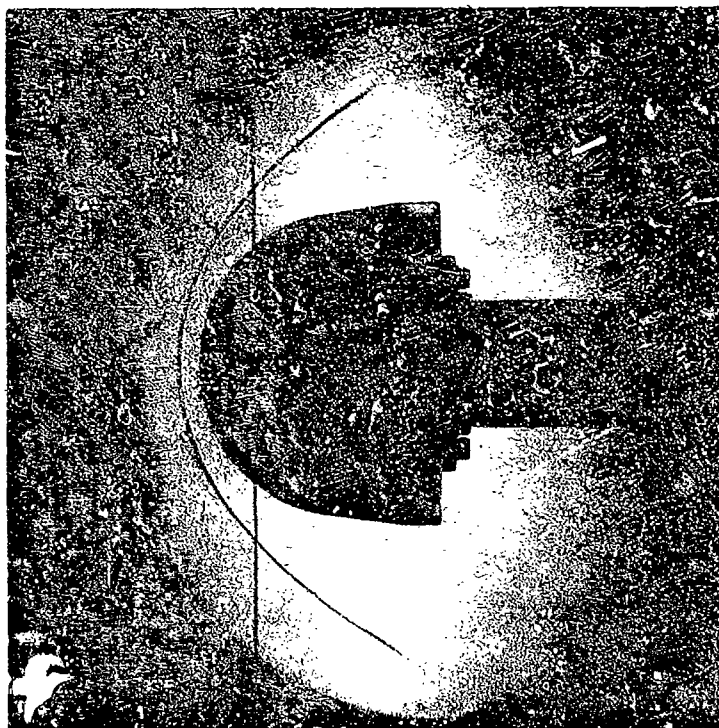


Figure 23. Concluded  
f. Laminar Ablated Model  
Run 638, Thermocouple 10

Shadowgraph photographs were taken in order to define the shock shapes and to determine if any flow anomalies were occurring. The photographs were obtained by using an off axis "Z" Schlieren system (Reference 8), a spark light source and 70mm film. During selected runs for the smaller nose radius models, close-up flow shadowgraphs were taken in order to adequately define the shock shape. These photographs were taken using only one half of the schlieren system, i.e., a parallel light beam was projected directly into the camera instead of reflecting it on the second parabolic mirror. Figure 24 presents a sample shadowgraph for each model configuration. Close up shadowgraphs are also included for the .75 inch sphere cone model and the biconic model.

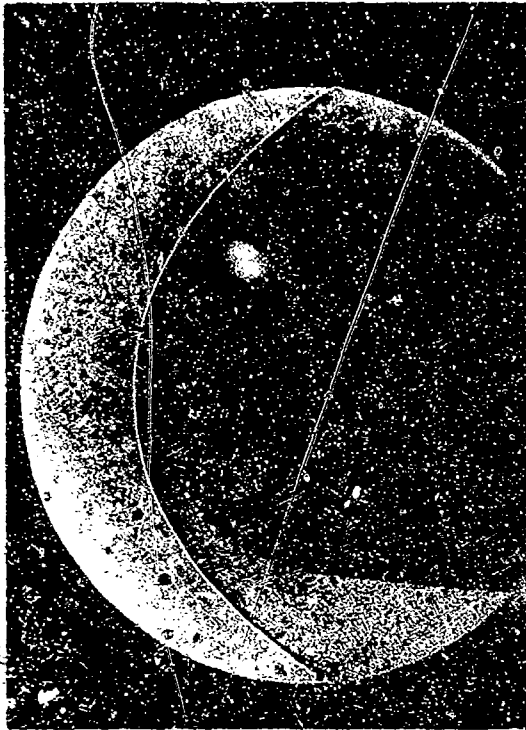


a. Overview, Run 601  
 Sphere Cone  $R_N = 2.5$  Inches

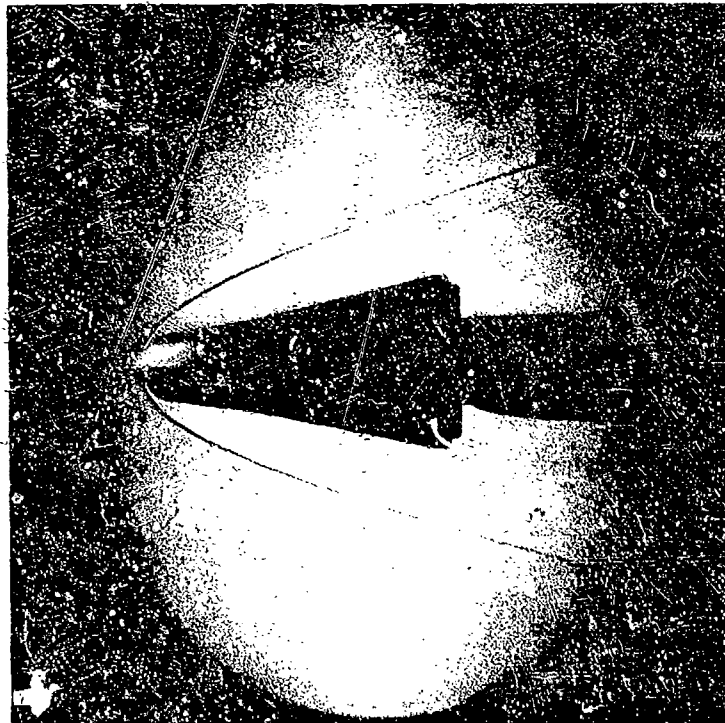


b. Overview, Run 606  
 Sphere Cone  $R_N = 3.5$  Inches

Figure 24. Sample Shadowgraph Photographs



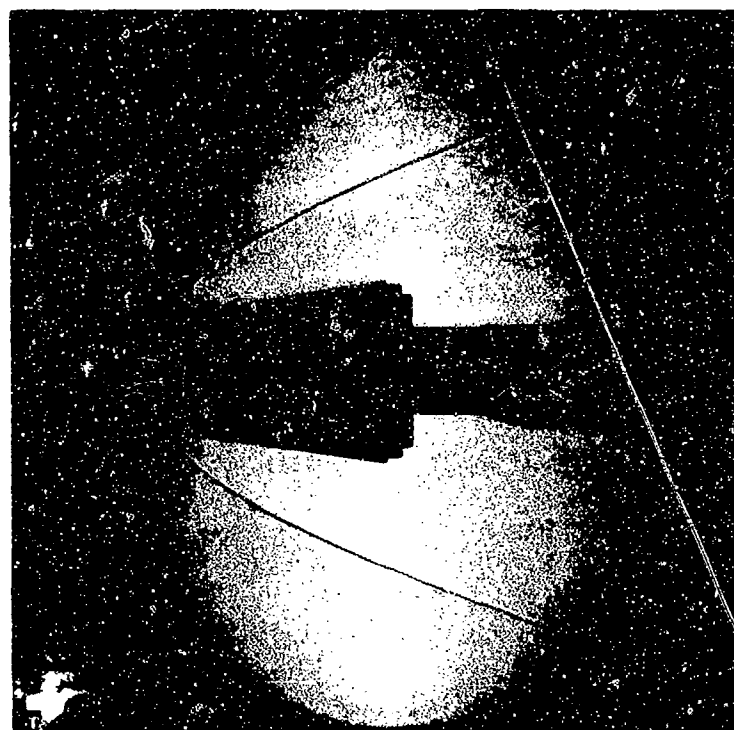
c. Closeup, Run 614  
Sphere Cone  $R_N = .75$  Inch



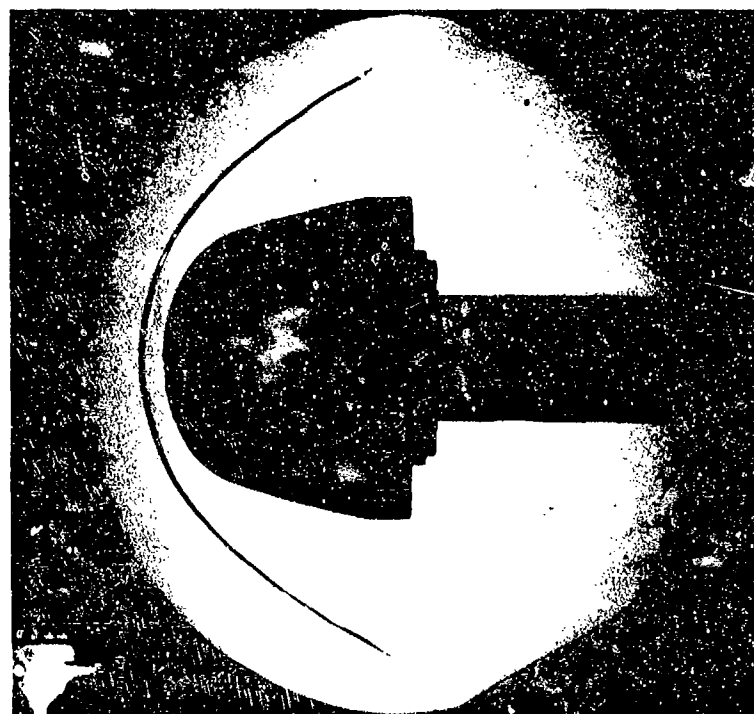
d. Overview, Run 616  
Sphere Cone  $R_N = .75$  Inch

Figure 24. Continued





e. Overview, Run 618  
Sphere Cone  $R_N = 1.5$  Inches

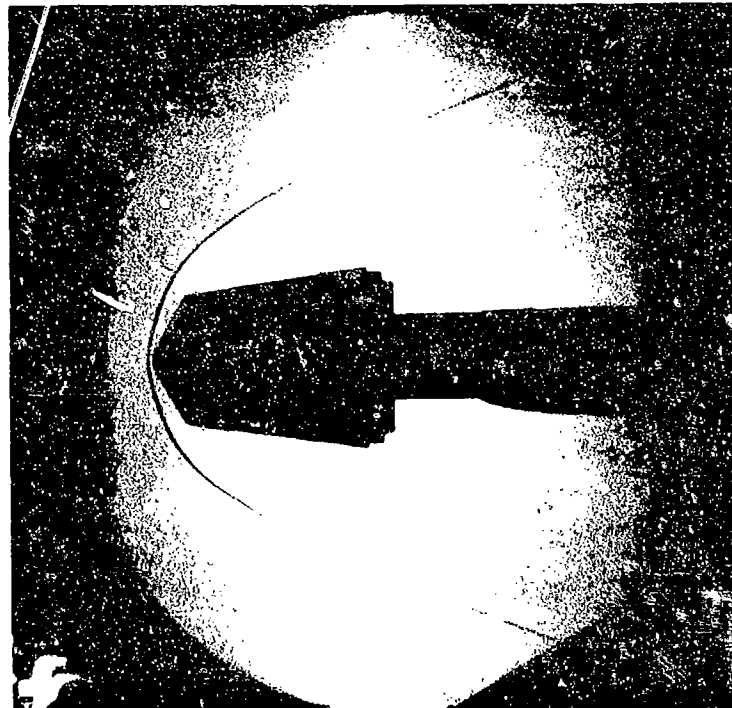


f. Overview, Run 640  
Laminar Shape  $R_S = 3.5$  Inches

Figure 24. Continued



a. Closeup, Run 629  
Ficonic,  $R_G = 1.5$  Inches



b. Overview, Run 621  
Ficonic,  $R_G = 1.5$  Inches

Figure 74. Concluded

## SECTION 6

### TEST RESULTS

The experimental data recorded during the Series J tests provide the basis for satisfying the test objectives. However, the determination of whether or not these objectives have been satisfied can be made only after the experimental data have been reduced and analyzed. The reduced data and comparison of this data to analytical predictions are given in this section. The data reduction technique is reviewed in Section 6.1 and heat transfer coefficient distributions are presented in Section 6.2.

#### 6.1 DATA REDUCTION TECHNIQUE

For continuous thick-skin calorimeter models used in this test series the temperature rise rate across the thickness of the shell is constant after approximately 0.2 second. After this initial response time and assuming negligible circumferential heat conduction and negligible heat losses from the interior surface of the calorimeter shell, the local incident heat flux including streamwise heat conduction can be expressed as

$$q_w = \rho c t \frac{\partial T}{\partial \theta} - \frac{1}{r} \frac{\partial}{\partial s} (K t r \frac{\partial T}{\partial s}) \quad (1)$$

where

- $q_w$  - incident heat flux
- $\rho$  - calorimeter density
- $c$  - calorimeter specific heat
- $t$  - wall thickness
- $T$  - thermocouple temperature
- $\theta$  - time
- $s$  - streamwise distance
- $K$  - calorimeter thermal conductivity
- $r$  - radial distance from model centerline to thermocouple location

The validity of the above assumptions have been examined in detail and were found to be adequate for continuous thick skin calorimeters; see Appendix B of Reference 3. As a point of interest for this test series, the magnitude of the streamwise heat conduction term,  $(1/r)\partial/\partial s[Ktr(\partial T/\partial s)]$ , is less than 10 percent of the total incident heat flux for all models except the .75 inch sphere cone model. This is true only near the beginning of a particular test, since the contribution of the streamwise heat conduction term increases with time. The importance of including the streamwise heat conduction term is not in the magnitude of heat flux at given location, but more in the trend of the data particularly near the transition location where slight differences can influence the interpretation of the transition location.

As can be seen from Equation (1), the spatial temperature distribution must be known as well as the slope of the temperature history. This information can be obtained from the thermocouple temperature data. It is necessary, however, in terms of both data handling and accuracy to first curve fit the thermocouple temperature data. This was accomplished using the splined quadratic least squares curve fit technique described in Appendix A of Reference 3. Each quadratic was least squares fit to six data points with the number of splined quadratic curves depending upon the test duration. Typically, the lower Reynolds number ( $Re^* < 4$ ) runs had from 10 to 13 quadratic segments. Data points prior to 0.2 second initial response time were not included.

In the actual application of Equation (1), the spatial terms were written in standard difference form. The thermocouple locations were taken as nodal points, which worked out quite well since the spacing between individual thermocouples was close enough to yield a good resolution of the temperature field at the time of interest. For purposes of this data report the slope of the temperature histories and the surface temperatures were evaluated at  $\theta = 1$  second for all models except the .75-inch sphere cone model, which were evaluated at  $\theta = .5$  second.

Two techniques were used to determine the temperature distribution for use in determining the streamwise conduction term in Equation (1). For the larger models, i.e., 3.5-inch sphere cone, 2.5-inch sphere cone and the laminar ablated shape calorimeters, the circumferential temperatures at a given  $s/R_N$  location or nodal point were averaged. For the remaining models, the positioning of the thermocouples required a slightly different approach. A best fit curve was drawn through the temperature data. This was done in order not to weight those temperatures on the staggered ray (refer to Figure 11, Section 3) more than the other rays.

In addition to the curve fitted temperature data, the thermal properties of the calorimeter models are required. As indicated in Section 3, the 2.5-inch calorimeter was fabricated from electroformed nickel whereas all other models were machined from Nickel 200. The specific heats and thermal conductivities for these two materials are summarized in Figures 25 and 26, respectively. The density for both electroformed Nickel and Nickel 200 was taken as 555 lbm/ft<sup>3</sup> (References 12, 13).

Having obtained the incident heat flux, the heat transfer coefficient was determined according to

$$h = \frac{q_w}{T_r - T_w} \quad (2)$$

where

$h$  - convective heat transfer coefficient

$T_r$  - boundary layer edge recovery temperature

$T_w$  - wall temperature of thermocouple of interest

The recovery temperature was calculated using the following equation:

$$\frac{T_r}{T_o} = \frac{T_e}{T_o} \left[ 1 + M_e^2 \frac{\gamma - 1}{2} R_f \right] \quad (3)$$

where the recovery factor ( $R_f$ ) was taken to be .85. The boundary layer edge Mach number,  $M_e$ , was calculated for all model configurations using the SAANT code (Reference 14). The resulting ratios of recovery temperature to model stagnation point temperature,  $T_r/T_o$ , are given in Figure 27 for the sphere cone models, laminar ablated shape model and biconic model, respectively.

## 6.2 TEST DATA

In this report, heat transfer coefficient distributions are presented in terms of the normalized streamwise surface location,  $s/R_n$ , and meridian location. The streamwise surface location was either normalized with respect to the nose radius (sphere cone models) or local stagnation point radius of curvature (laminar shape model). For the biconic model, however,  $s$  was normalized by 1.45 inches. This information as well as the roughness height ( $k$ ), stagnation point pressure ( $P_o$ ) and temperature ( $T_o$ ), sonic point unit Reynolds number ( $RE^*$ ) and stagnation point wall temperature ( $T_w$ ) are summarized on each heat

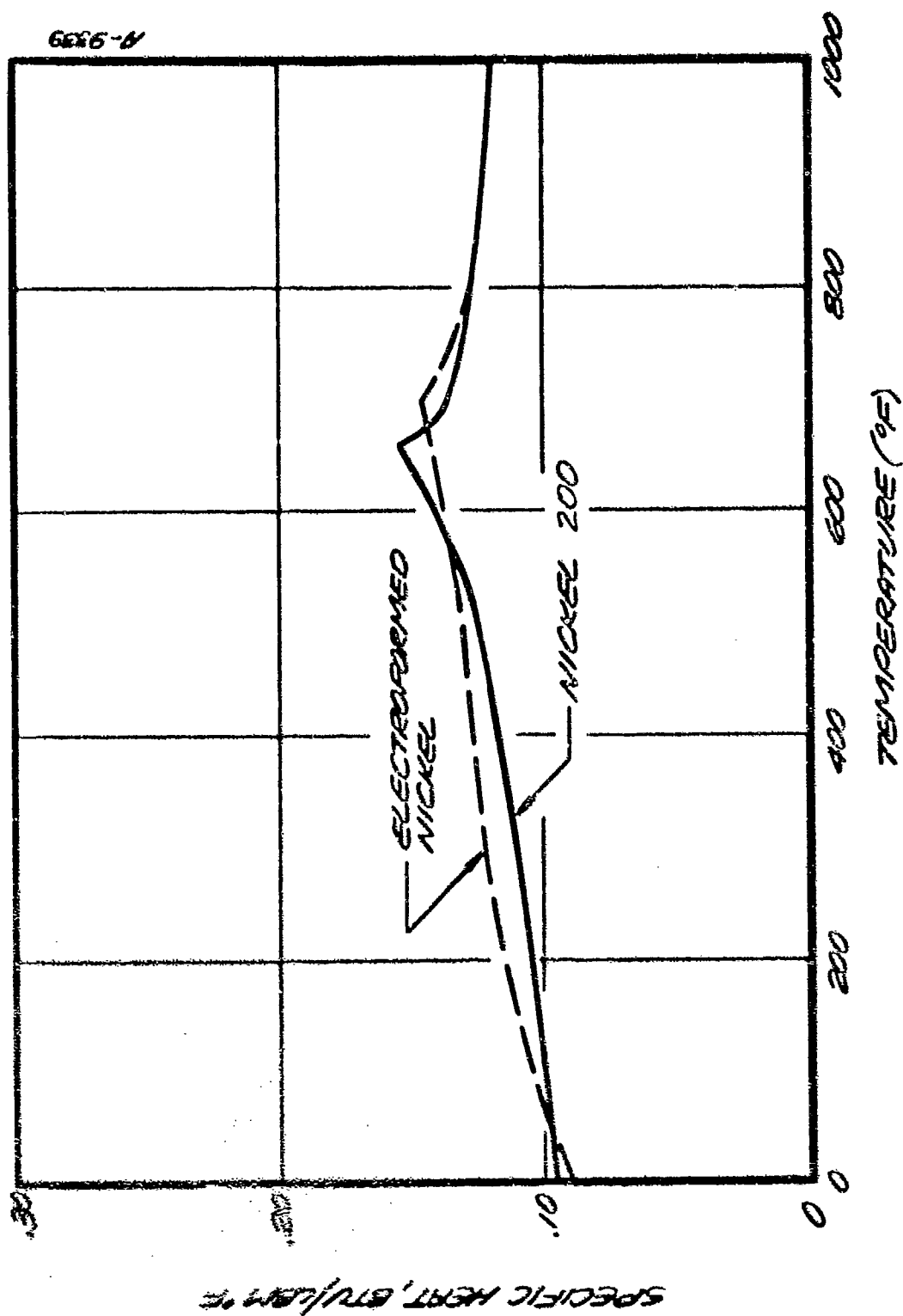


Figure 25. Specific Heat as a Function of Temperature for Electroformed Nickel and Nickel 200

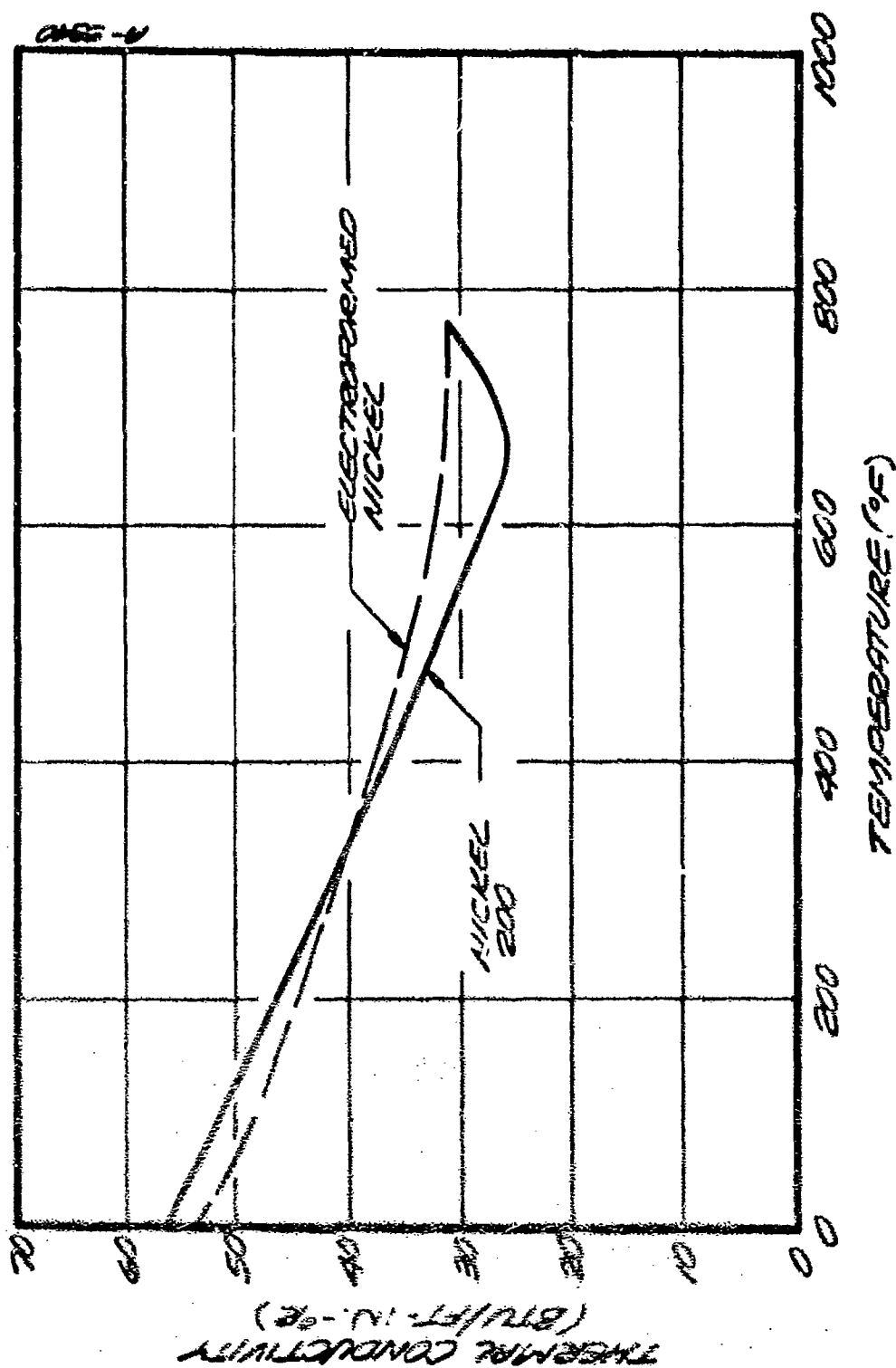


Figure 26. Thermal Conductivity as a Function of Temperature for Electroformed Nickel and Nickel 200

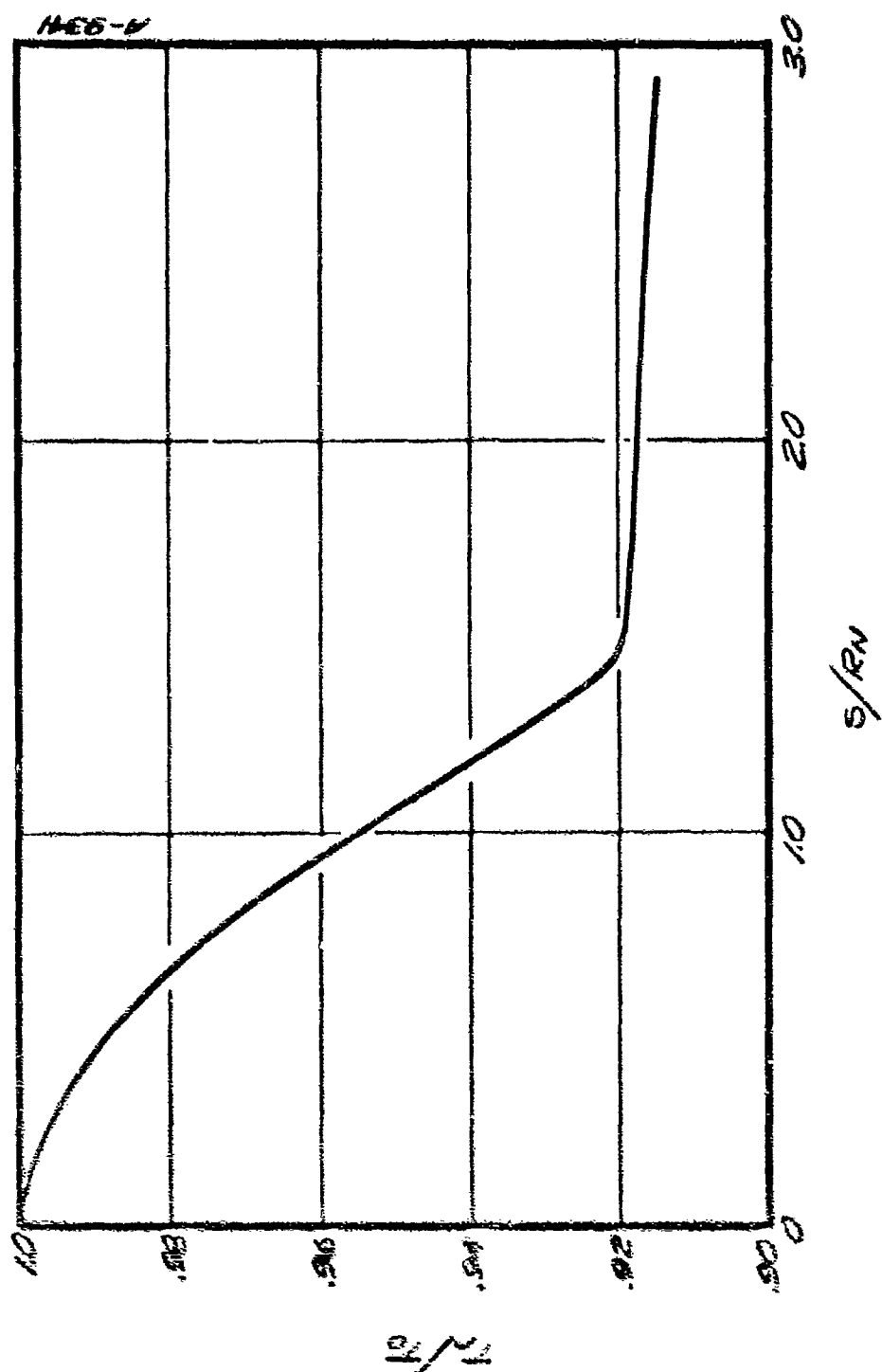


Figure 27. Recovery Temperature Distribution  
 a. Sphere Cone Configuration



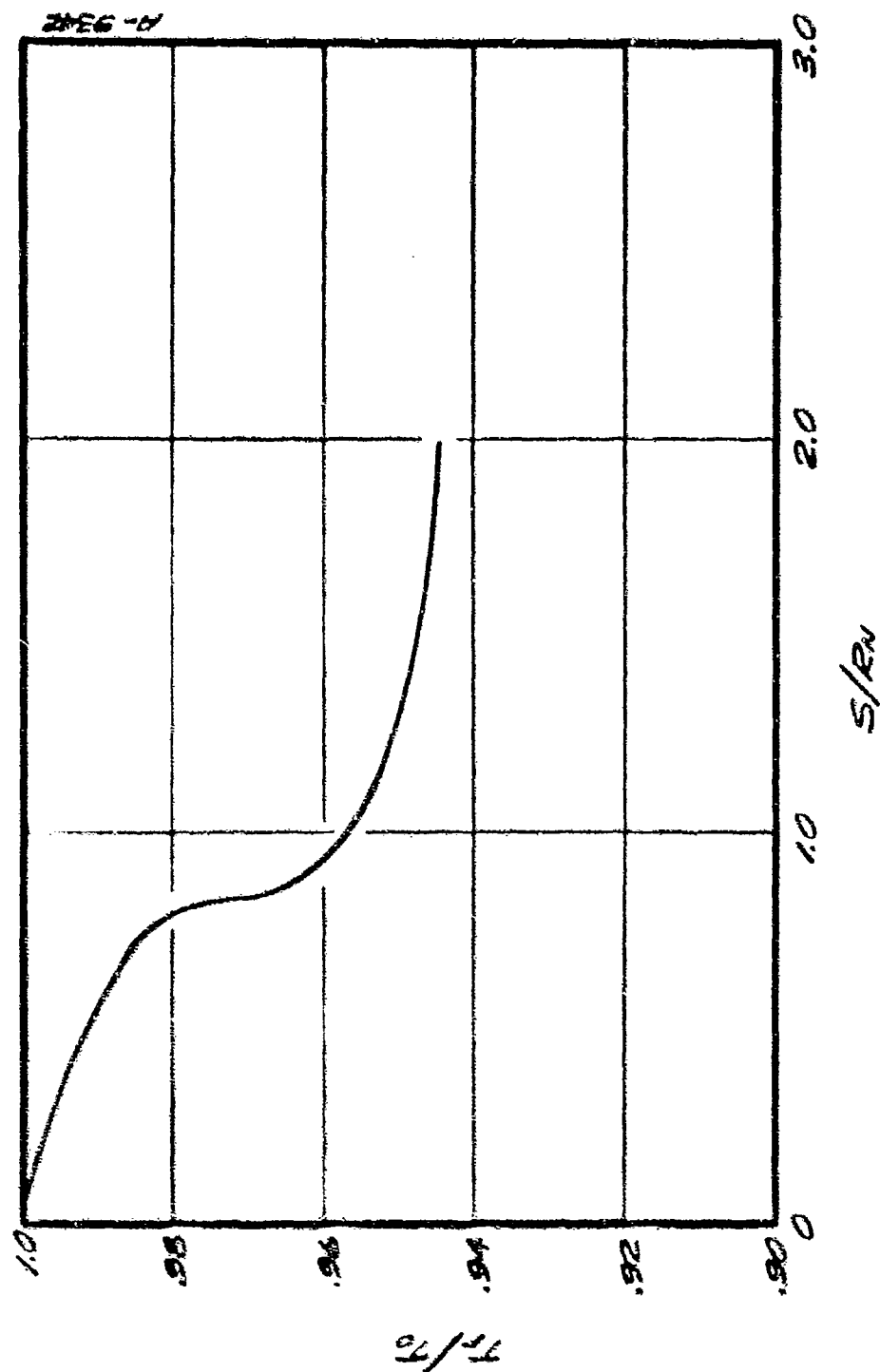


Figure 27. Continued  
b. Laminar Ablated Shape Configuration

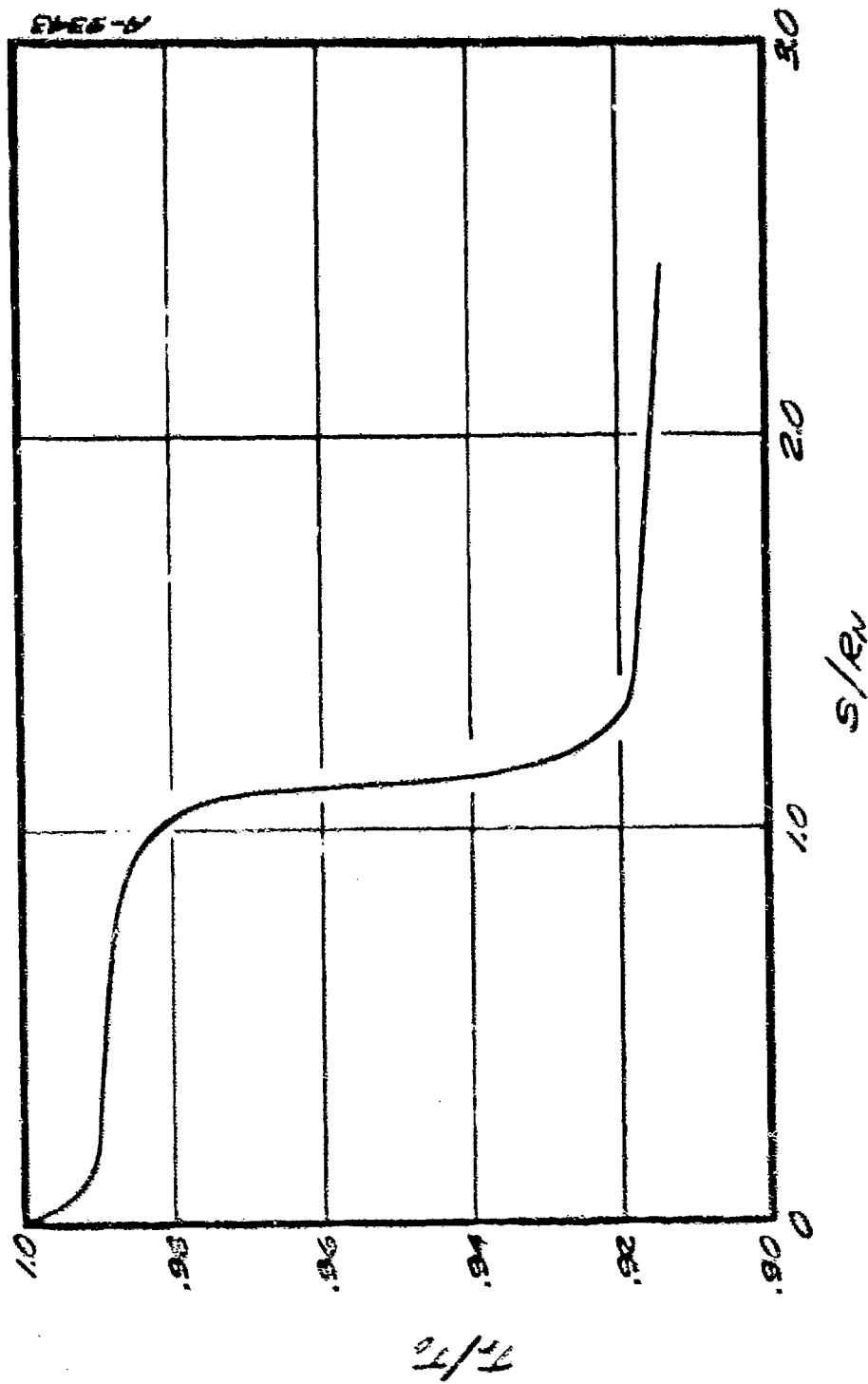


Figure 27. Concluded

c. Biconic Configuration

transfer coefficient plot. In addition to the thermocouple data, laminar and fully turbulent predictions are also included for each run. These predictions were made using the SAANT code.

Heat transfer coefficient distributions are presented as follows:

- Model Number 4 (k = 3.0 mils, 2.5-inch sphere cone) Figure 28
- Model Number 18 (k = 3.5 mils, 3.5-inch sphere cone) Figure 29
- Model Number 16 (k = 3.5 mils, .75-inch sphere cone) Figure 30
- Model Number 17 (k = 3.5 mils, 1.5-inch sphere cone) Figure 31
- Model Number 20 (k = 3.5 mils, Biconic) Figure 32
- Model Number 19 (k = 3.5 mils, Laminar Ablated Shape) Figure 33

Throughout these figures, abnormal data have been deleted. The criterion for establishing a bad data point was to look at both the raw and fitted temperature data identifying those data exhibiting extreme noise, no or little response, etc. A discussion of the results presented in the above figures is given in the following section.

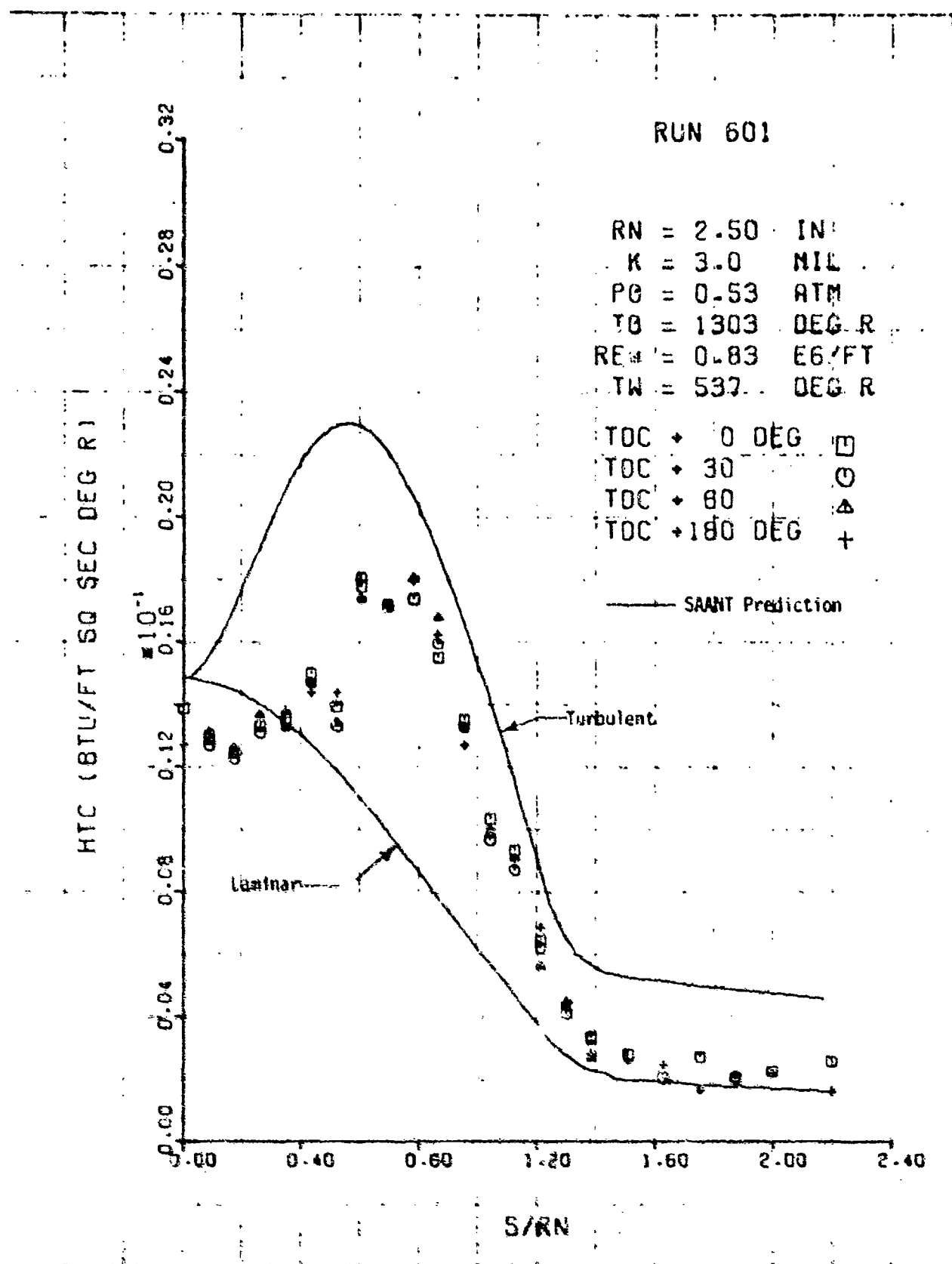


Figure 25. Convective Heat Transfer Coefficient Distribution,  
 Model 4, Sphere Cone,  $R_N = 2.5$  Inches  
 a. Run No. 601 ( $Re_N = 1.94 \times 10^5/\text{ft}$ )

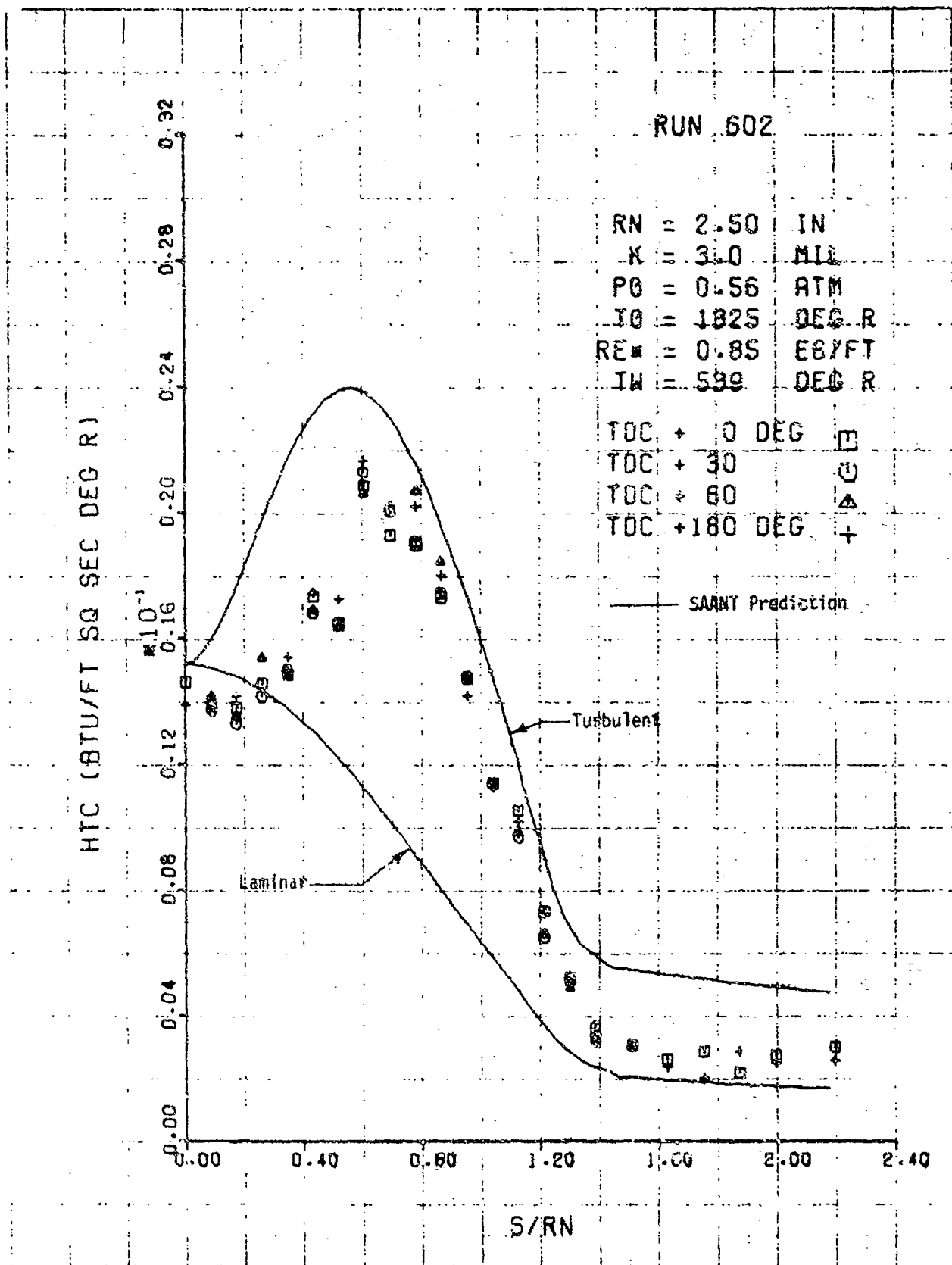


Figure 28. Continued

b. Run No. 602 ( $Re_{\infty} = 2.00 \times 10^6/\text{ft}$ )

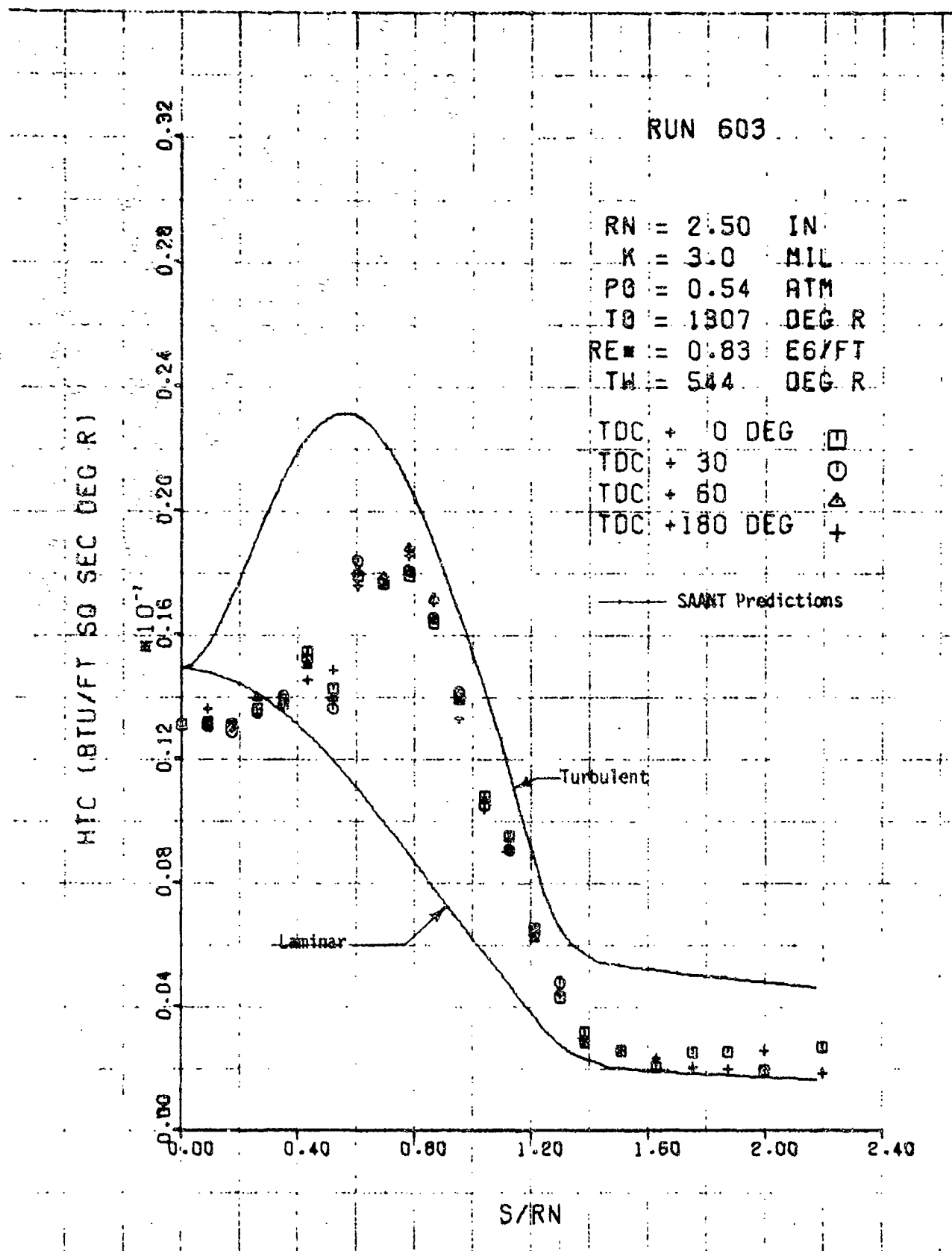


Figure 28. Continued

c. Run No. 603 ( $Re_{\infty} = 1.96 \times 10^6/\text{ft}$ )

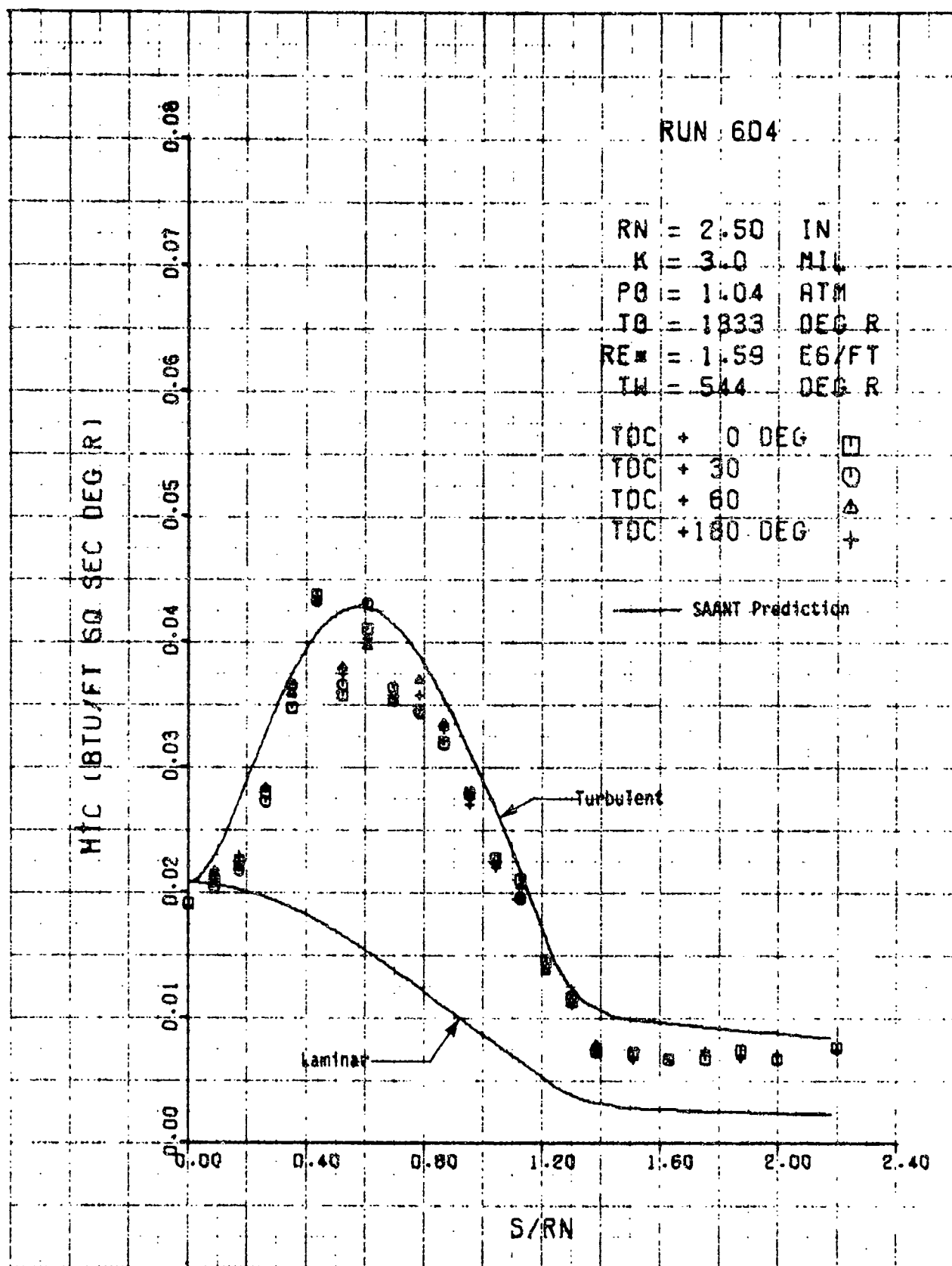


Figure 28. Concluded

d. Run 604 ( $Re_{\infty} = 3.67 \times 10^6/\text{ft}$ )

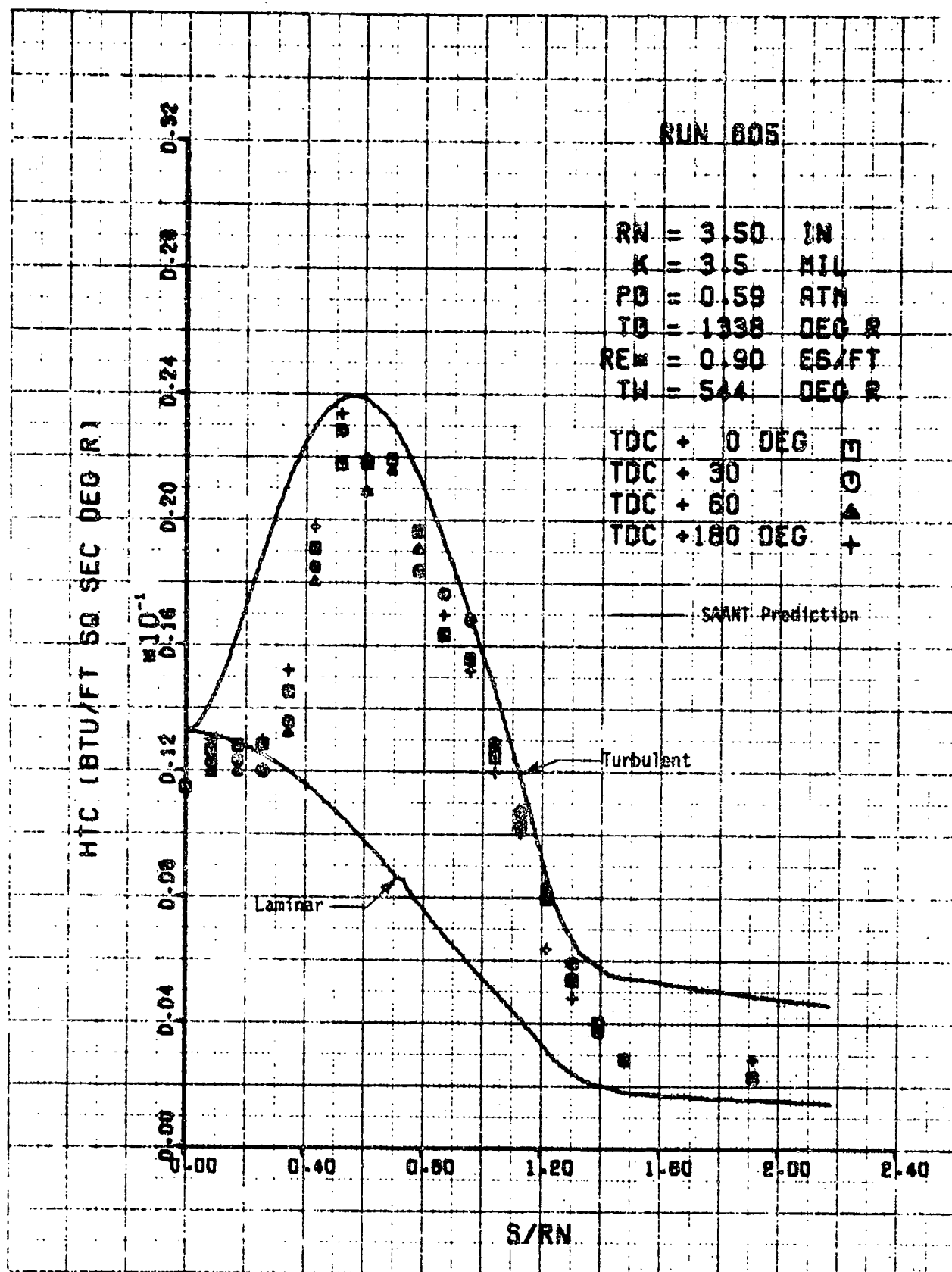


Figure 29. Convective Heat Transfer Coefficient Distribution,  
 Model 18, Sphere Cone,  $R_N = 3.5$  Inches  
 a. Run No. 605 ( $Re_\infty = 2.08 \times 10^6/\text{ft}$ )



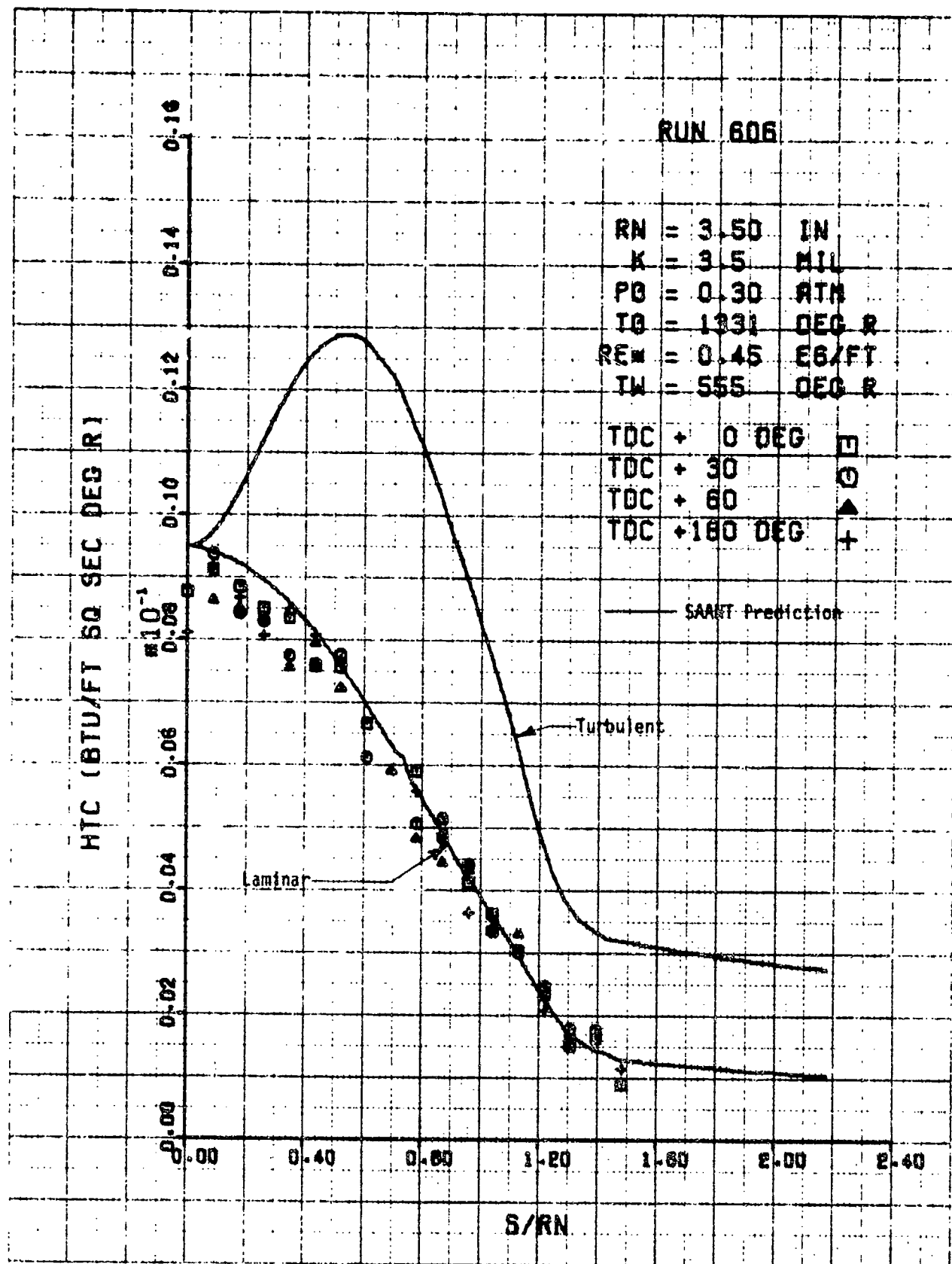


Figure 29. Continued

b. Run No. 606 ( $Re_{\infty} = 1.09 \times 10^6/\text{ft}$ )

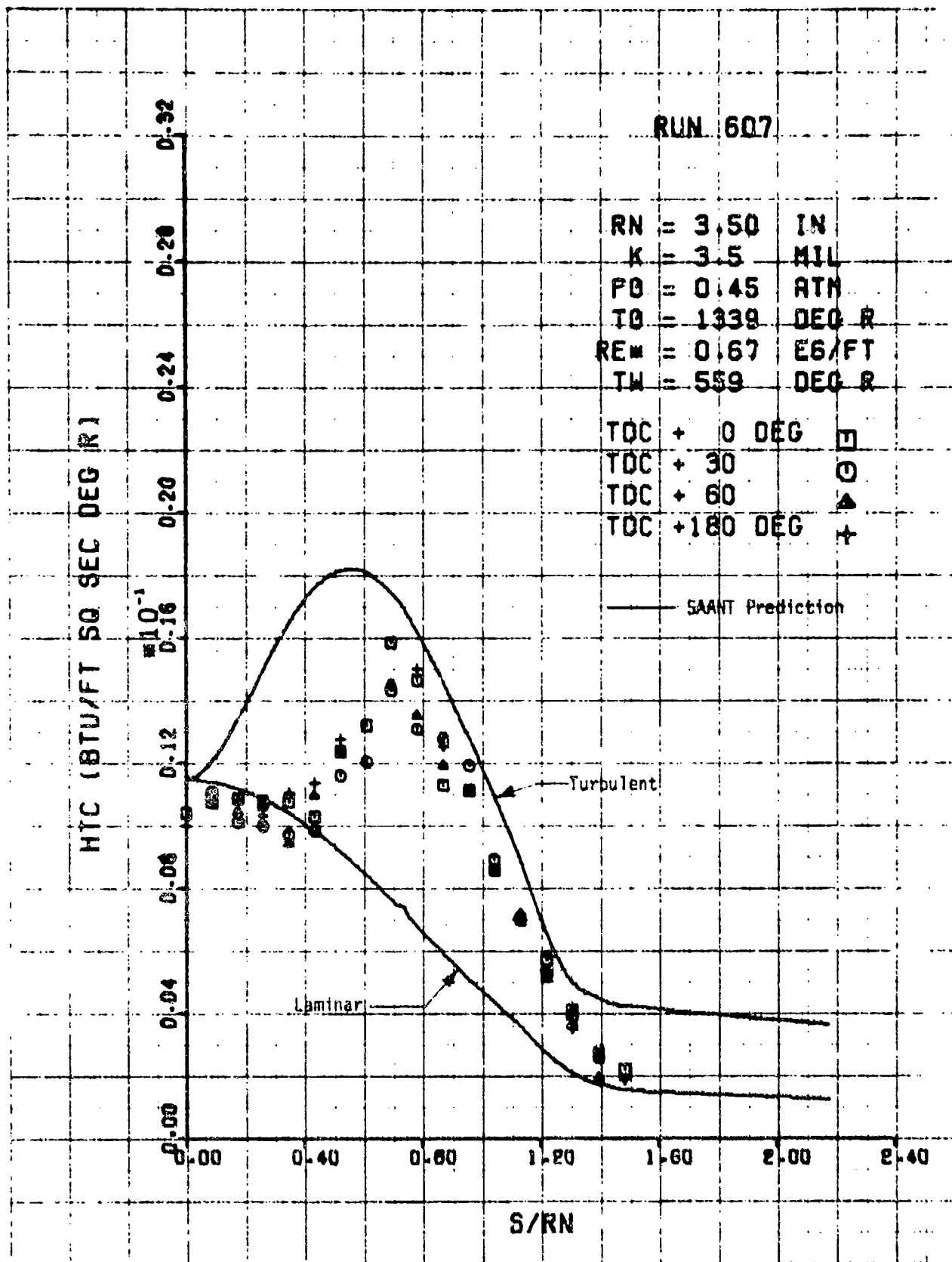


Figure 29. Continued

c. Run No. 607 ( $Re_w = 1.58 \times 10^5/\text{ft}$ )

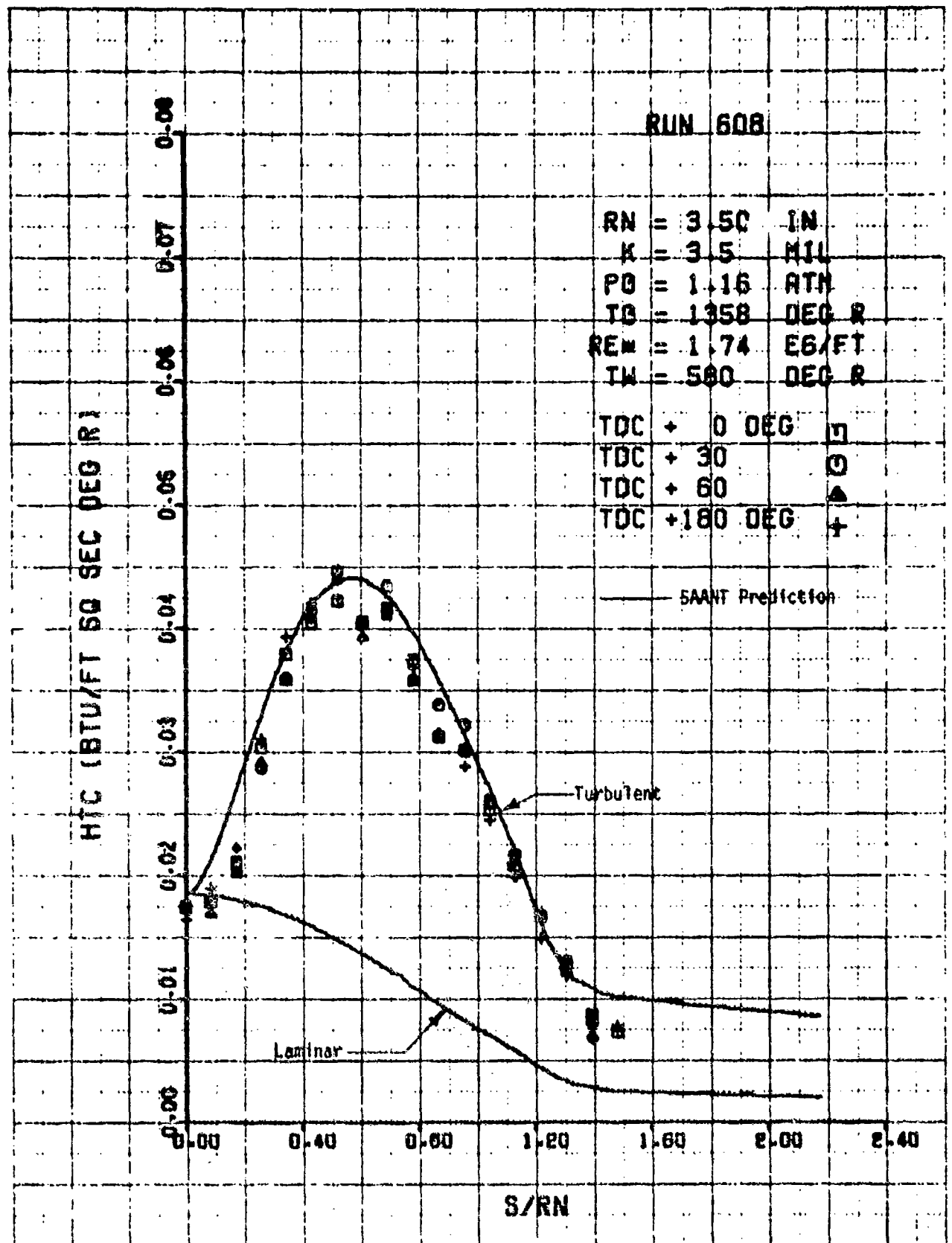


Figure 29. Continued

d. Run No. 608 ( $Re_m = 3.98 \times 10^6/\text{ft}$ )

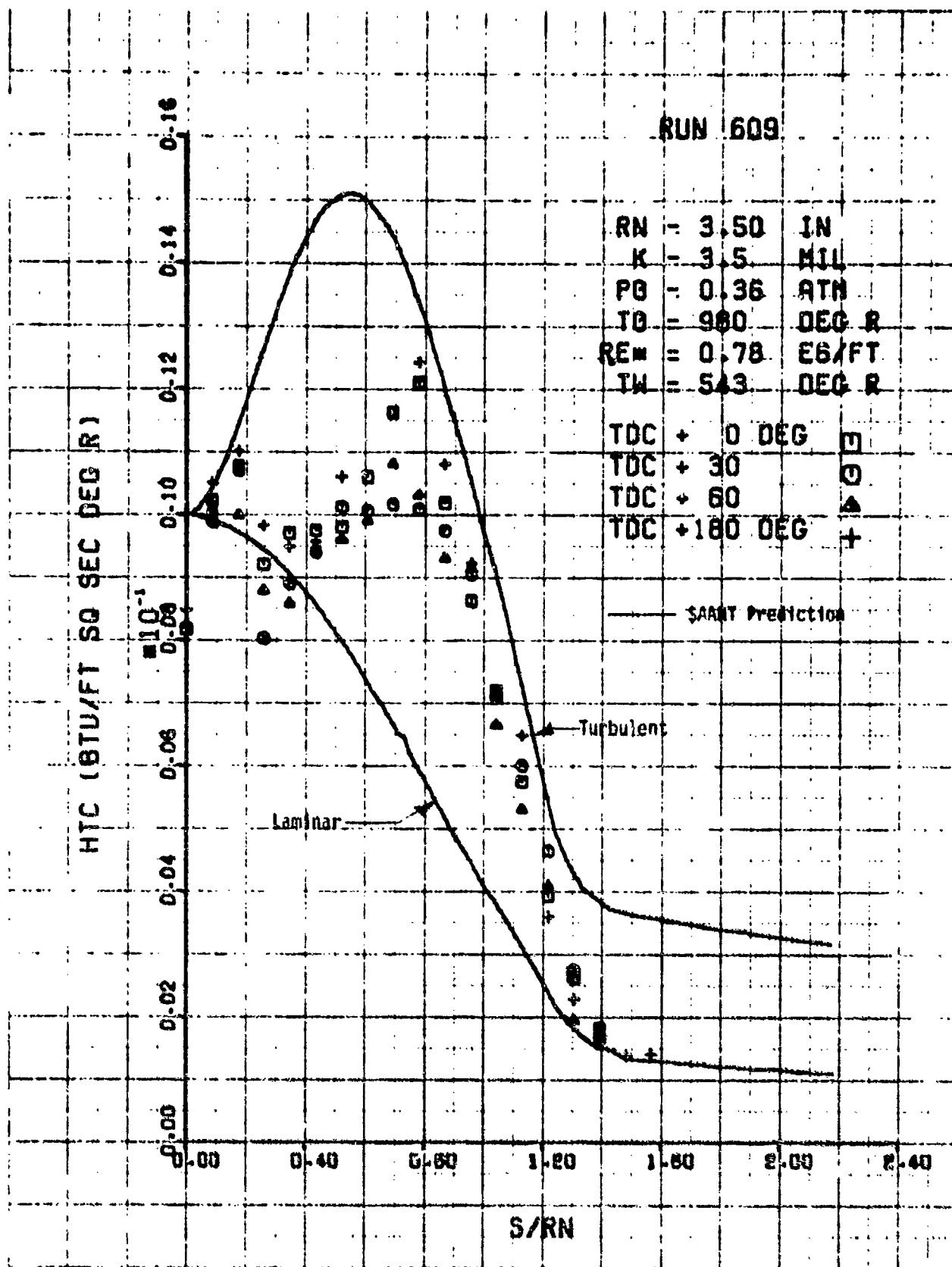


Figure 29. Continued

e. Run No. 609 ( $Re_{\infty} = 2.04 \times 10^6/\text{ft}$ )

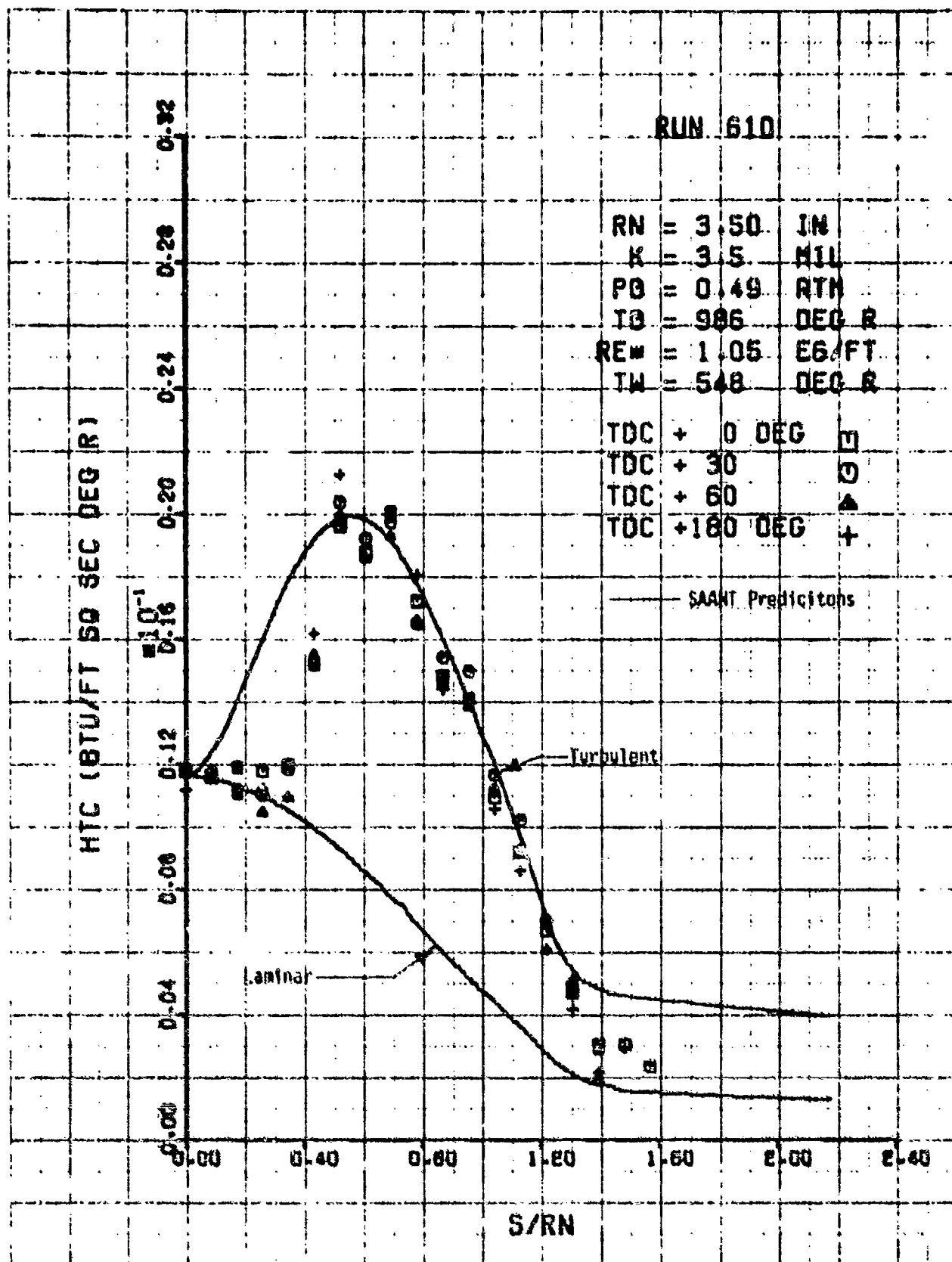


Figure 29. Continued

f. Run No. 610 ( $Re_m = 2.74 \times 10^4/\text{ft}$ )

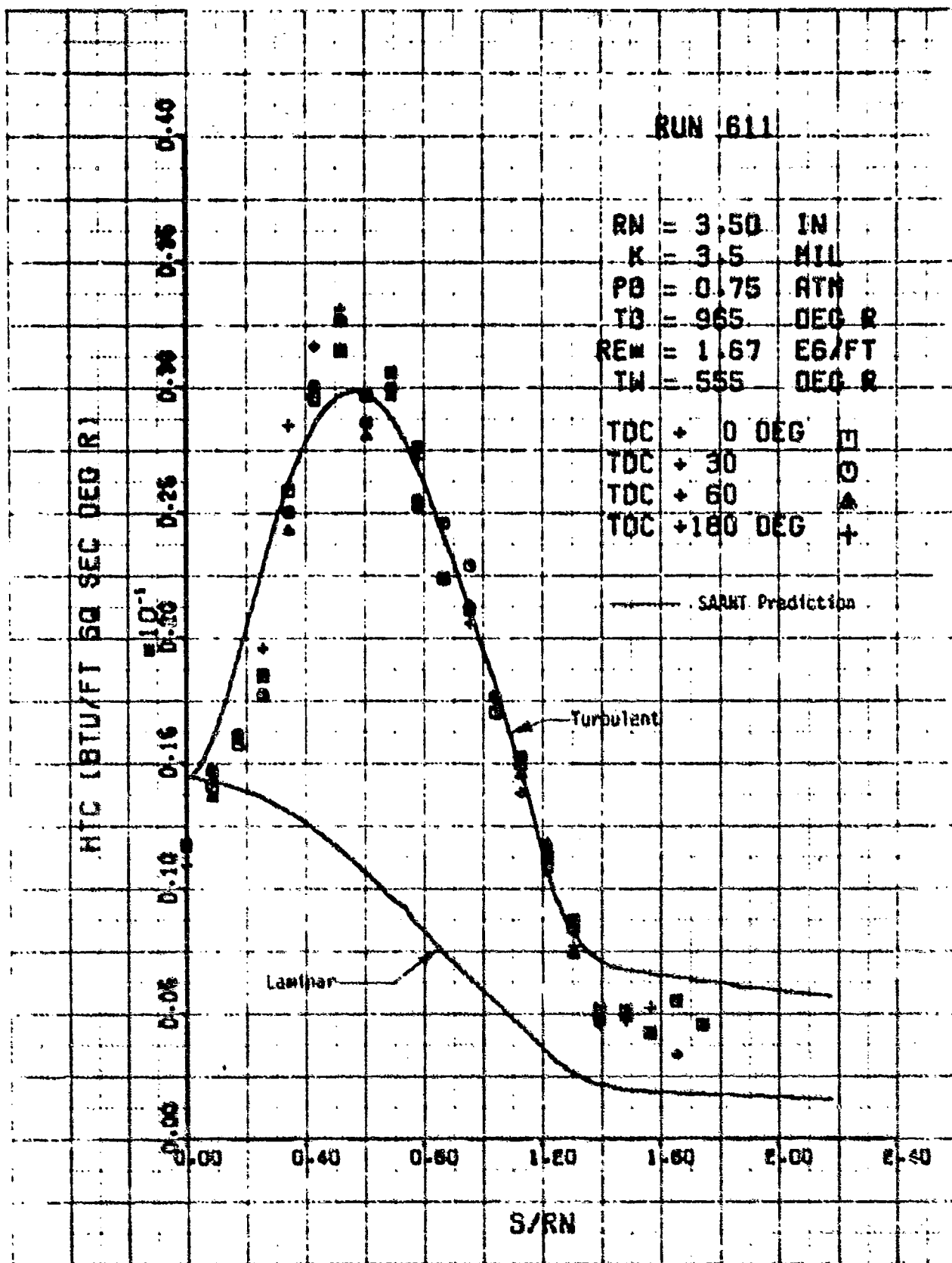


Figure 29. Continued

g. Run No. 611 ( $Re_m = 4.31 \times 10^4/\text{ft}$ )

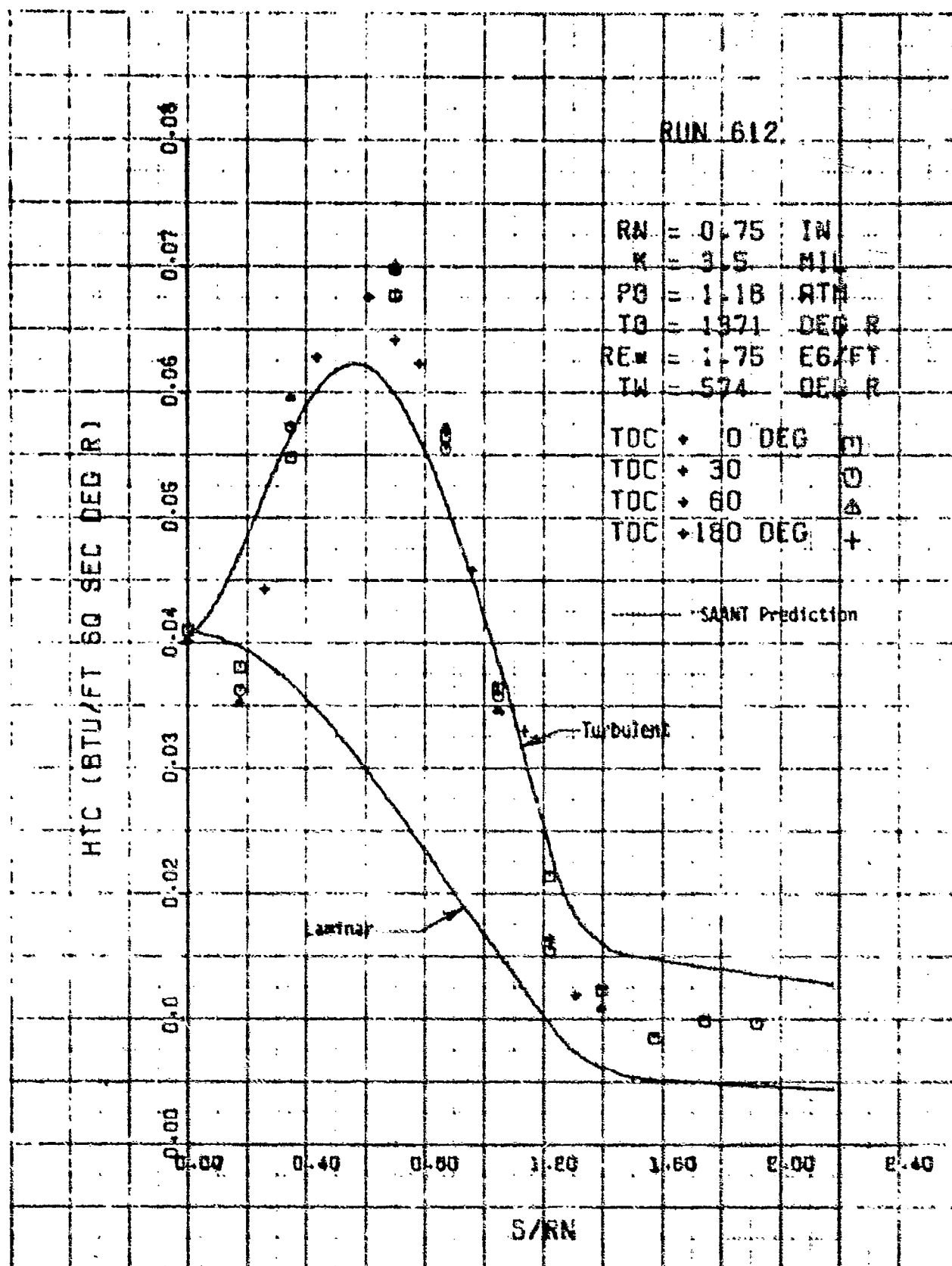


Figure 30. Convective Heat Transfer Coefficient Distribution,  
Model 16, Sphere Cone,  $R_n = .75$  inch

a. Run No. 612 ( $Re_n = 3.98 \times 10^5$ /ft)

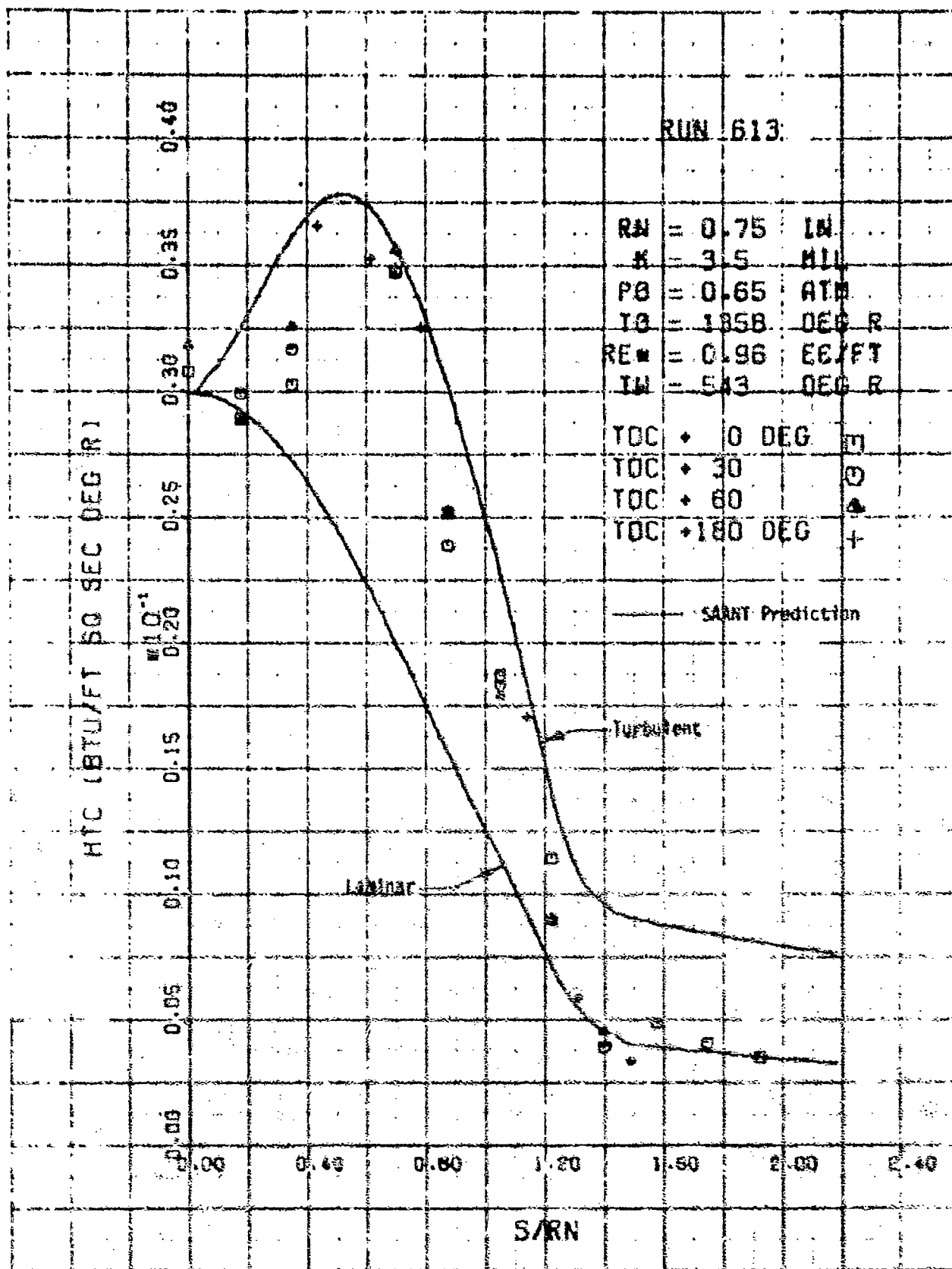


Figure 30. Continued

b. Run No. 613 ( $Re_{\infty} = 2.22 \times 10^5$ )



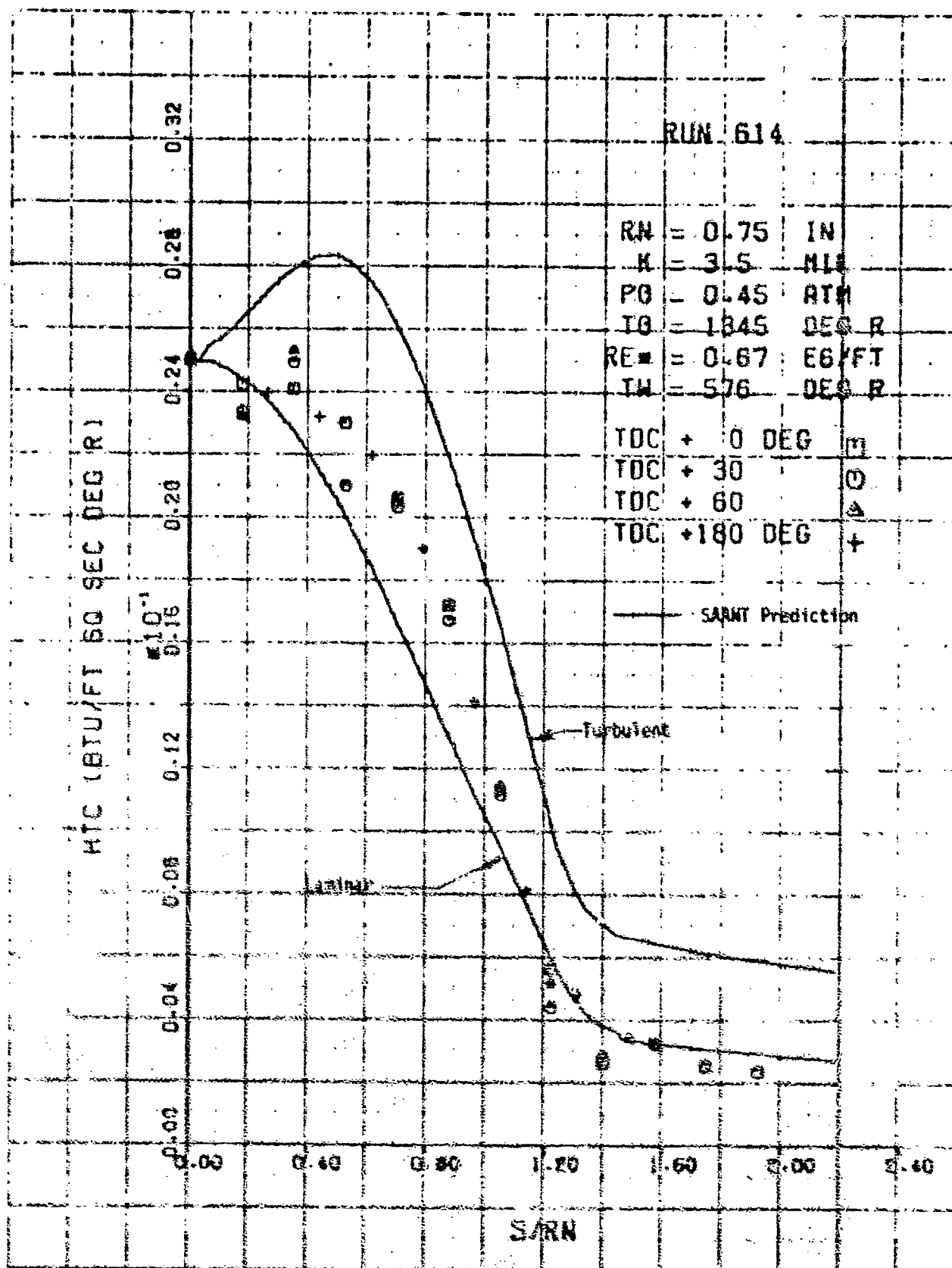


Figure M. Continued

c. Run No. 614 ( $Re = 1.60 \times 10^5/ft$ )

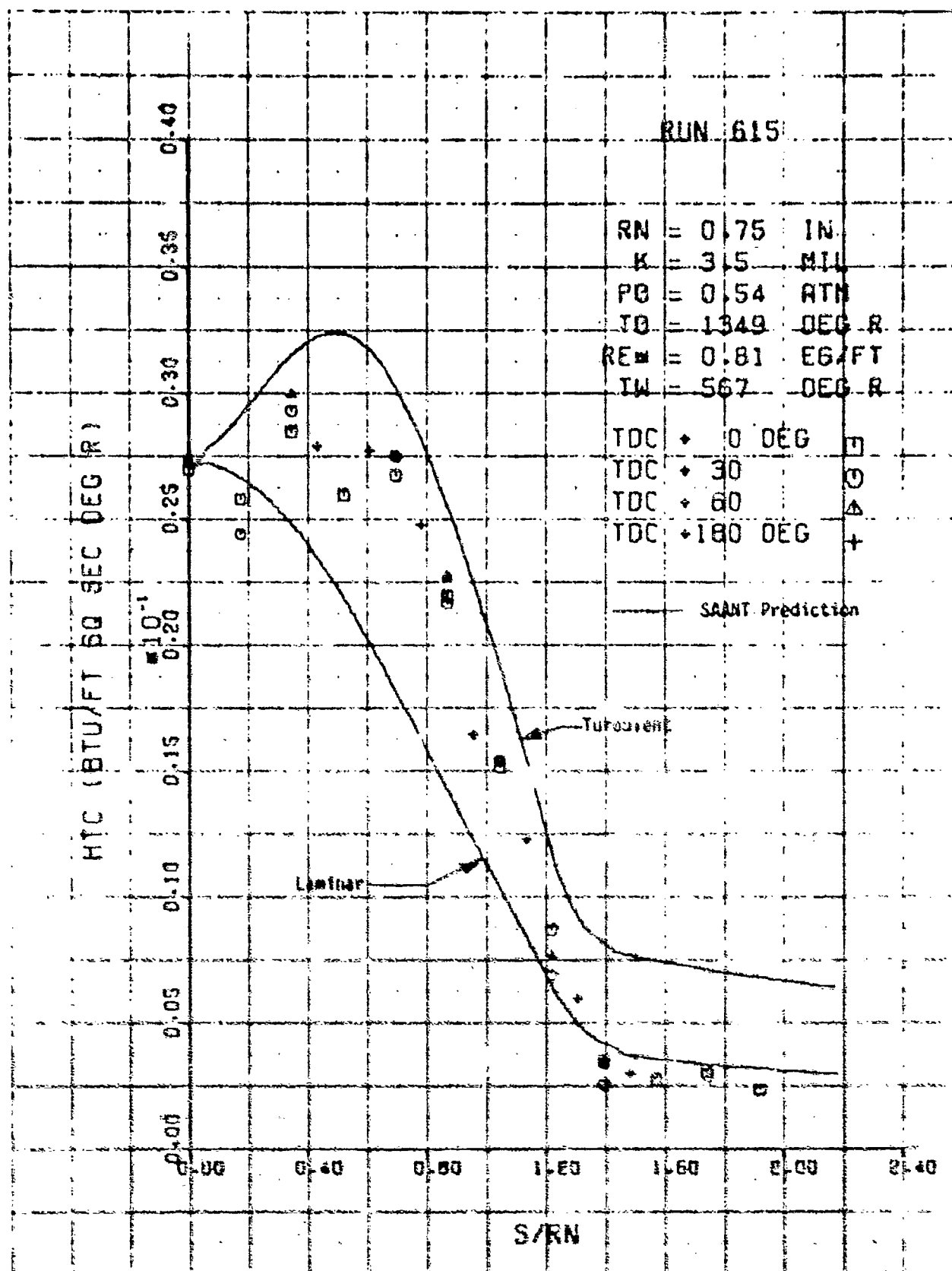


Figure 10. Continued

d. Run No. 615 ( $Re = 1.89 \times 10^5/ft$ )

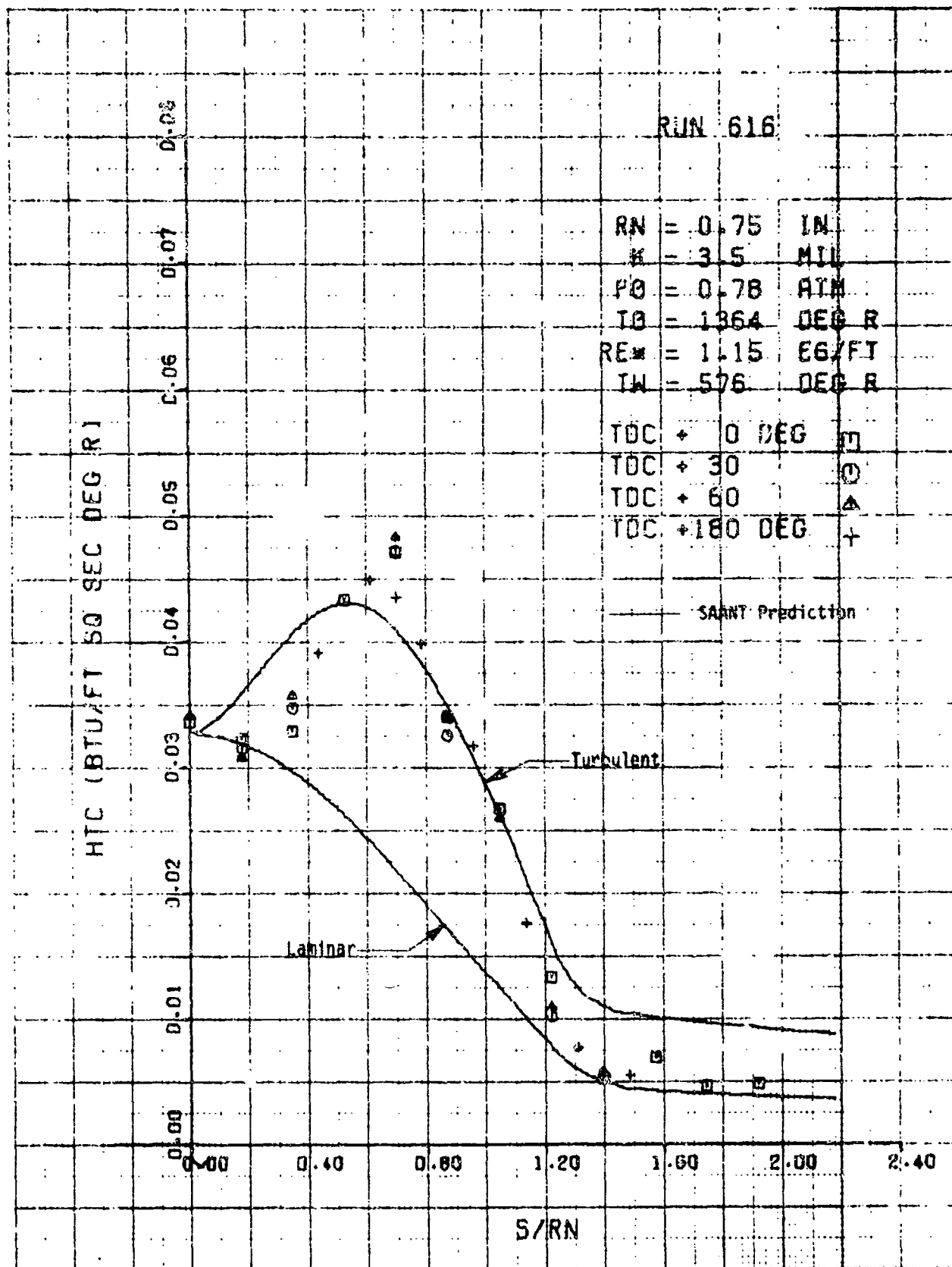


Figure 30. Continued

e. Run No. 616 ( $Re_w = 2.60 \times 10^6/\text{ft}$ )

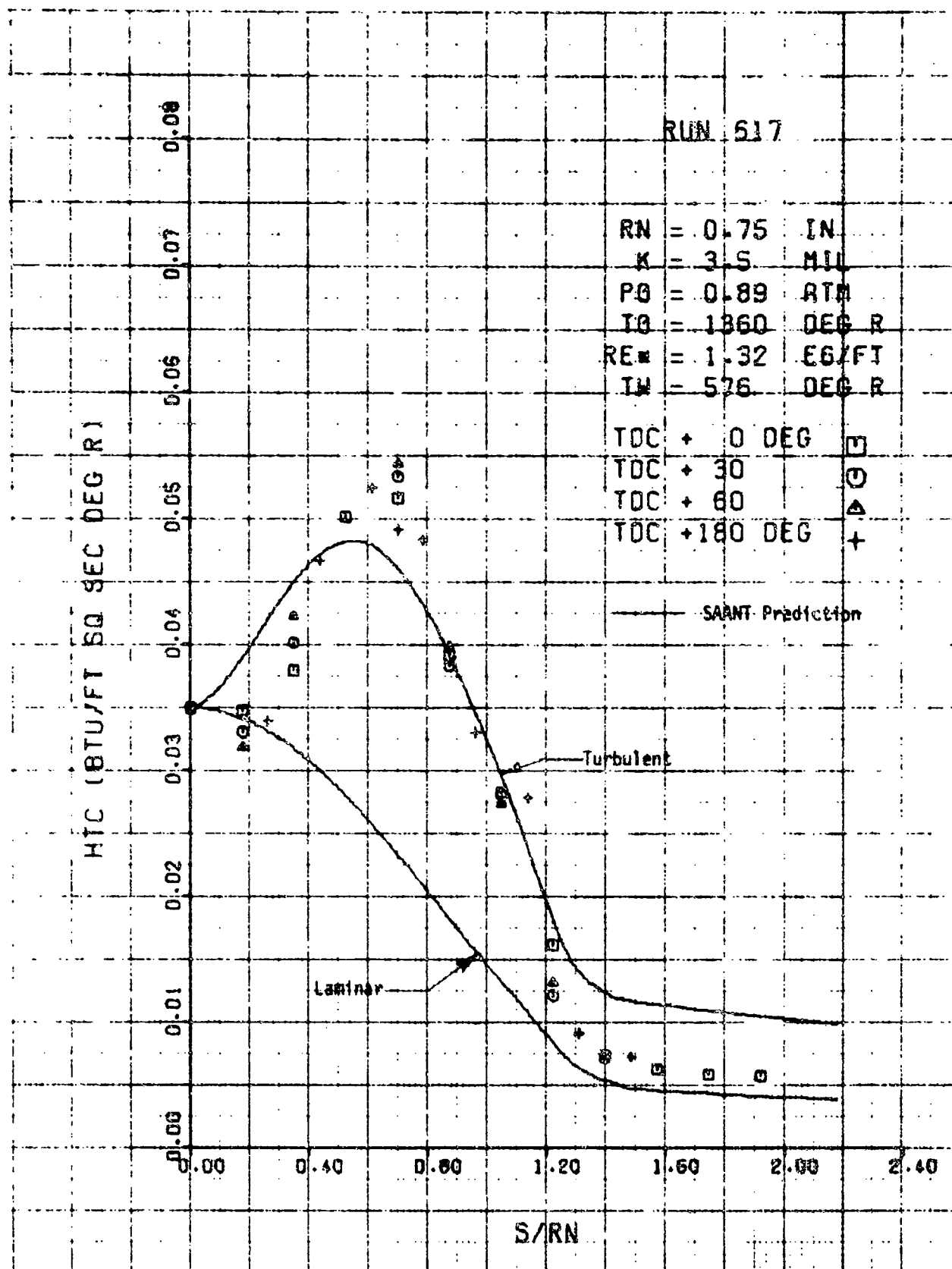


Figure 30. Concluded

f. Run No. 617 ( $Re_{\infty} = 3.04 \times 10^5/\text{ft}$ )

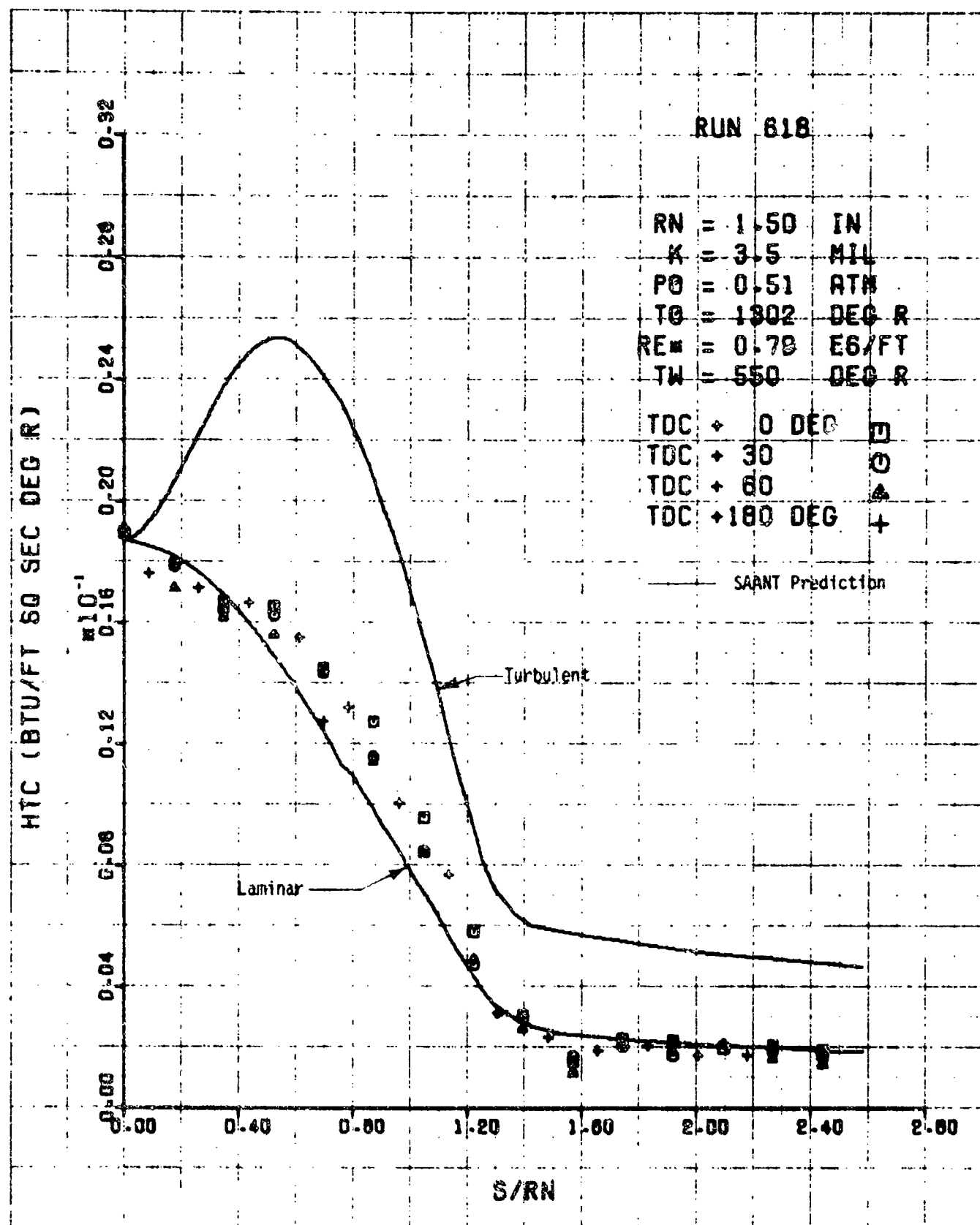


Figure 31. Convective Heat Transfer Coefficient Distribution, Model 17, Sphere Cone,  $R_N = 1.5$  Inches

a. Run No. 618 ( $Re_m = 1.87 \times 10^6/\text{ft}$ )

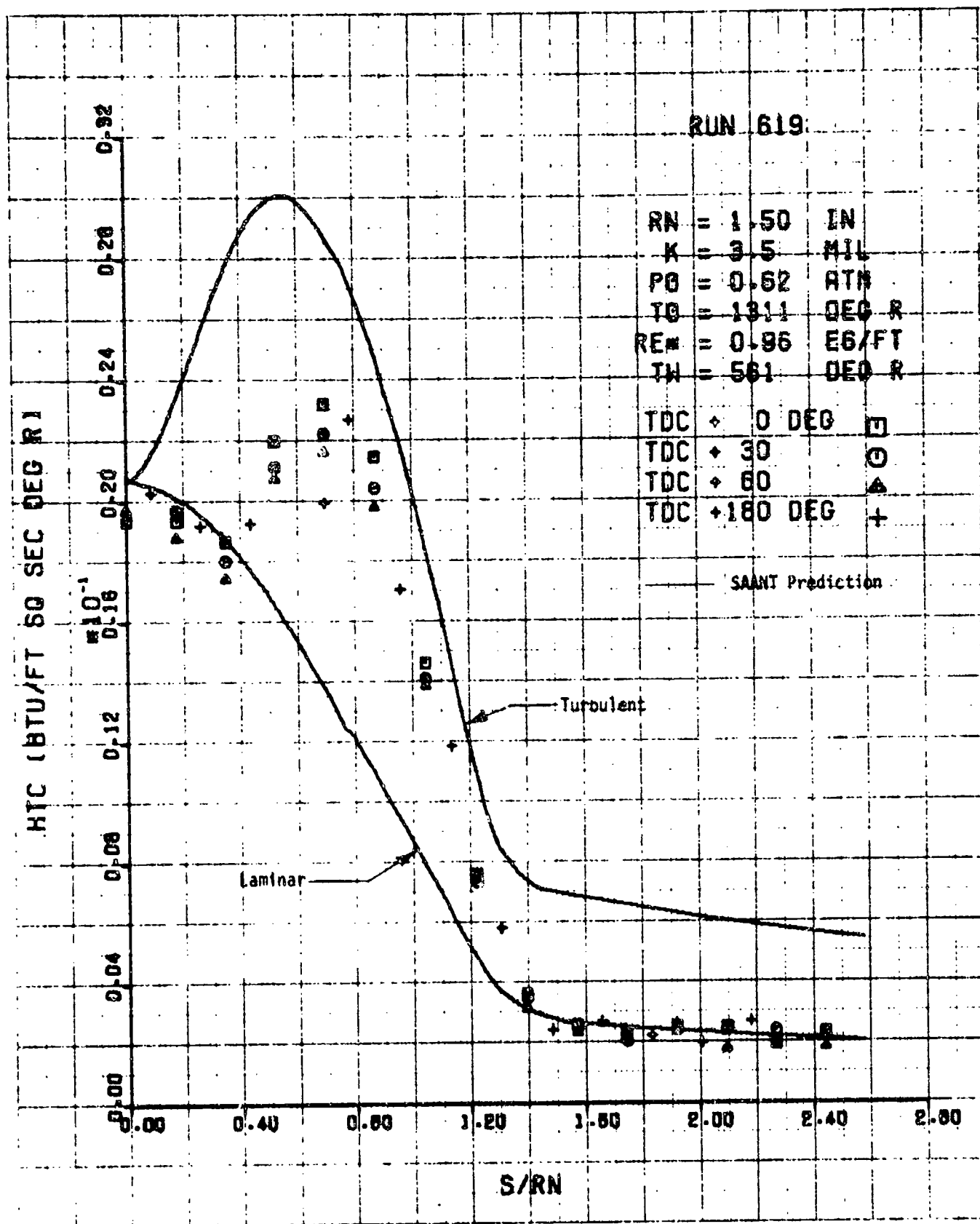


Figure 31. Continued

b. Run No. 619 ( $Re_{\infty} = 2.25 \times 10^6/\text{ft}$ )

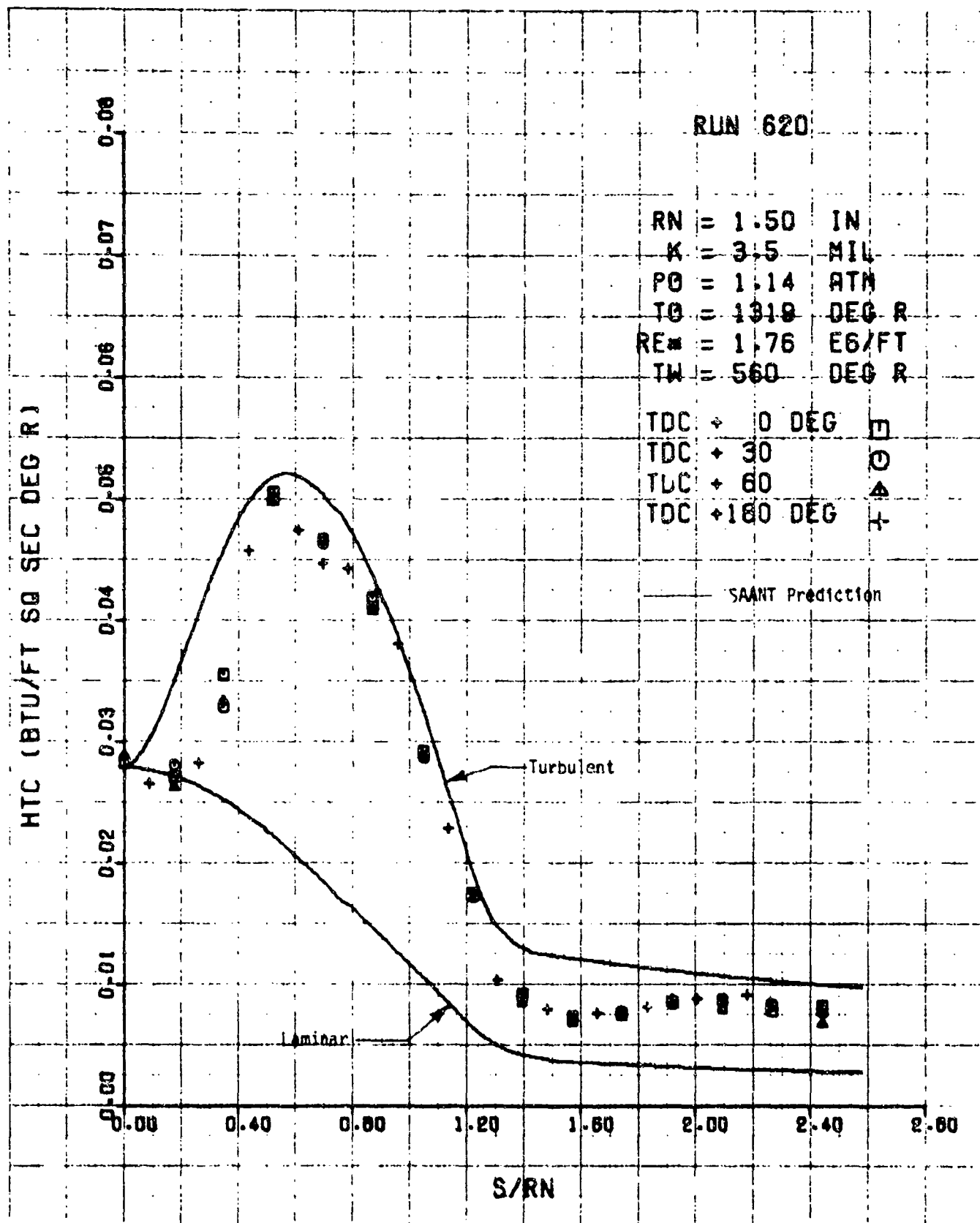


Figure 31. Continued

c. Run No. 620 ( $Re_s = 4.05 \times 10^5/\text{ft}$ )

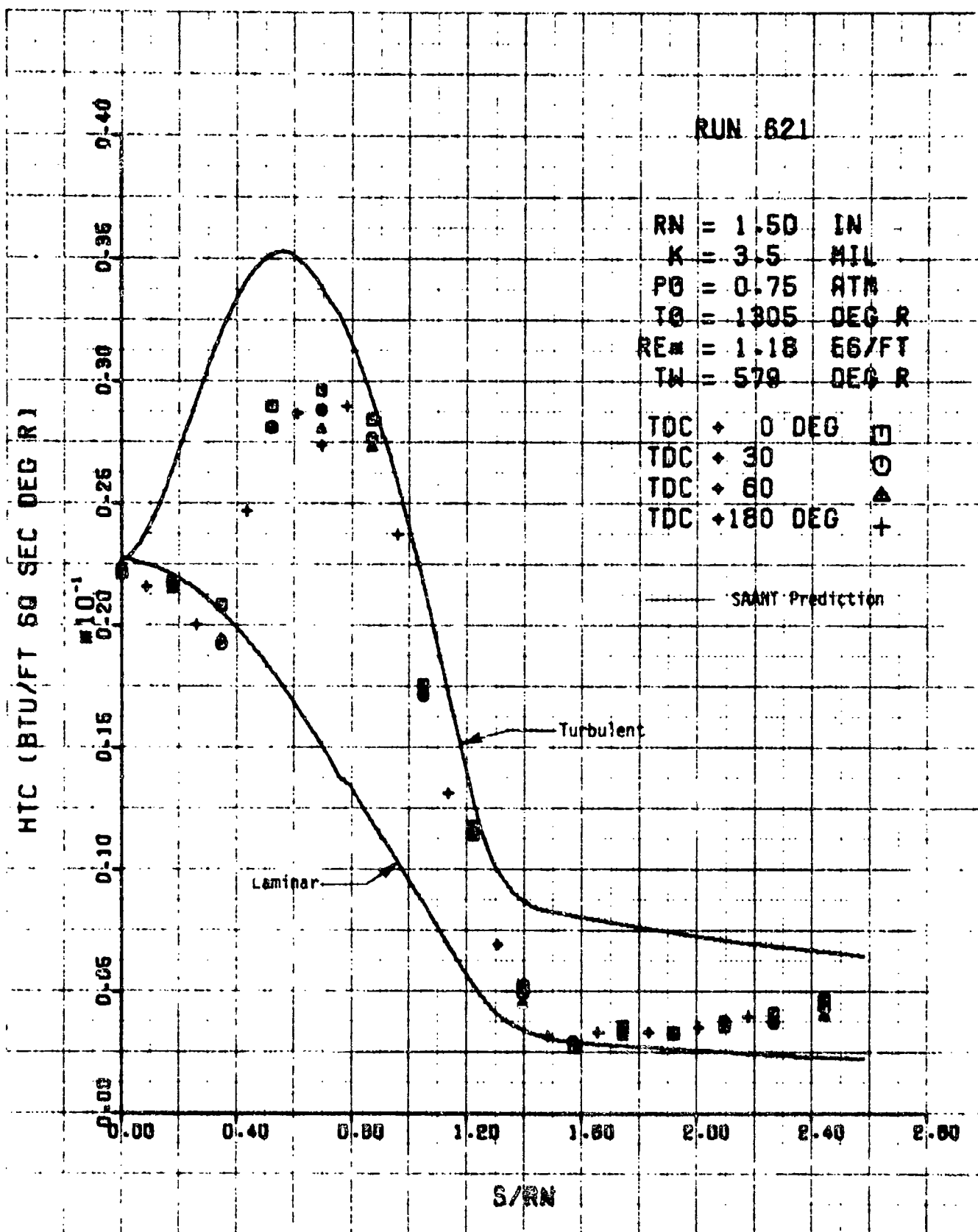


Figure 31. Continued

d. Run No. 621 ( $Re_{\infty} = 2.75 \times 10^6/\text{ft}$ )



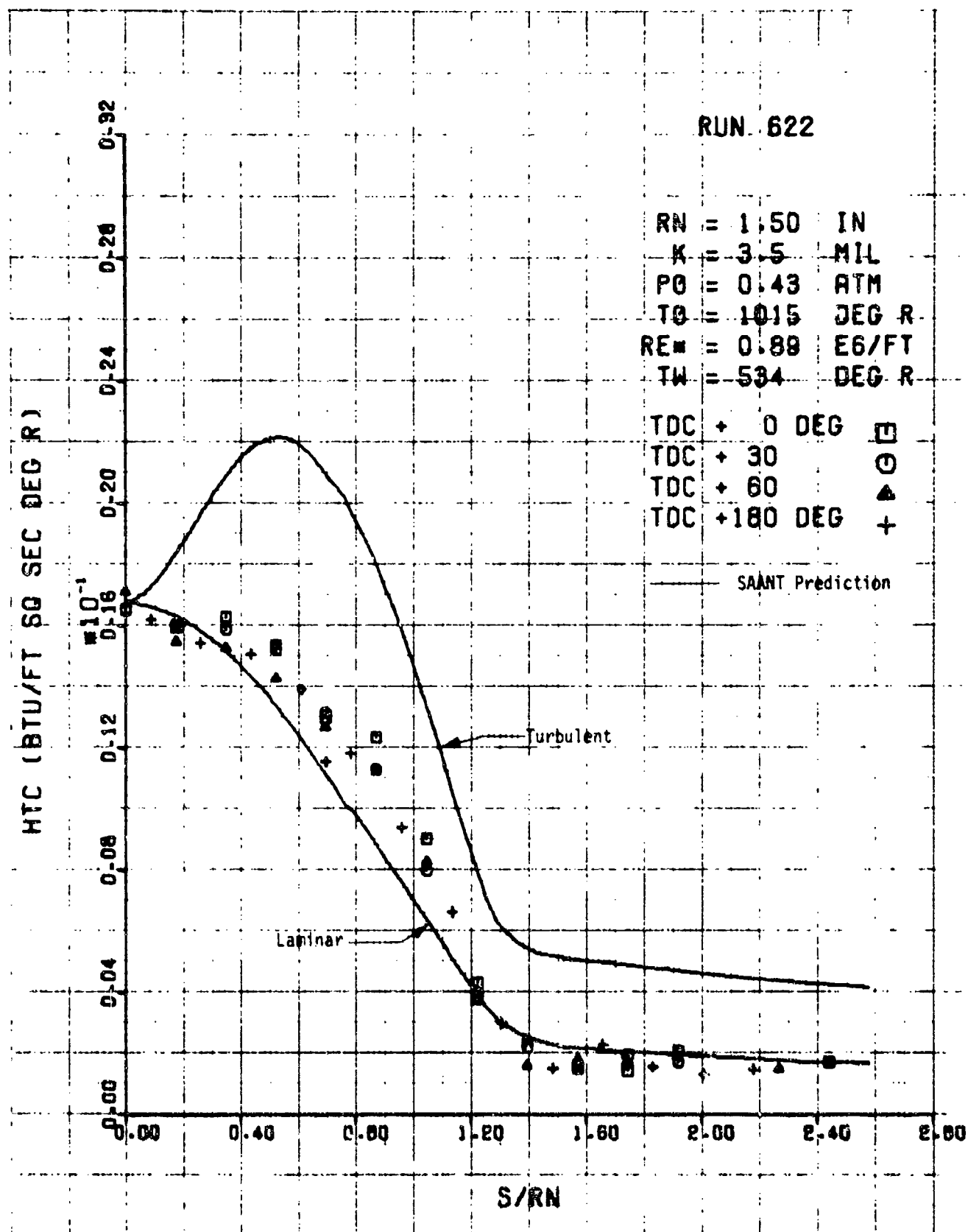


Figure 31. Continued

e. Run No. 622 ( $Re_s = 2.31 \times 10^6/\text{ft}$ )

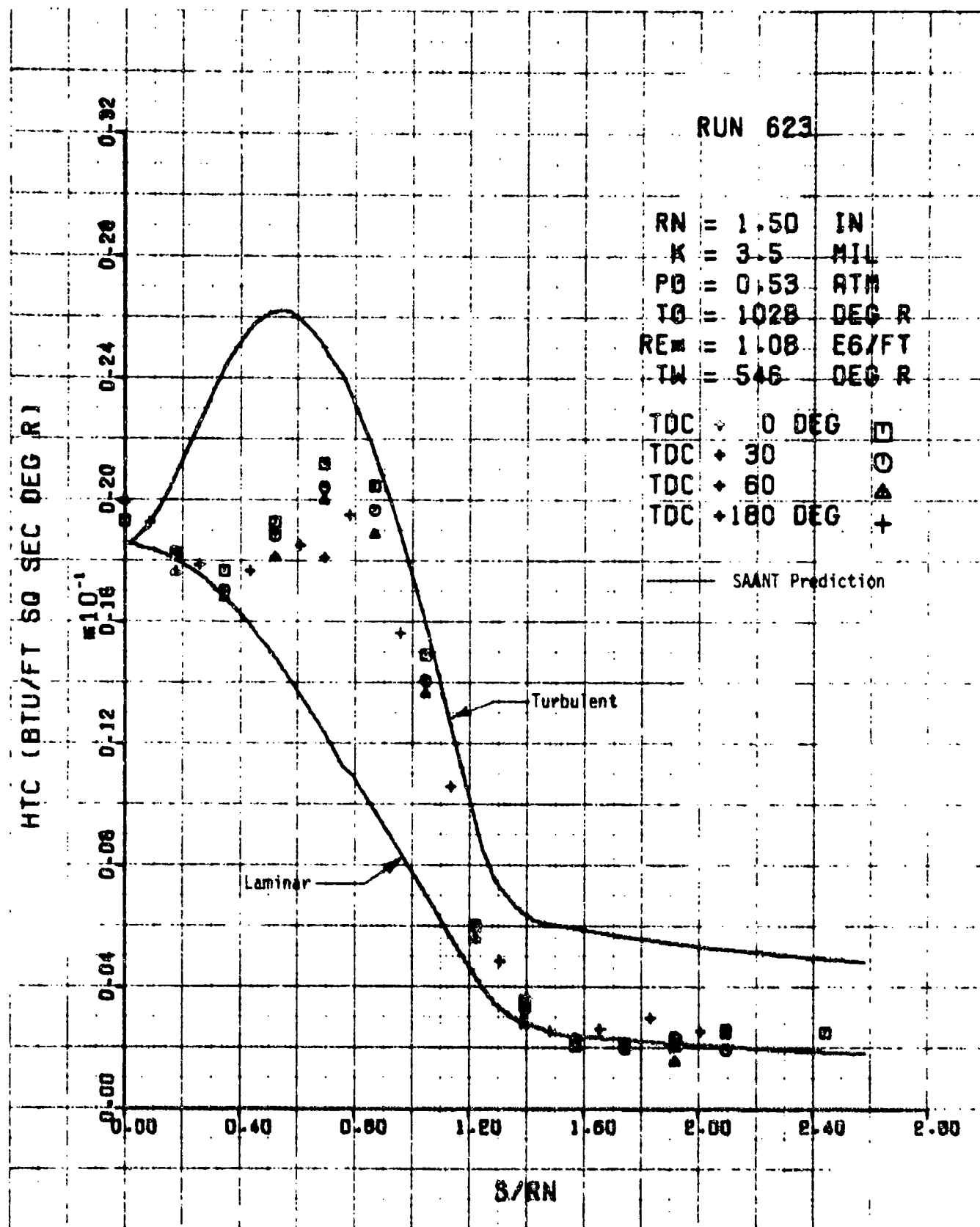


Figure 31. Continued

f. Run No. 623 ( $Re_m = 2.77 \times 10^4$ /ft)

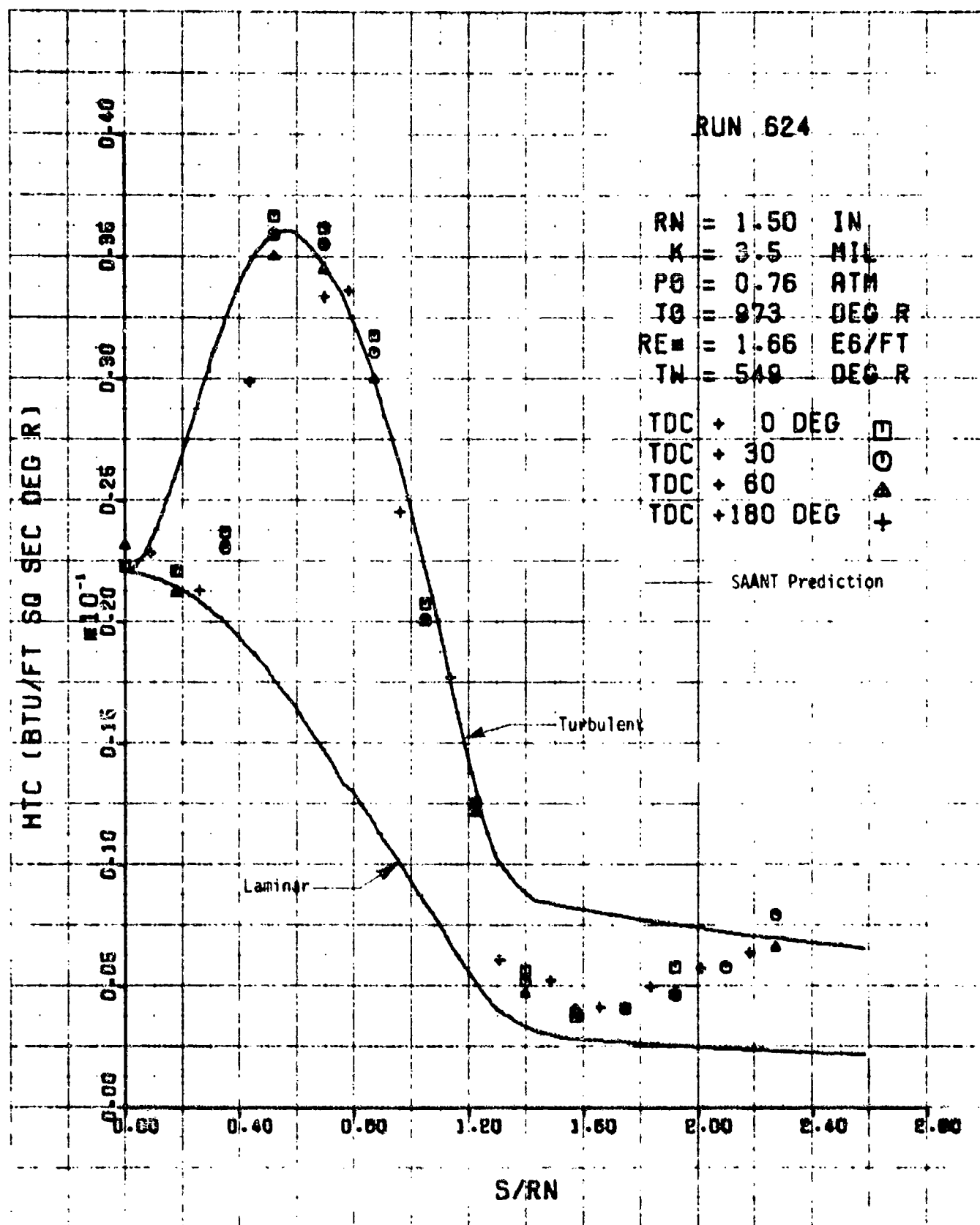


Figure 31. Continued

a. Run No. 624 ( $Re_s = 4.31 \times 10^6/\text{ft}$ )

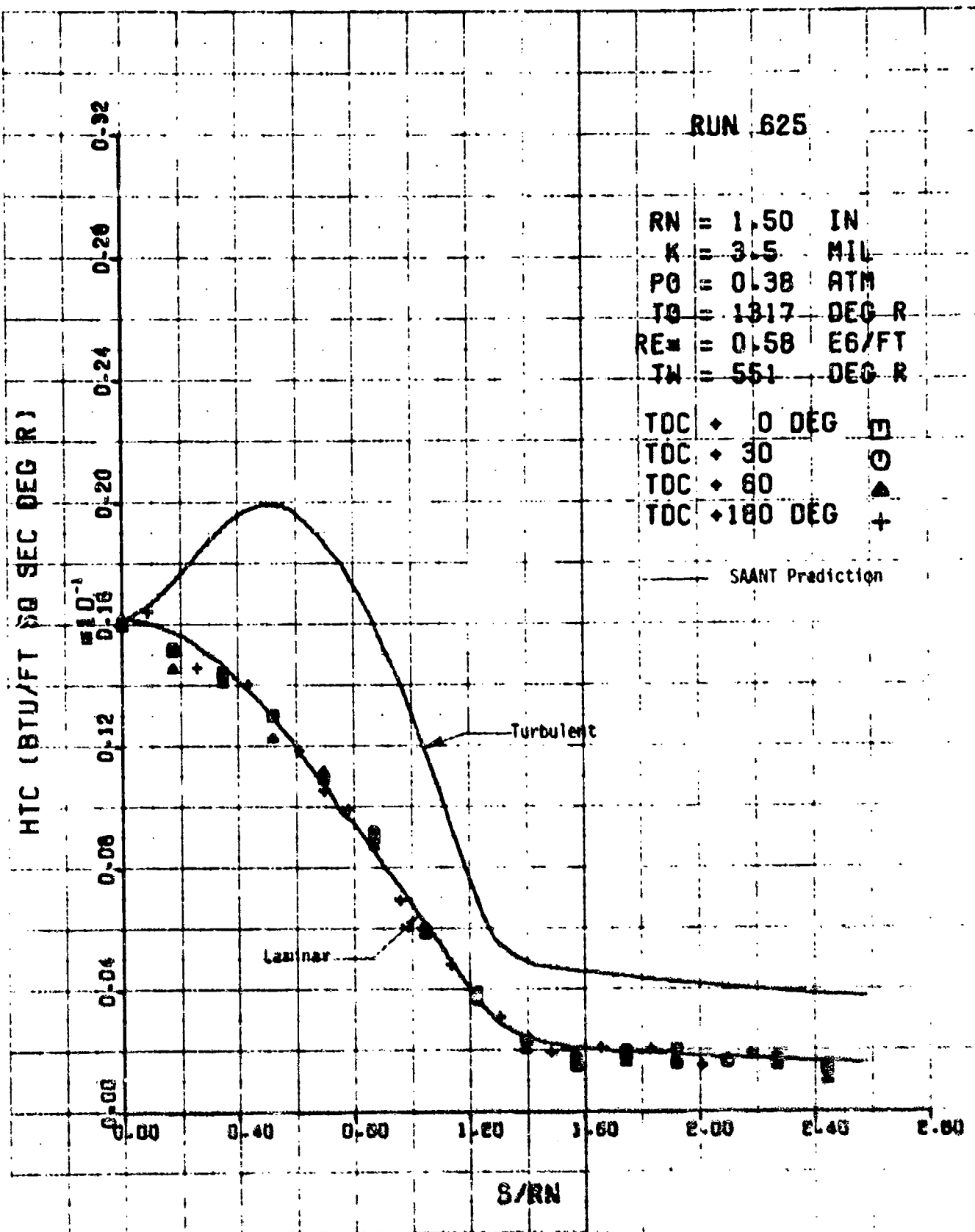


Figure 31. Continued

h. Run No. 625 ( $Re_s = 1.38 \times 10^6 / ft$ )

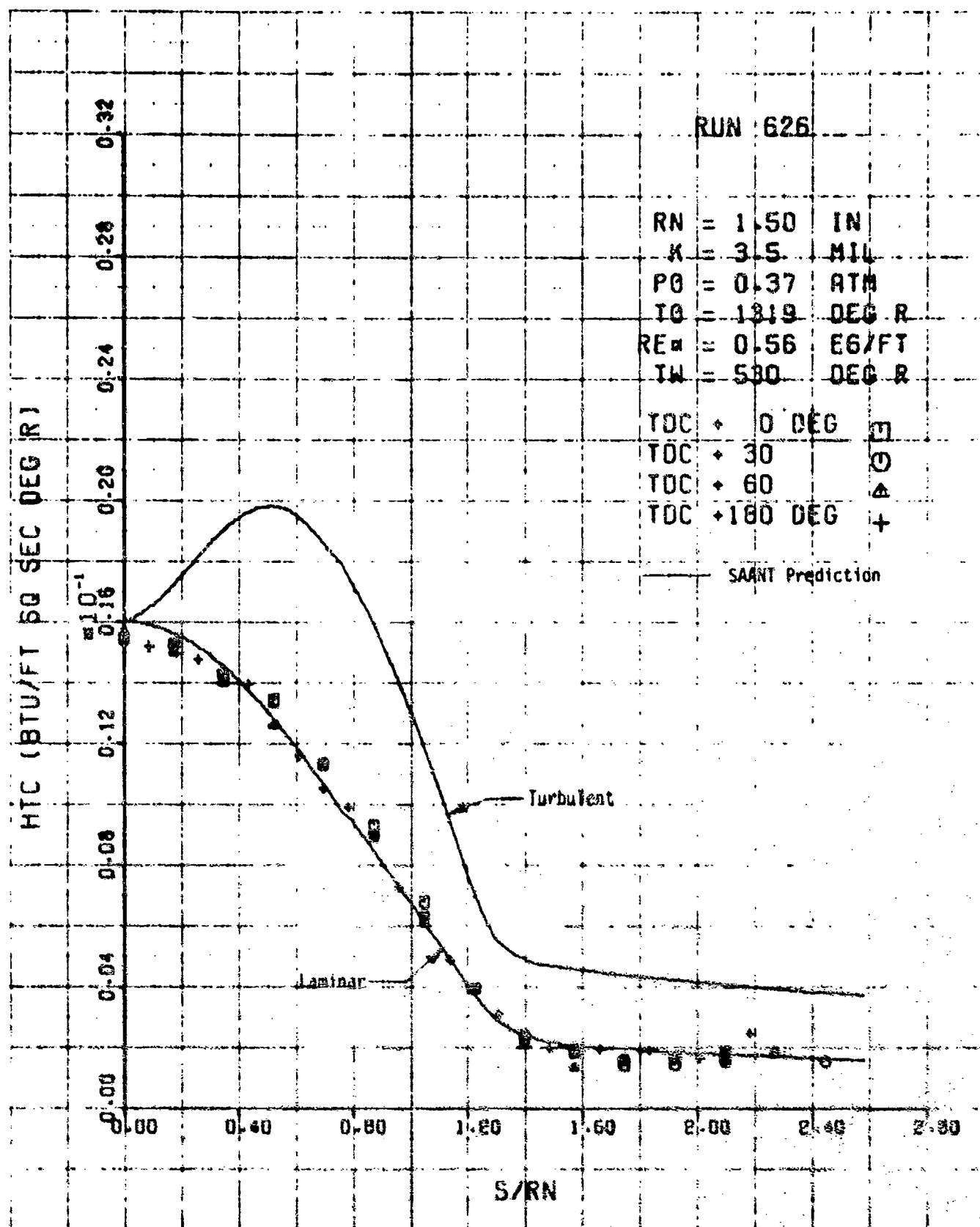


Figure 31. Continued

(, Run No. 626 ( $Re_w = 1.35 \times 10^5$ /ft)

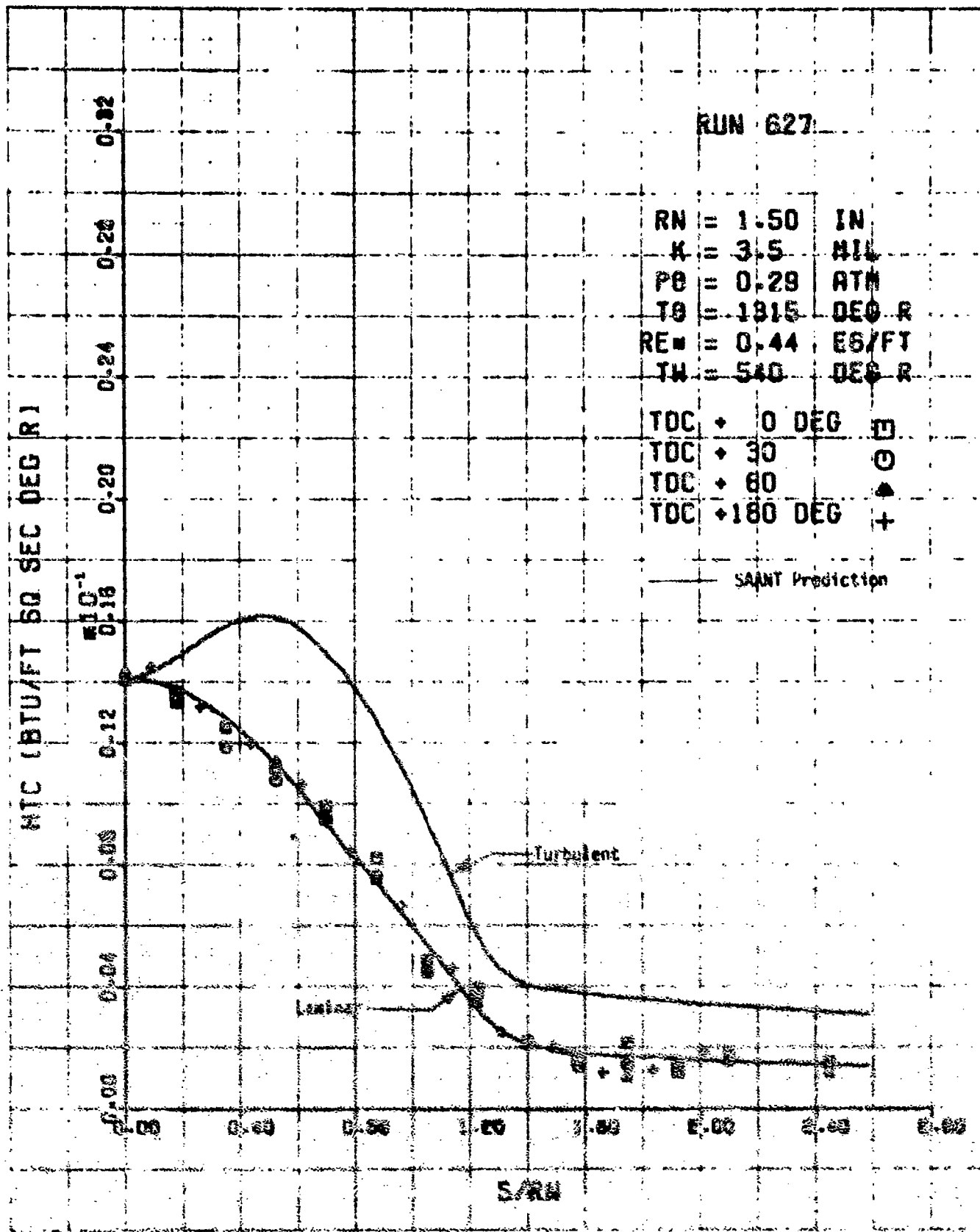


Figure 31. Concluded

1. Run No. 627 ( $Re = 1.07 \times 10^4$  ft)

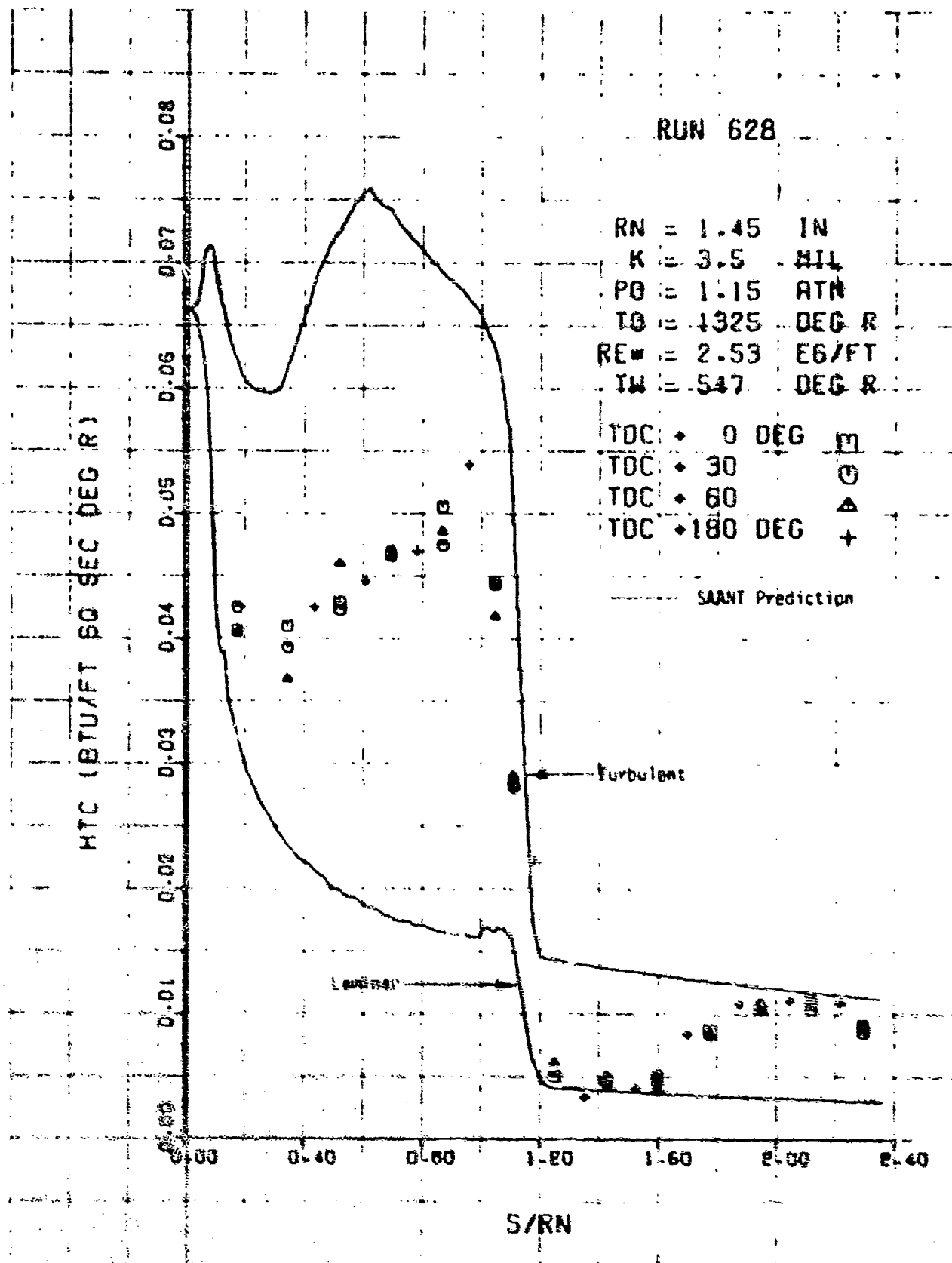


Figure 10 Convective Heat Transfer Coefficient Distribution,  
Model 22, Biconic,  $R_s = 1.5$  inches

Run No. 628  $Pe_s = 3.0 \times 10^4$  sec

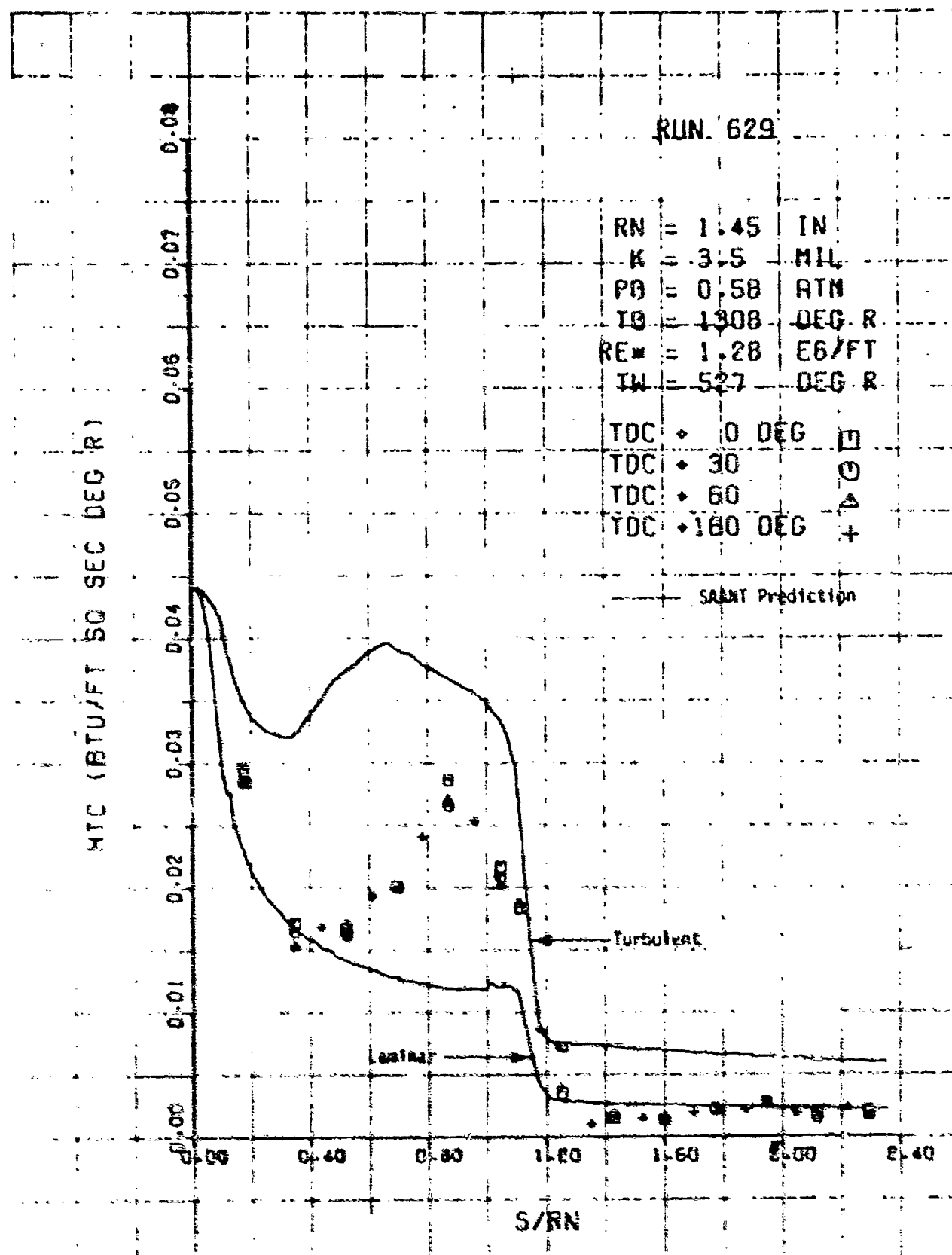


Figure 12 Continued

b. Run No. 629 ( $Re_c = 2.12 \times 10^5/ft$ )



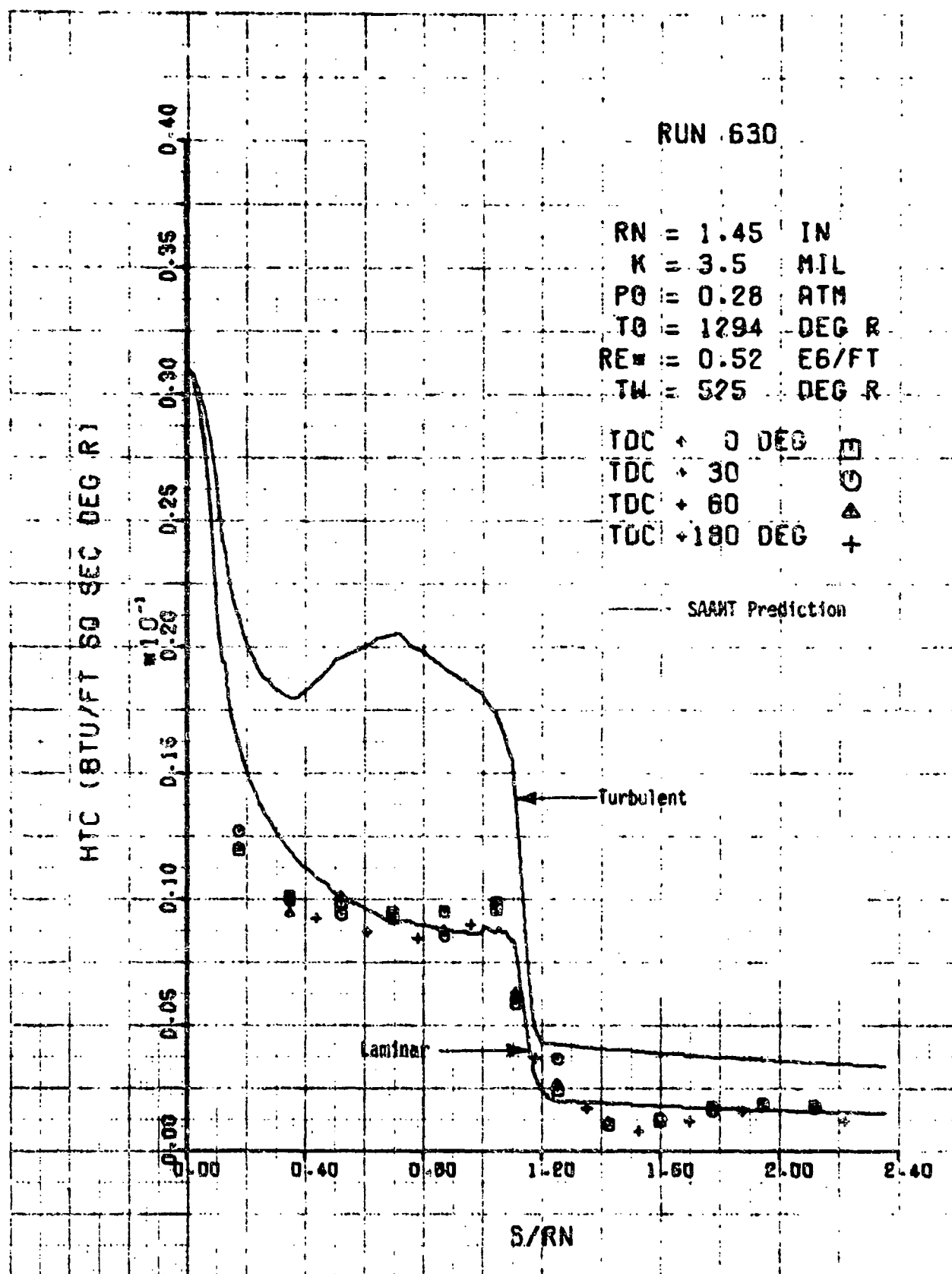


Figure 32. Continued

c. Run No. 630 ( $Re_{\infty} = 1.06 \times 10^6/\text{ft}$ )

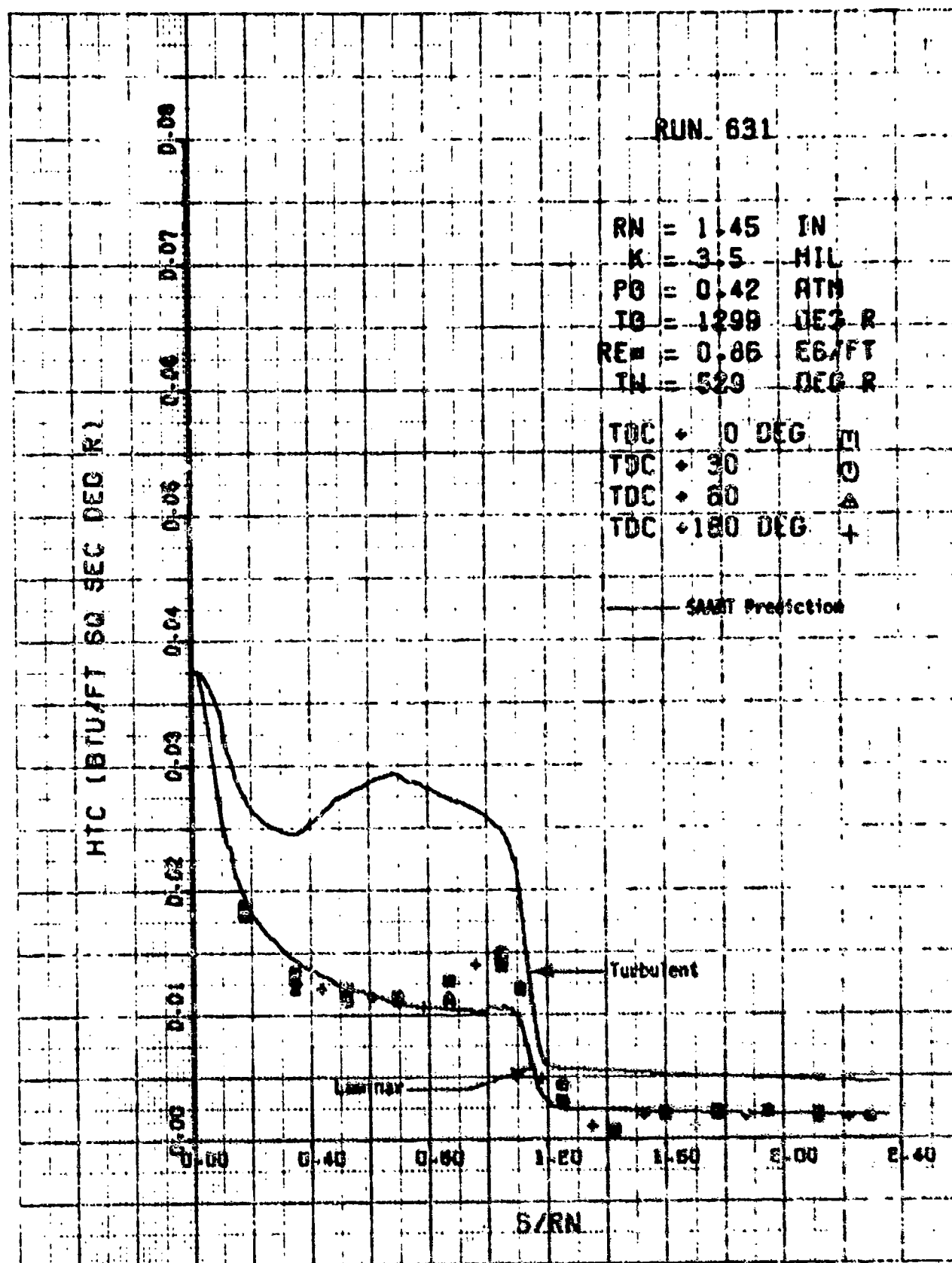


Figure 32. Continued

d. Run No. 631 ( $Re_m = 1.55 \times 10^5/\text{ft}$ )

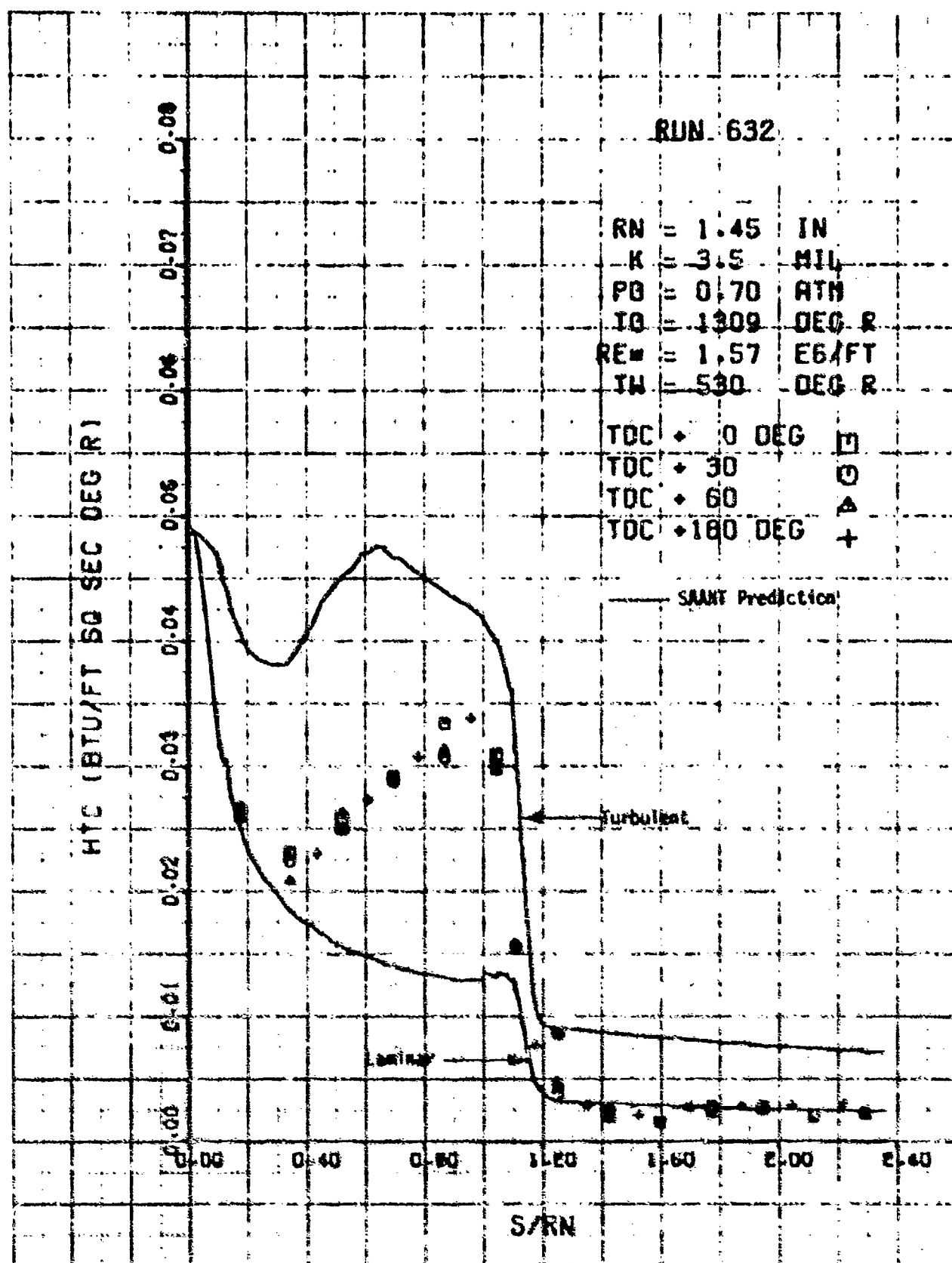


Figure 32. Continued

e. Run No. 632 ( $Re_{\infty} = 2.54 \times 10^6/\text{ft}$ )

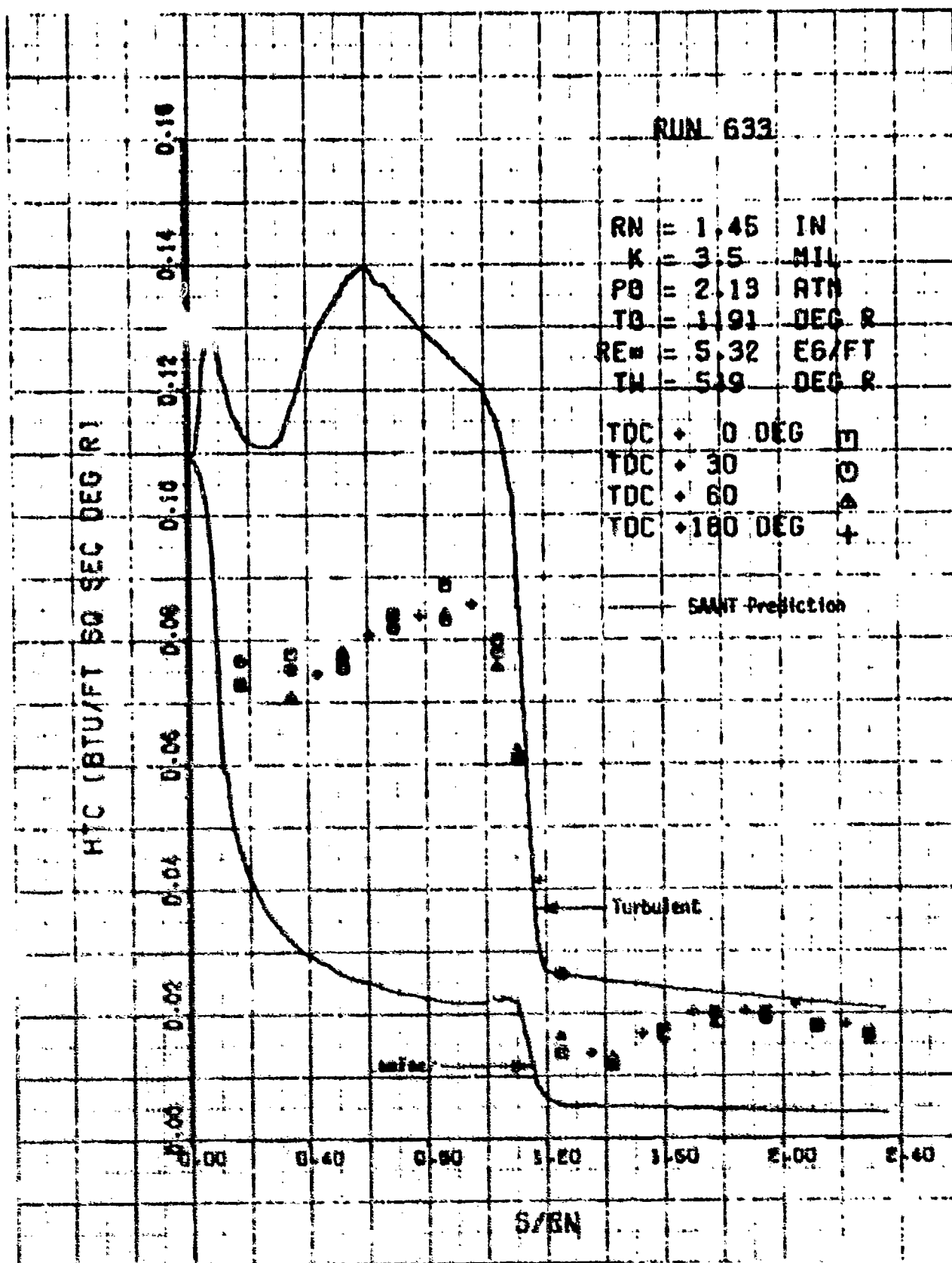


Figure 32. Concluded

f. Run No. 633 ( $Re_{\infty} = 8.79 \times 10^4/\text{ft}$ )

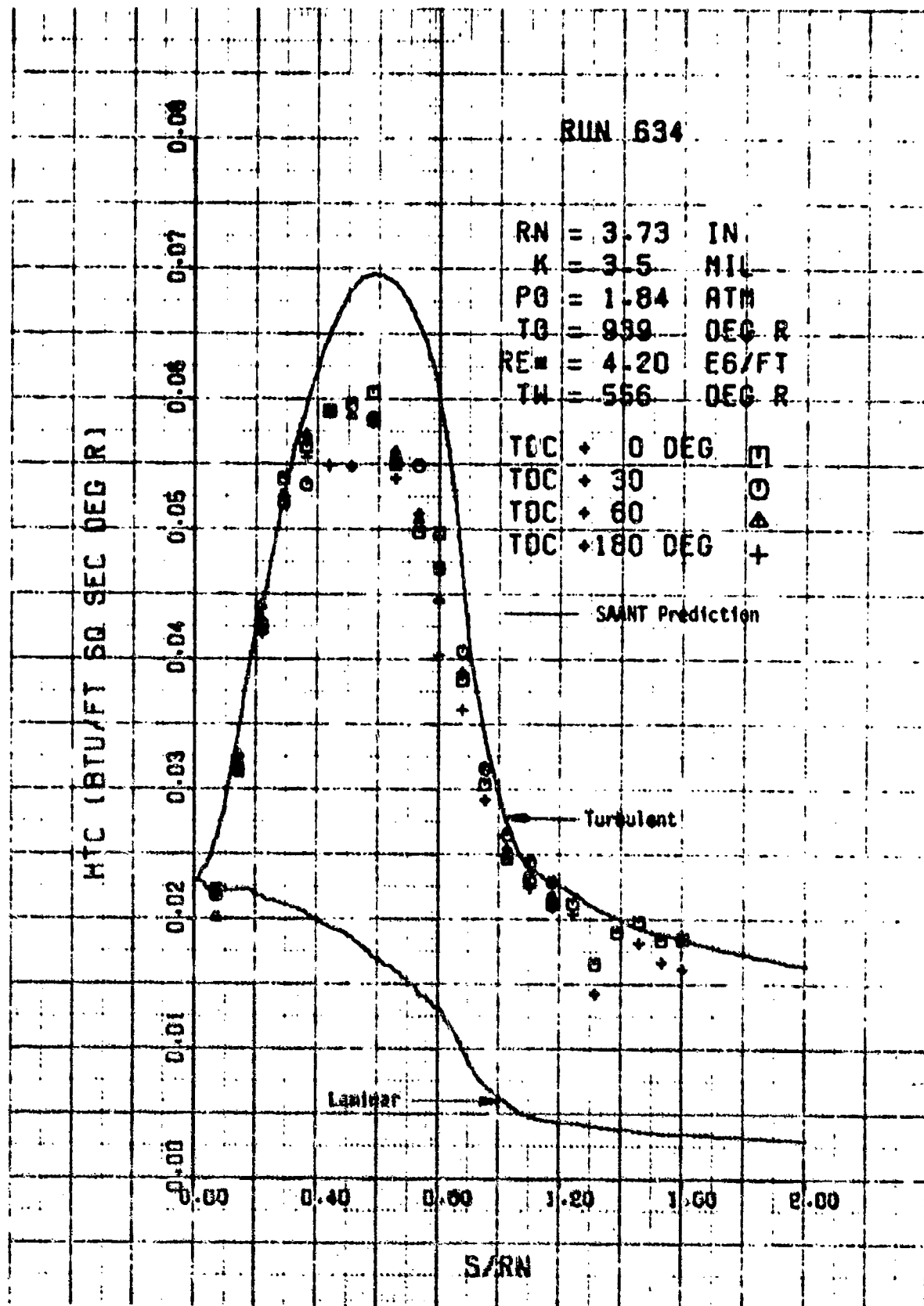


Figure 33. Convective Heat Transfer Coefficient Distribution, Model 19, Laminar Shape,  $R_s = 3.5$  Inches

a. Run No. 634 ( $Re_s = 10.90 \times 10^6/\text{ft}$ )

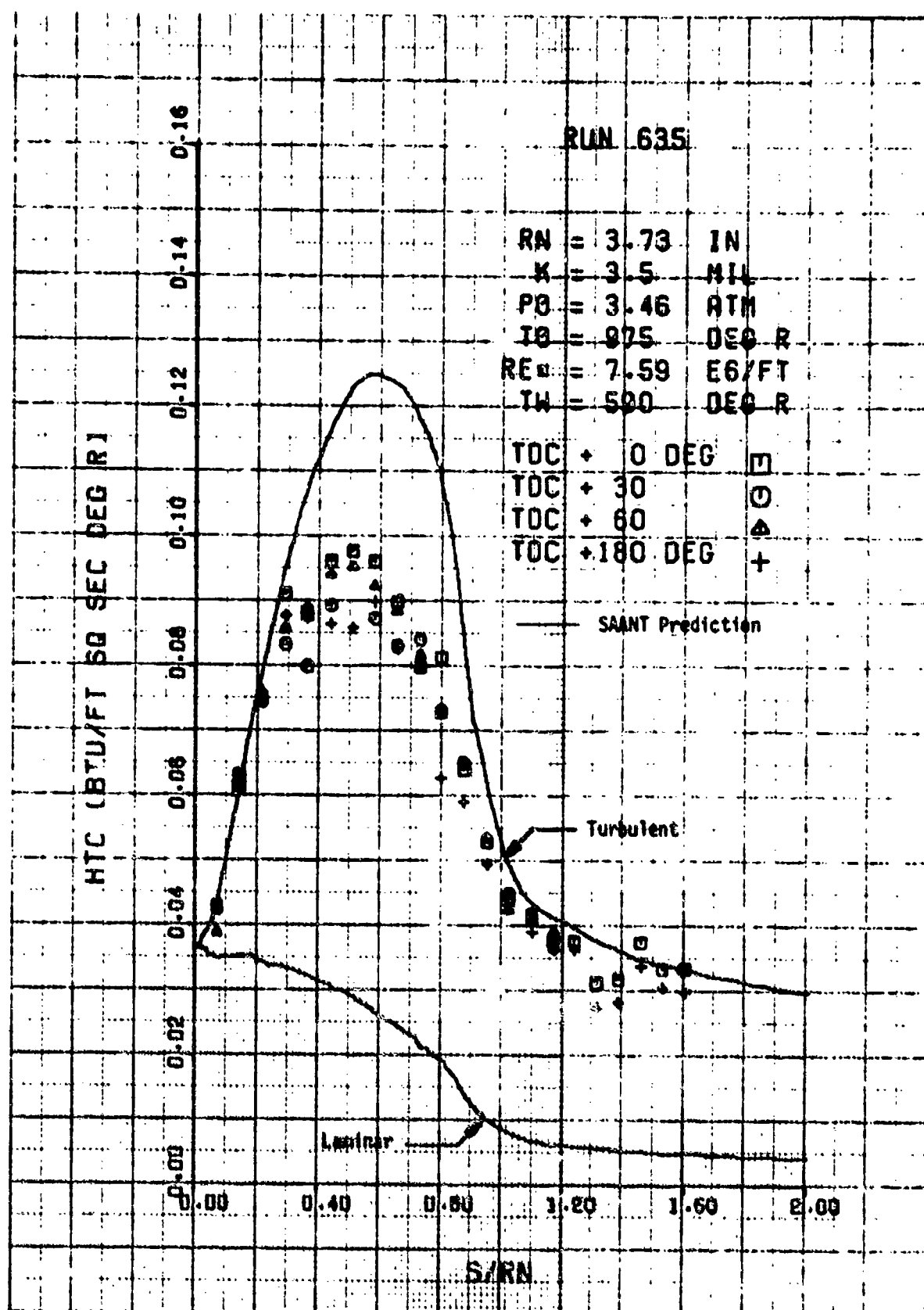


Figure 33. Continued

b. Run No. 635 ( $Re_{\infty} = 19.41 \times 10^6/\text{ft}$ )

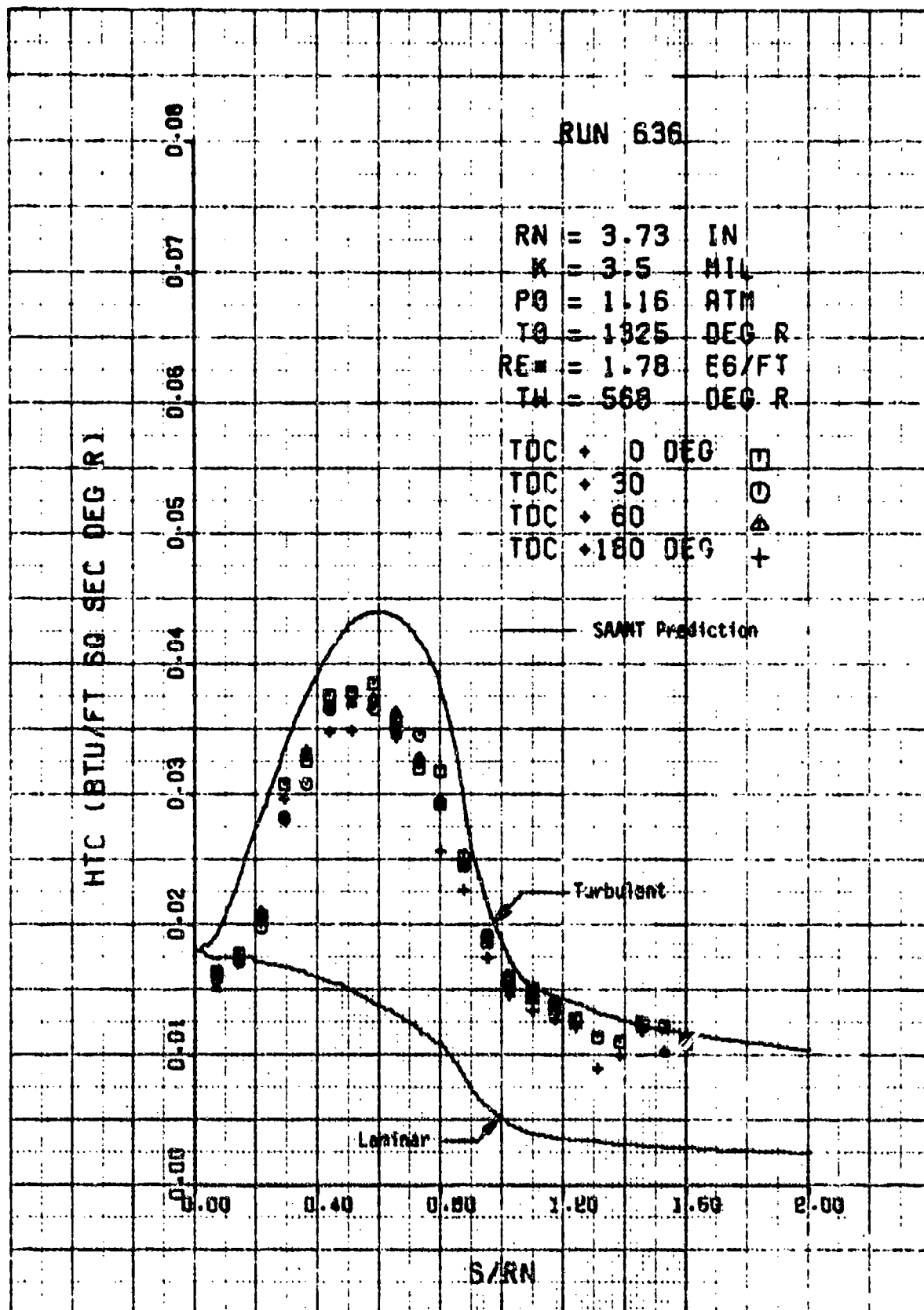


Figure 33. Continued

c. Run No. 636 ( $Re_{\infty} = 4.09 \times 10^6/\text{ft}$ )

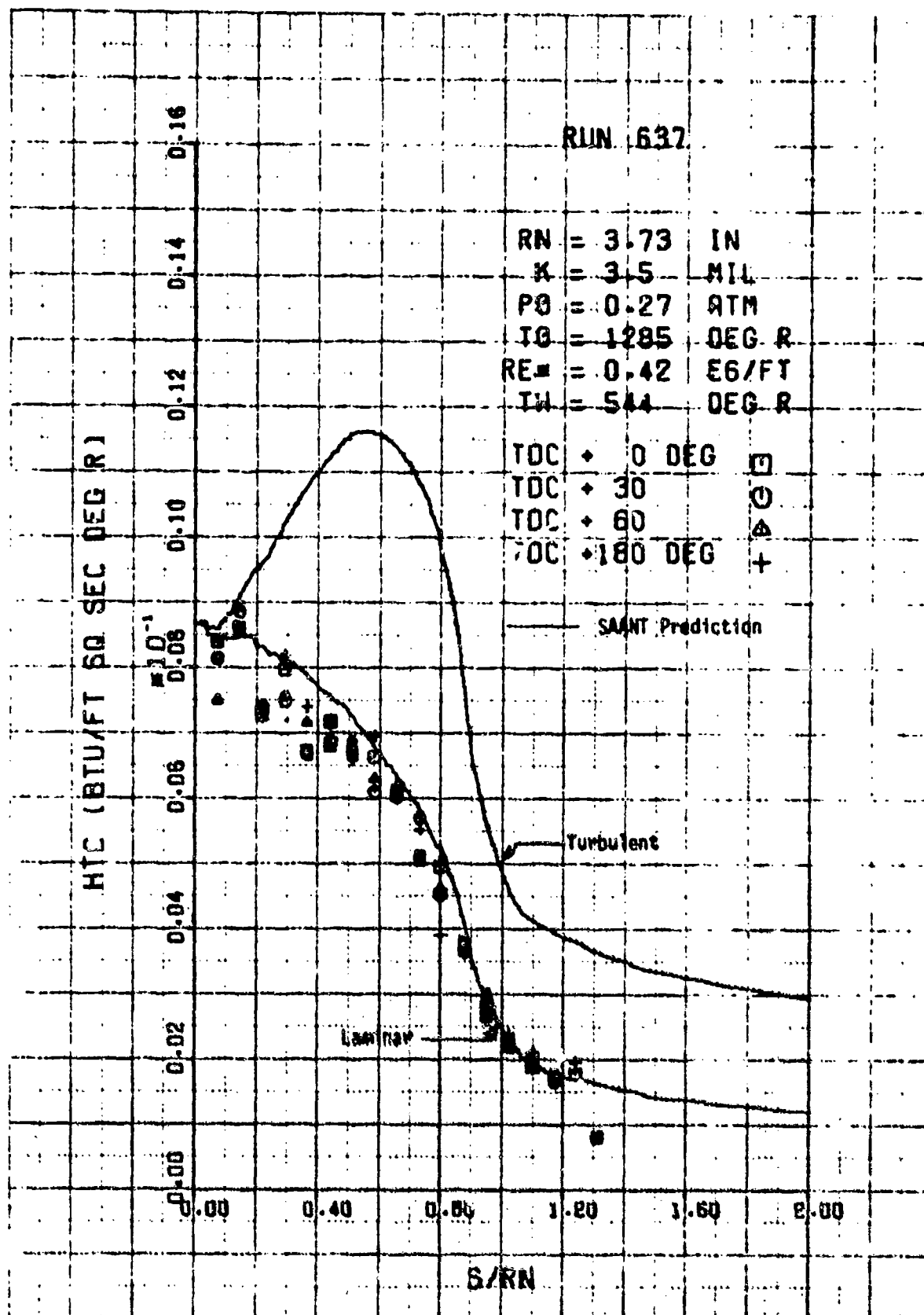


Figure 33. Continued

d. Run No. 637 ( $Re_w = .98 \times 10^6/\text{ft}$ )



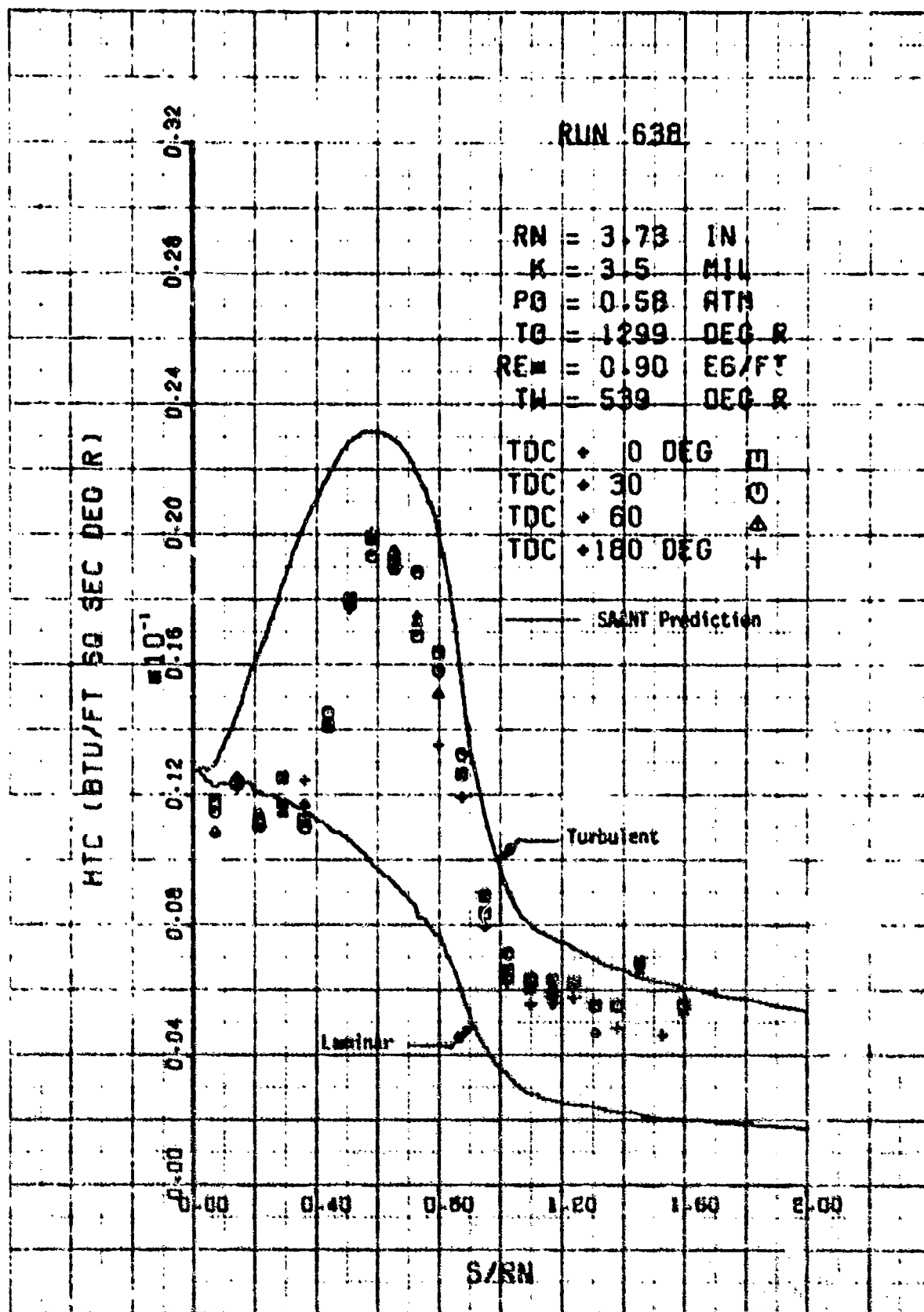


Figure 33. Continued

e. Run No. 638 ( $Re_{\infty} = 2.08 \times 10^6/\text{ft}$ )

HTC (BTU/FT SQ SEC DEG R)

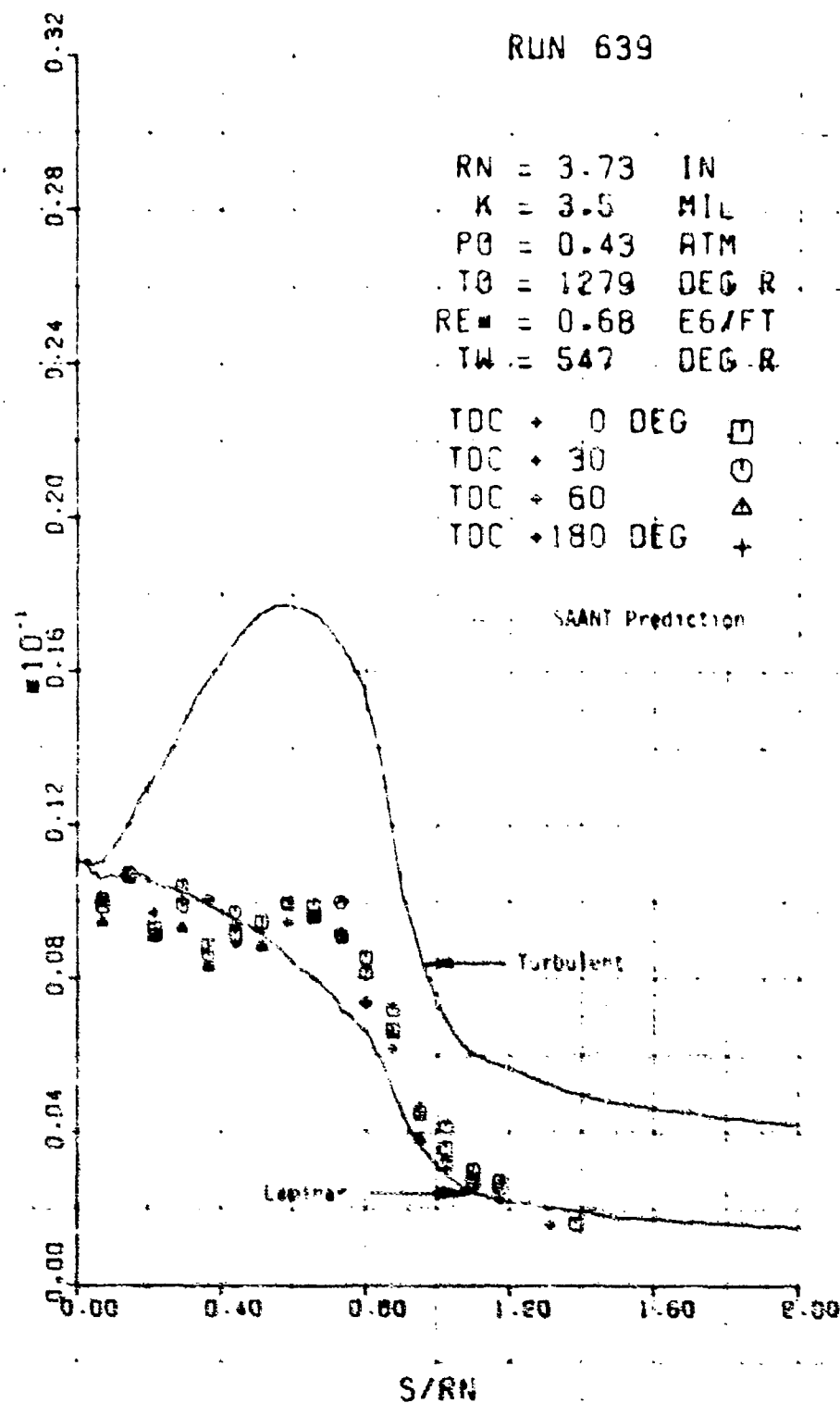


Figure 10. Heat Transfer

HTC vs. S/RN for Run 639, 1279 DEG R, 0.68 E6/FT

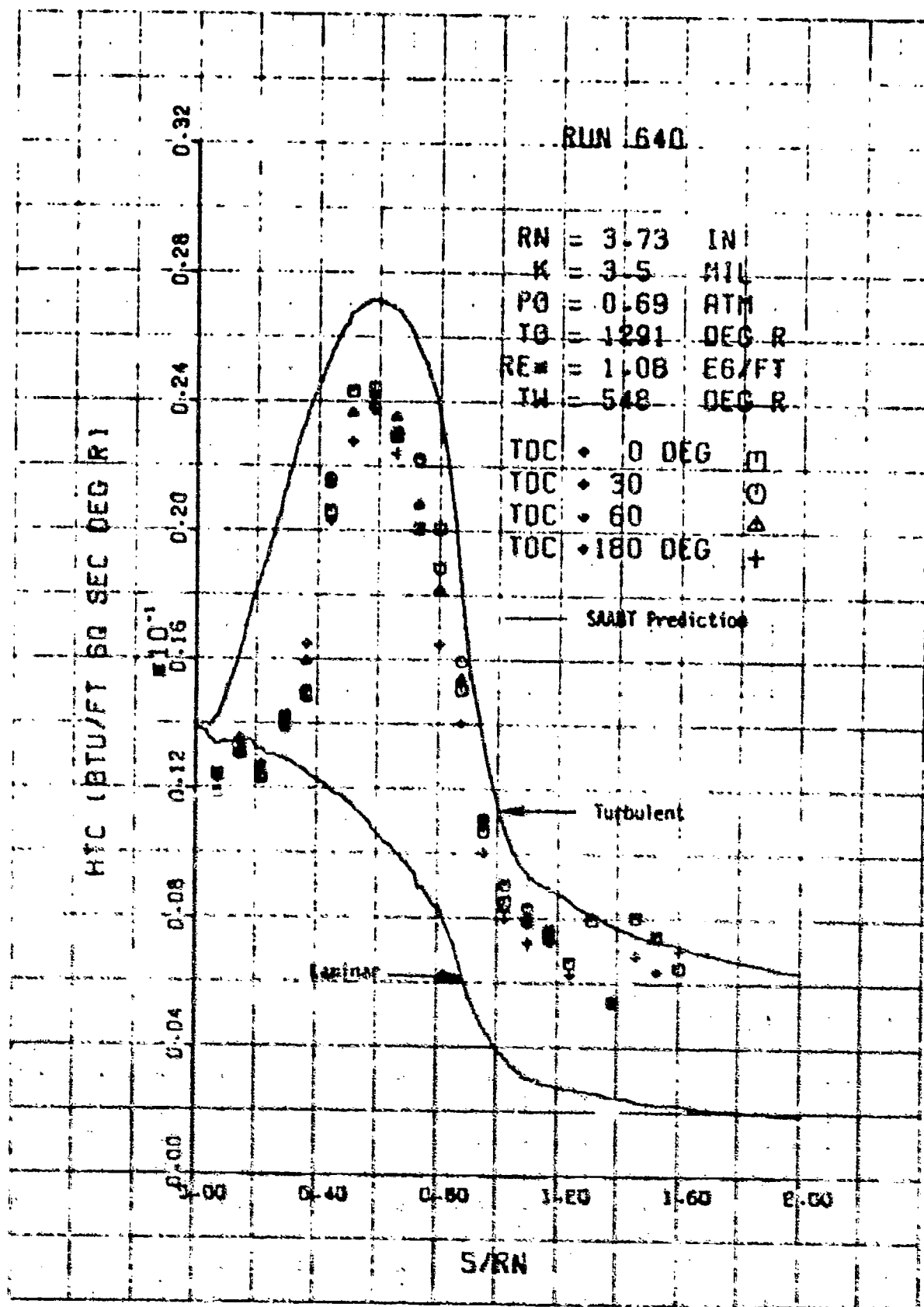


Figure 33. Concluded

g. Run No. 640 ( $Re_m = 2.37 \times 10^5/ft$ )

## SECTION 7

### SUMMARY OF RESULTS AND CONCLUSIONS

The PANT Series J experiments provide the basis for evaluating the adequacy of existing rough wall boundary layer transition correlations. Detailed analysis of this data is not included here; however some comments relative to the test series are warranted. These comments are limited to calorimeter model performance and data trends.

#### Calorimeter Model Performance

In general the quality of the Series J data is quite good. For all models there is little or no ambiguity in interpreting the transition location for a particular test point. The data scatter at a streamwise location is within acceptable experimental accuracy and indicates probably only slight differences in thermocouple location, thermocouple attachment and/or transition location. Additionally, this lack of data scatter also illustrates that the surface roughness was uniformly distributed over the calorimeter surface.

The individual heat transfer coefficients are calculated using a simplified energy equation which accounts for variations in calorimeter thermal properties, wall thickness as well as streamwise heat conduction along the calorimeter shell. The accuracy of this method is verified by both the quality and the consistency of the data.

#### Data Trends

One of the more interesting effects illustrated by the Series J data is the dependency of boundary layer transition on body size. Figure 14 summarizes the data obtained on the sphere cone models in terms of sonic point unit Reynolds number and nose radius. The data presented here are for a nearly constant wall cooling ratio,  $T_w/T_\infty$ . Although somewhat subjective, this figure illustrates as the nose radius decreases the boundary layer tends to be more stable. Larger  $Re^*$  is required to promote boundary layer transition on the smaller nose radius models.

As indicated in Section 4, Runs 625 and 626 were tested at near constant supply conditions but with a 30 percent increase in the aerodynamic noise level for Run 626. Figure 34 indicates that the boundary layer for both runs remained laminar. This result implies that the boundary layer transition is probably roughness dominate. The evidence is not conclusive however, since the data base is neither large enough nor varied enough to fully assess the effects of tunnel noise.

Another interesting point highlighted by the Series J data is boundary layer relaminization which existed to some degree on all models except the laminar ablated shape model. A good example of this phenomenon is illustrated in Figure 32(f) for the biconic model (Run 633). Even at the relatively high Reynolds number ( $Re^* = 5.32 \times 10^6/\text{ft}$ ) there is partial relaminarization in the corner region.

One should also note, that the SAANT solutions adequately predict the fully turbulent heat transfer coefficient distributions for all models except the biconic model. The agreement between predicted and measured heat transfer coefficients for the sphere cone models substantiates the correlation of heating augmentation due to roughness recommended in Reference 5. A brief study was performed to assess the discrepancy between the measured and predicted heat transfer coefficients for the biconic model. This study showed that the current shock correlation in SAANT was inadequate for the biconic model, and caused overprediction of the boundary layer edge entropy.

In summary, the rough wall calorimeter data was of excellent quality and provides the basis for a better understanding of rough wall boundary layer transition.

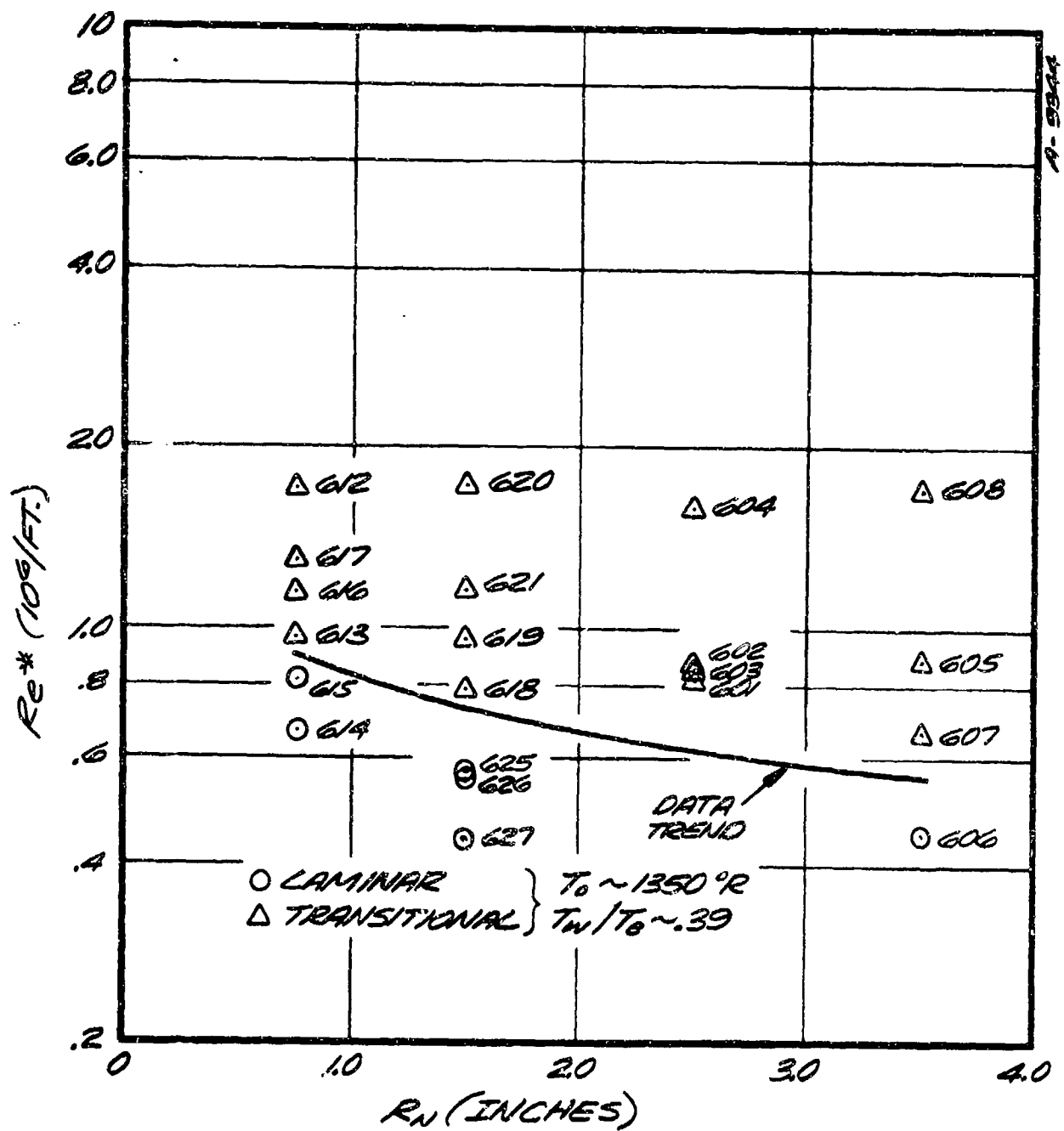


Figure 34. Summary of Transition Data on Sphere Cone Models

## REFERENCES

1. Abbett, M. J. , et. al., "Unsteady Flow on Ablated Nosetip Shapes", Aero-therm Report 73-87, Aerotherm Division/Acurex Corporation, December 1973.
2. Jackson, M. D. and Baker, D. L., "Passive Nosetip Technology (PANT) Program, Interim Report, VOL. III - Surface Roughness Effects, PANT I - Experimental Data," SAMSO-TR-74-86, January 1974.
3. Anderson, A. D., "Passive Noetip Technology (PANT) Program. Interim Report, Vol. III - Surface Koughness Effects, Part III - Boundary Layer Transition, SAMSO-TR-74-86, January 1974. (Confidential).
4. Jackson, M. D. and Nelson, E. V., "Roughness Induced Transition, PANT Environmental Test Plan, Series J," Aerotherm Report 74-94, Aerotherm Division/Acurex Corporation, January 1974.
5. Powars, C. A., "Passive Nosetip Technology (PANT) Program, Interim Report, Vol. III - Surface Roughness Effects, Part II - Roughness Augmented Heating Data Correlation and Analysis," SAMSO-TR-74-86, January 1974. (Confidential)
6. Personal Communication, Denman, G. L., Air Force Materials Laboratory, MXS, Wright Patterson Air Force Base, Ohio.
7. "A Recommended Revised Wind Tunnel Test Plan for the PANT Program," TM-71-12, Aerotherm Division/Acurex Corporation, July 1971.
8. Baltakis, F. P., "PANT Series H and J Heat Transfer Wind Tunnel Test Data, Wind-Tunnel Report No. 83, Naval Ordnance Laboratory, May 1974.
9. Kovaszny, L. S. G., "Turbulence in Supersonic Flow," Journal of the Aeronautical Sciences, Vol. 20, pp. 657, October 1953.
10. Pate, S. R. and Schueler, C. J., "Radiated Aerodynamic Noise Effects on Boundary-Layer Transition in Supersonic and Hypersonic Wind Tunnels, AIAA Journal, Vol. 7, pp. 2241, March 1969.
11. Stainback, P. C., "Hypersonic Boundary Layer transition in the Presence of Wind-Tunnel Noise," AIAA Journal, Vol. 9, pp.2475, December 1971.
12. "Thermal Conductivity and Heat Capacity of an Electrolytic Nickel," Southern Research Institute Final Report to Aerotherm/Acurex, P.O. 17299, December 1971.
13. American Society for Metals, Metals Handbook, Vol. I, 8th Editing, 1964.
14. Wool, M. R., Overly, P. T., and Derbidge, T. C., "Passive Nosetip Technology (PANT) Program, Interim Report, Vol. VII - Computer User's Manual, Steady-State Analysis of Ablating Nosetips (SAANT) Program," SAMSO-TR-74-86, January 1974.